



Spectroscopic study of manganites with magnetoelectric coupling

Dissertation zur Erlangung des
naturwissenschaftlichen Doktorgrades
der Julius-Maximilians-Universität Würzburg

vorgelegt von
Alexey Shuvaev
aus Wolgograd

Würzburg 2012

Eingereicht am: 20. Dezember 2012

bei der Fakultät für Physik und Astronomie

Gutachter der Dissertation:

1. Gutachter: Prof. Dr. A. Pimenov
2. Gutachter: Prof. Dr. J. Geurts
3. Gutachter: Prof. Dr. T. Kimura

Vorsitzender: Prof. Dr. K. Mannheim

Prüfer im Promotionskolloquium:

1. Prüfer: Prof. Dr. A. Pimenov
2. Prüfer: Prof. Dr. J. Geurts
3. Prüfer: Prof. Dr. F. Assaad

Tag des Promotionskolloquiums: 4. Juli 2013

Doktorurkunde ausgehändigt am: 24. Juli 2013

“But, after all, what use is it?”

“Why, sir, there is every probability that you will soon be able to tax it!”

Michael Faraday to William Gladstone, the Chancellor of the Exchequer, when he asked about the practical worth of electricity [1].

Contents

Zusammenfassung	ix
Abstract	xi
1 Introduction	1
1.1 Revival of the magnetoelectric effect	2
1.2 Rare earth manganites RMnO_3	9
1.2.1 Crystal structure	10
1.2.2 Jahn-Teller effect and orbital order	13
1.2.3 Magnetic interactions and phase diagram	15
2 Magnons	21
2.1 Underlying equations	22
2.2 Ferromagnets	23
2.2.1 Ferromagnet with easy axis anisotropy in magnetic field	23
2.2.2 The treatment of the exciting field and dissipation	25
2.2.3 Ferromagnet with next-nearest-neighbour interaction	27
2.3 Ferrimagnets	28
2.4 Simple collinear antiferromagnet	32
2.5 Cycloidal incommensurate antiferromagnet	38
2.5.1 The unit cell and Brillouin zone	38
2.5.2 Cycloidal antiferromagnet with easy plane anisotropy	40
2.5.3 Inelastic neutron scattering spectra	44
2.5.4 Antiferromagnetic resonances in optical spectroscopy	46
2.5.5 Inverse Dzyaloshinskii-Moriya model of electromagnons	50
2.5.6 Heisenberg exchange model of electromagnons	53
3 Experimental techniques	59
3.1 Mach-Zehnder interferometer	59
3.2 Analysis of the spectra	64
3.3 Sample characterization	67
4 GdMnO_3: introducing an electromagnon	69
4.1 Zero field THz and FIR spectra	69
4.2 Coupling of phonons and electromagnons	73
4.3 Summary	75

5	Eu_{1-x}Y_xMnO₃: manganese <i>vs.</i> rare earth	77
5.1	Multiferroic phases of Eu _{1-x} Y _x MnO ₃	77
5.2	Canted antiferromagnetic phase: $x = 0.1$	79
5.3	Cycloidal antiferromagnetic phase: $x = 0.5$	81
5.4	Summary	83
6	DyMnO₃: electromagnon as a soft mode	85
6.1	THz excitations in zero magnetic field	85
6.2	Electromagnons in external magnetic fields	89
6.2.1	Magnetic field along the a axis	90
6.2.2	Magnetic field along the b axis	95
6.3	Summary	98
7	TbMnO₃: electromagnon internals	101
7.1	Temperature dependence of excitations in zero magnetic field	101
7.2	Electric and magnetic excitations in external magnetic field	108
7.3	Summary	117
8	Conclusions and outlook	119
	Bibliography	123
	Acknowledgments	129

Zusammenfassung

Die vorliegende Dissertation befasst sich mit den spektroskopischen Untersuchungen von Manganaten der Seltenen Erden im Bereich der Submillimeterwellen. Spektroskopisches Merkmal der starken elektromagnetischen Kopplung ist die Existenz der Elektromagnonen – Spinwellen, die durch das elektrische Feld des Lichtes angeregt werden.

Die Lösung der Landau-Lifshitz Gleichungen für die zyklonale magnetische Ordnung verbindet die inelastische Neutronstreuung mit den optischen Experimenten. Eine halbquantitative Übereinstimmung wurde zwischen der Theorie und diesen zwei experimentellen Techniken erreicht. Zwei Mechanismen der magnetoelektrischen Kopplung, die inverse Dzyaloshinskii-Moriya (IDM) Wechselwirkung und das auf den symmetrischen Heisenberg Austausch basierte Modell, werden in einer perturbativen Art eingeführt.

Die Ferninfrarotmessungen an GdMnO_3 zeigen die Existenz eines zweiten Elektromagnons bei 75 cm^{-1} . Diese Beobachtung deutet auf die Existenz von zumindest kurzzeitigen ferroelektrischen Ordnungsparameter in GdMnO_3 .

Die Untersuchung der Elektromagnonen in $\text{Eu}_{1-x}\text{Y}_x\text{MnO}_3$ Mischsystemen hat die Rolle des Magnetismus der Seltenen Erden geklärt. Nachdem Y^{3+} Ionen diamagnetisch sind und Eu^{3+} Ionen nur Van Vleck Paramagnetismus aufweisen, ist das Mn Untersystem vorrangig für die magnetoelektrischen Eigenschaften der Selten-Erd-Manganaten verantwortlich.

Die Untersuchung von DyMnO_3 in äußeren Magnetfeldern hat gezeigt, dass, je nach magnetischer Ordnung von Dy, die Elektromagnonen und die statische elektrische Polarisation entweder erhöht oder unterdrückt werden können. Daher spielt die magnetische Ordnung der Seltenen Erde eine wichtige Rolle.

Nach der Rotation der Spinzykloide in äußeren Magnetfeldern ändern die Elektromagnonen in DyMnO_3 und TbMnO_3 ihre Auswahlregeln nicht. Für diese Beobachtung fehlt jedoch noch eine übereinstimmende theoretische Erklärung. Die genauen Messungen von unterschiedlich orientierten TbMnO_3 Proben ermöglichten einen schwachen elektrischen Beitrag bei 21 cm^{-1} zu detektieren. Das ist die erste direkte Beobachtung einer dynamischen Anregung der IDM Wechselwirkung.

Zusammenfassend, kann die IDM Wechselwirkung die statische elektrische Polarisation und die schwache elektrische Anregung in der Hochfeldphase von TbMnO_3 gut beschreiben. Das HE Modell wird erfolgreich bei der Erklärung des Hochfrequenzelektromagnons, dessen Auswahlregeln und des Spektralgewichts angewandt. Beide Modelle sind jedoch noch nicht in der Lage die Energie und das Spektralgewicht des Niederfrequenzelektromagnons zu beschreiben. Weitere theoretische Anstrengungen sind nötig um die noch verbleibenden offenen Fragen zu klären.

Abstract

The present thesis is devoted to the spectroscopic study of rare earth manganites RMnO_3 ($\text{R} = \text{Gd}, \text{Dy}, \text{Tb}, \text{Eu}_{1-x}\text{Y}_x$) in the submillimeter frequency range. A dynamic manifestation of a strong magnetoelectric coupling in these systems is the existence of electromagnons – spin waves excited by the electric component of the electromagnetic wave.

The exact analytical solution of the Landau-Lifshitz equations obtained for cycloidal antiferromagnets builds the bridge between the inelastic neutron scattering and the optical experiments. A semi-quantitative agreement is achieved between the theory and the results by these two experimental techniques. Two suggested mechanisms of the magnetoelectric coupling, the inverse Dzyaloshinskii-Moriya (IDM) interaction and the symmetric Heisenberg exchange (HE) striction, are introduced in a perturbative manner. The qualitative conclusions regarding both static and dynamic electric properties are also in agreement with the experiment.

GdMnO_3 is the system in which the electromagnons were first detected at low frequencies. Far infrared measurements in GdMnO_3 presented here have confirmed the existence of a second high frequency electromagnon at 75 cm^{-1} . The detection of an additional mode suggests the existence of at least short range ferroelectric order. Such order has not been observed in static experiments so far.

The electromagnons in $\text{Eu}_{1-x}\text{Y}_x\text{MnO}_3$ helped to clarify the role of the rare earth magnetism. As the Y^{3+} ions are diamagnetic and Eu^{3+} ions possess Van Vleck paramagnetism only, it is the Mn subsystem that is primarily responsible for the magnetoelectric properties of rare earth manganites.

The electromagnons in DyMnO_3 and TbMnO_3 do not change their excitation conditions upon the flop of the spin cycloid in external magnetic fields. This fact still lacks consistent theoretical explanation. Detailed measurements on TbMnO_3 of different orientations have allowed to prove the existence of the IDM electromagnon. The study of DyMnO_3 in external magnetic fields has shown that, depending on the Dy ordering, the electromagnons and static electric polarization can be either enhanced or suppressed. Thus, the magnetic order of rare earth moments still plays an important role.

As a general result of the present work, the IDM interaction is capable to describe the static electric polarization and the weak electro-active excitation in the high-field phase of TbMnO_3 . The HE model is successful in explaining the high frequency electromagnon, including its excitation conditions and the spectral weight. However, both models are still unable to describe the energy and the spectral weight of the low frequency electromagnon. Further theoretical and experimental efforts are required in this direction.

1 Introduction

Scientific discoveries have radically changed our everyday life over the last century. The modern way of life would not be possible without electricity, for example. The night lighting in almost all of its current forms, from room and table lamps to the car headlights and pocket flashlights, uses electricity as a main or intermediate energy source. Electric motors have made a lot of household tools and industry machines possible. Nearly all air conditioning fans are run by some type of electric motor. The role of electricity in the modern medicine is also tremendous. The majority of diagnostic and treatment equipment is of electrical type, besides the most simple ones like thermometer or endoscope.

The discovery of transistor in 1947 by J. Bardeen, W. B. Shockley and W. H. Brattain at Bell Labs has led to the birth of the microelectronic industry. The miniaturization and mass production of integrated circuits have made such devices as personal computer and mobile phone available for average customers. Their accumulation in households in the last decades was a prerequisite for the internet to become widespread, which has further changed the society.

The distinguishable feature of social life in developed countries at present is the ability to transfer information freely, and to have instant access to information that was difficult or impossible to find previously. One of the important components of this information flow is the ability to store it somewhere. Up to now, no practical universal storage medium exists, and there are several kinds of storage, each with some advantages and drawbacks. The two most important modern ones are the semiconductor memory and hard disk drives.

In a semiconductor memory one bit of information is stored electrically either as a charged or discharged capacitor or as a state of a trigger (i.e., the current flowing through the one or the other transistor). Both variants need power supply to maintain the stored information and belong to volatile storage. The single storage elements are organized into big arrays, with electric lines connected to each of the elements, providing very fast random access to the stored information.

The hard disk drives use thin films of ferromagnetic material on a rigid disk to record data and are of magnetic type of storage. The single bits are represented as a local direction of magnetization in the magnetic material. As the magnetization direction can stay intact for years, the hard disk drives belong to the non-volatile storage class. In order to read or write information from or to the particular region of the disk, the read or write head mounted on the arm have to be moved to the proper radial position of the disk. The desired azimuthal position is achieved by the rotation of the disk. The read head is based on magnetoresistance, which means that the electrical resistance of the material depends upon the strength of magnetic field. The change of the magneti-

zation, needed to write new information, is achieved via a magnetic field produced by a small electromagnet in the writing head. The need of mechanical movements to access particular information causes rather large random access times.

In attempt to overcome the shortcomings and limitations of the existing storage technologies, a number of alternatives to produce universal non-volatile random access memory (RAM) have emerged. One of them is the magnetoresistive RAM. Like hard disk drives, it uses ferromagnetic material to encode binary information ensuring the non-volatility. The single memory cells are arranged, however, into the grid with electrical lines laid to each of the cells, like in the semiconductor memory, providing fast access times. Although the reading via tunnel magnetoresistance is quite efficient in terms of power consumption, the writing is still a problem. All techniques of the cell remagnetization, from the simplest via applied magnetic field to the most advanced using spin transfer torque, require an electric current of different strengths to flow through the cell, which increases the power consumption. In this aspect, the switching of magnetization via applied electric field, without any currents flowing, is very promising. Another possible application of this phenomenon, termed magnetoelectric effect, is in the electrically controllable spin current polarizers, which are required in the emerging field of spintronics.

Similar to magnetic materials, where the lowest lying magnons determine the switching characteristics of magnetic memory cells, the dynamics of the magnetoelectric effect is crucial for the possible magnetoelectric memory cells. Moreover, the elementary excitations in the magnetoelectric media are not well investigated and represent an interesting topic for the fundamental research as well. The spectroscopic study of the rare earth manganites, where the giant magnetoelectric effects were recently discovered [2], is the main topic of this thesis. The next two sections give a short overview of the magnetoelectric effect and the relevant physical properties of rare earth manganites. Chapter 2 provides the theoretical background for the interpretation of experimental data. Details of experimental setup and sample preparation are outlined in chapter 3. The crucial for the understanding results on GdMnO_3 and $\text{Eu}_{1-x}\text{Y}_x\text{MnO}_3$ compounds are summarized in chapters 4 and 5. The chapters 6 and 7 are dedicated to the in-depth investigations of the magnetoelectric excitations in DyMnO_3 and TbMnO_3 , respectively. Chapter 8 concludes the results of the present work and outlines the directions for future research in the field of magnetoelectric excitations.

1.1 Revival of the magnetoelectric effect

The magnetoelectric effect is the induction of magnetization in external electric fields or electric polarization in external magnetic fields inside a material. The coupling between electric and magnetic fields already exists in vacuum as described by the Maxwell equations. However, this coupling is a consequence of the dualism of the electromagnetic field and is not related to material properties.

If the material does not possess any spontaneous polarization \mathbf{P}_0 or magnetization \mathbf{M}_0 , the strongest allowable magnetoelectric effect will be linear. In this case, an exter-

nal magnetic field H induces a proportional electric polarization $P \propto H$, and an external electric field E induces a proportional magnetization $M \propto E$ (see also Fig. 1.1). The fact that such a magnetoelectric effect does not contradict to general symmetry considerations and may exist in some materials with low symmetry was already discussed by Pierre Curie [3]. However, the fundamental symmetry conditions, which are necessary for the existence of the linear magnetoelectric coupling were not established until the late 1950s. Namely, the time and space inversion operations, R and I respectively, are allowed to be among the symmetry elements of the material only in combined form RI [4]. Using these symmetry considerations, the linear magnetoelectric effect was shown to be allowed in Cr_2O_3 [5]. Shortly afterwards this phenomenon was confirmed experimentally [6, 7]. Only after the discovery and theoretical understanding of the magnetoelectric effect, it became clear why it was not discovered until 1960s. Not only the number of materials that obey symmetry conditions is quite limited, but also the experiments have to be carried out on a sample, which possesses a nonequal distribution of magnetic domains (preferably single domain samples). Even then, the strength of the observed effect was very small, compared to conventional susceptibilities, given by $P \propto E$, and $M \propto H$. These problems have led to the decline of research in the field of magnetoelectricity after 1970s. For more information about the history of magnetoelectric effect, see Refs. [8, 9].

Materials which exhibit a static electric polarization \mathbf{P}_0 in the absence of external fields are called ferroelectrics. In the same manner, materials showing spontaneous magnetization \mathbf{M}_0 are called ferromagnets. Electric polarization in the former case and magnetization in the latter case belong to the primary ferroic order parameters. The corresponding materials are termed ferroics. Materials that exhibit more than one primary ferroic order parameter simultaneously (in a single phase) are termed multiferroics. Although other primary order parameters, i.e. strain and, possibly, toroidal moment also exist, only electric and magnetic orders will be considered throughout this thesis. On the other hand, the ordered materials with non-primary order parameters (mostly anti-ferromagnets) do not meet the definition, but are still included into consideration and also called ferroics.

One property of ferroics that makes them suitable for memory applications is their intrinsic ability to retain their state without any external stimuli for prolonged periods of time. The example is the ferromagnetic layer in the hard disk drives mentioned above. Another important aspect of primary ferroic order parameters is their strong interaction with corresponding external fields. For example, the magnetization of the ferromagnet can be switched via applied magnetic field relatively easy. The schematic interrelations between primary order parameters and external stimuli are shown in Fig. 1.1. The left part of the figure depicts external electric \mathbf{E} and magnetic \mathbf{H} fields together with the common methods to produce them via applied voltage U or flowing current I , respectively. In the right part of the figure, electric polarization \mathbf{P} is schematically shown by the surface charges, while magnetization \mathbf{M} is represented by molecular currents. In normal ferroics, only direct control of polarization by the electric field and of magnetization by the magnetic field, shown as black arrows, are allowed. However, in a multiferroic with a magnetoelectric coupling, the cross-control of the polarization via a magnetic field and the magnetization via an electric field are also possible, shown

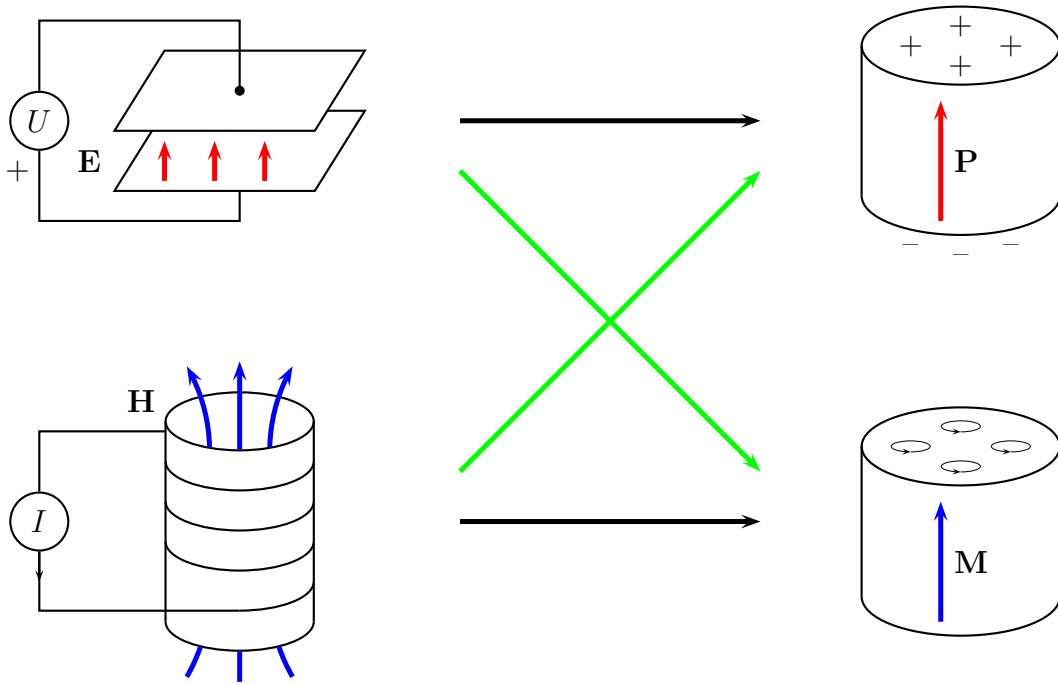


Figure 1.1: Electromagnetic state control in ferroics and multiferroics. The controlling electric \mathbf{E} and magnetic \mathbf{H} fields together with the common methods to produce them via applied voltage U or flowing current I are shown on the left side. The switchable polarization \mathbf{P} and magnetization \mathbf{M} of ferroic materials are shown in the right side. In most ferroic materials polarization \mathbf{P} can only be controlled via external electric field \mathbf{E} and magnetization \mathbf{M} via magnetic field \mathbf{H} (black arrows). In a magnetoelectric multiferroic polarization \mathbf{P} can also be controlled via magnetic field \mathbf{H} and magnetization \mathbf{M} via electric field \mathbf{E} (green arrows).

as green arrows. The latter – electrically switchable magnetization – is of particular interest for applications as was mentioned above.

Although some multiferroics were already known in the period of first investigations of the magnetoelectric effect in 1960s, it is the strong magnetoelectric coupling that was lacking at the time. Not surprisingly, that the discovery of improper ferroelectricity in rare earth manganites in 2003 [2] has led to the revival of the magnetoelectric effect. The ferroelectricity in these compounds emerges only as a consequence of a particular cycloidal magnetic order, which breaks the space inversion symmetry. This directly leads to the intimate coupling between electric and magnetic order parameters in these materials. The representative experimental confirmation of such coupling in TbMnO_3 , reproduced from Ref. [2], is shown in Fig. 1.2. This dielectric material undergoes the antiferromagnetic transition into the incommensurate sinusoidally modulated phase at $T_N \approx 41$ K. The magnetic order transforms into the incommensurate spin cycloid at $T \approx 27$ K. The data shown in the figure are measured in this cycloidal phase. The left panels show the relative change of dielectric constant in external magnetic fields along the crystallographic b axis. The corresponding changes of electric polarization are

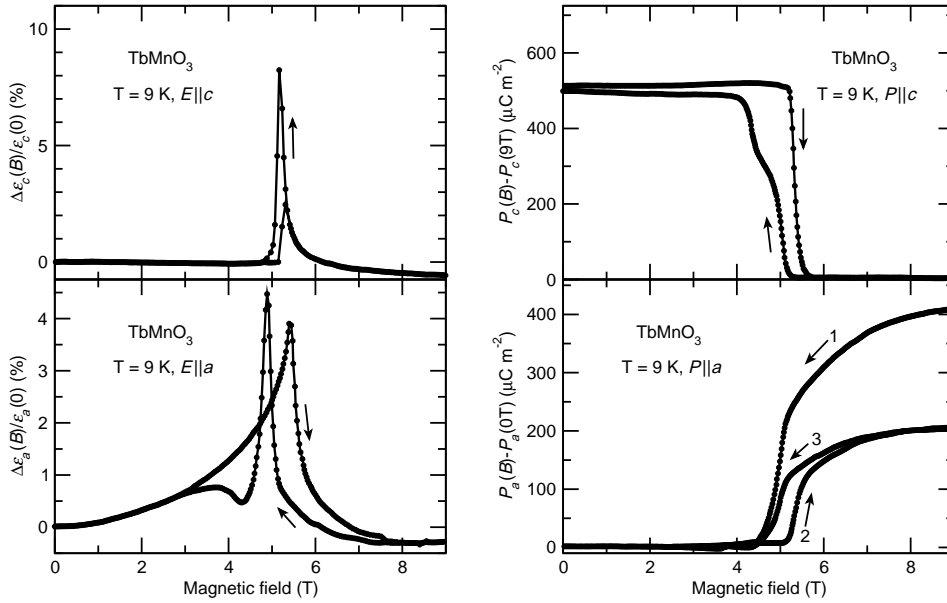


Figure 1.2: Magnetic field dependencies of the dielectric constant (left panels) and electric polarization (right panels) along crystallographic c (upper panels) and a (lower panels) axes in TbMnO_3 . Magnetic fields are applied along the b axis. The switching of electric polarization from c to a axis at magnetic fields of around 5 T (see right panels) represents an example of magnetic control of the electric polarization. The data are taken from Ref. [2].

in the right panels. The upper panels represent the changes of the physical properties along the c axis, the lower panels contain the data along the a axis. At around 5 T, the spin cycloid changes its orientation from the bc to the ac plane. This causes the giant magnetoelectric effect, as the electric polarization, bound to the spin cycloid, switches from the c to the a axis. The dielectric constant exhibits narrow peaks at the transition fields, showing the magnetocapacitance effect. This switching of polarization in external magnetic fields is one example of the magnetic control of the electric properties. Further details of the magnetoelectric coupling in TbMnO_3 and other rare earth orthorhombic manganites will be considered in the next chapter.

After the first pioneering works on multiferroic manganites, there was no doubt that strong magnetoelectric coupling is possible. However, the examples of the electric control of magnetic properties, which are interesting for applications, were still quite rare. One of the reasons is the difficulty in producing electric fields large enough to switch the direction of electric polarization. Another complication on this route stems from the fact that the majority of the magnetoelectric multiferroics possess antiferromagnetic order. The detection of the antiferromagnetic domains is much more difficult than of ferromagnetic ones. One of examples where magnetoelectric effect was observed in both directions in a single phase multiferroic is GdFeO_3 [10]. The antiferromagnetic order in this material has a weak ferromagnetic component along crystallographic c axis. The weak electric polarization develops below $T = 2.5$ K also along the c axis. Figure 1.3, reproduced from Ref. [10], shows the summary of the magnetoelectric coupling in this

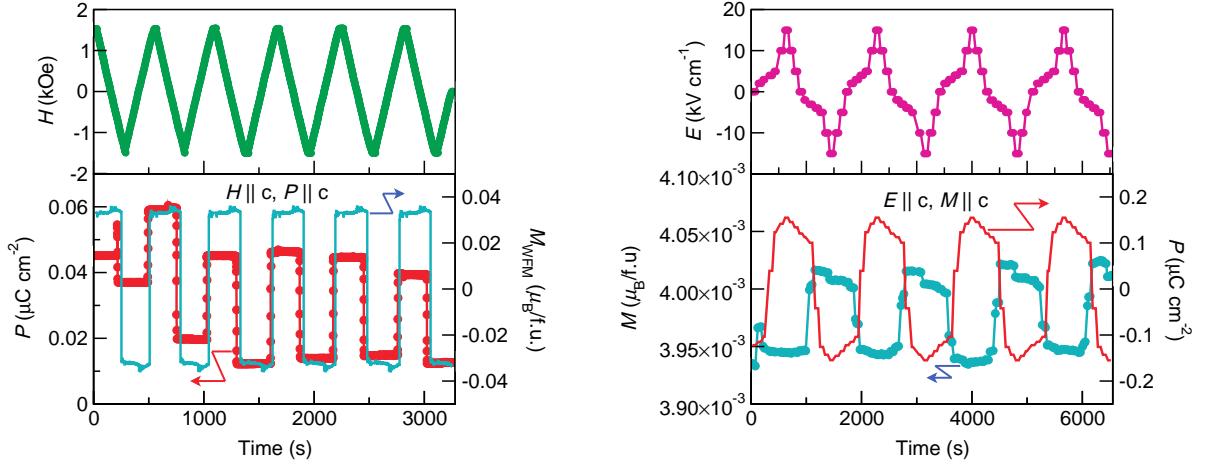


Figure 1.3: Magnetic field induced changes of polarization P and magnetization M at $T = 2$ K in GdFeO_3 (left panels) as the magnetic field H is repeatedly changed between -1.5 and 1.5 kOe (upper panel). The right panels show electric-field-induced changes of P and M at $T = 2$ K as the electric field E is repeatedly changed between -15 and 15 kV/cm (upper panel). All of the vector quantities \mathbf{P} , \mathbf{M} , \mathbf{E} and \mathbf{H} are along the c axis. These experiments demonstrate the mutual controllability of \mathbf{P} and \mathbf{M} with \mathbf{H} and \mathbf{E} in a single phase multiferroic. The data are taken from Ref. [10].

low temperature phase. The left panels demonstrate the temporal evolution of polarization and magnetization (lower panels) as the magnetic field is swept between -0.15 and 0.15 T (shown in the upper left panel). The magnetization is hysteretically changed between two saturation values. The electric polarization shows substantial changes at the same fields as the reversal of magnetization occurs. This demonstrates the mentioned magnetic control of electric polarization. The electrically controlled changes in magnetization are shown in the right panels. Here, again the time dependencies of polarization and magnetization are plotted, but now in external electric field, which changes repeatedly between -15 and 15 kV/cm (shown in the upper right panel). The electric polarization switches between two saturation values and some small changes in magnetization also occur at the same time. The observation of only fractional changes of electric polarization in magnetic fields and quite small changes of magnetization in electric fields is possibly due to the complicated character of the magnetoelectric coupling in this material [10]. Namely, the interaction energy E_{int} has a form of a product of three order parameters, polarization P , magnetization M and a hidden antiferromagnetic order parameter of Gd subsystem, M' : $E_{int} \propto PMM'$. The change of the sign of any two of these order parameters does not change the energy of the system, allowing for the independent changes in P and M . The partial coupling, detected experimentally, is due to the statistical distribution of domain walls and their interaction with each other and with pinning centers.

Complex domain structure and extrinsic lowering of the symmetry on interfaces in thin films also plays an important role in BiFeO_3 , one of the few room temperature multiferroics. Its high ferroelectric ($T_C \approx 1100$ K) and antiferromagnetic ($T_N \approx 640$ K) transition temperatures, well suitable for applications, have stimulated research activ-

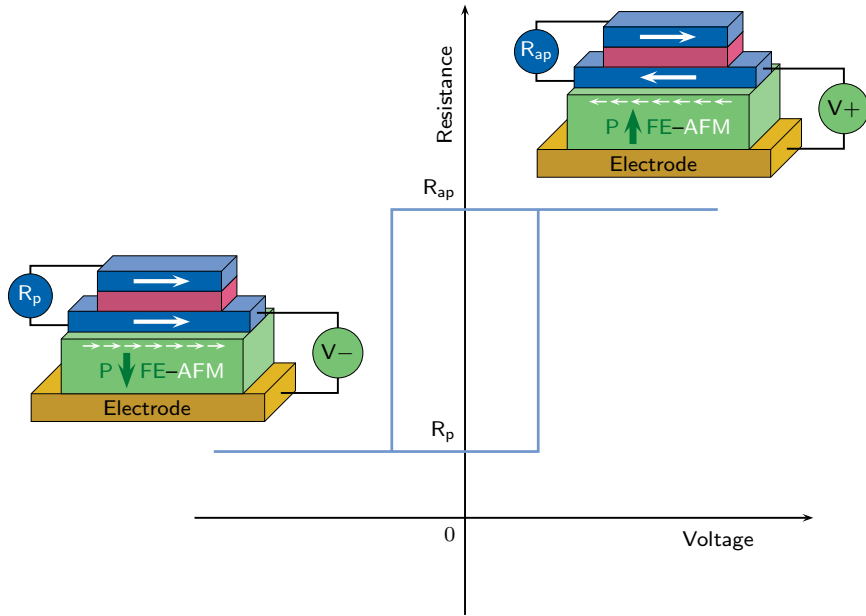


Figure 1.4: Sketch of a possible magnetoelectric random access memory (MERAM) element. The state of the bottom ferromagnetic layer (blue) encodes one bit of information. The bit is read by the resistance of the magnetic trilayer, R_p is the resistance when the magnetizations (thick white arrows) of upper and lower ferromagnetic layers are parallel to each other, and R_{ap} when the magnetizations are antiparallel. To write the bit the voltage V across the ferroelectric-antiferromagnetic layer (green) is applied. The reversal of electric polarization P (green arrow) in the multiferroic also changes its magnetic state causing the spins at the surface (small white arrows) to change their direction. The exchange coupling at the interface switches the magnetization of the lower ferromagnetic layer. The cyan curve demonstrates the suggested hysteretic behaviour of the device. Reproduced from Ref. [11].

ities on this material. The theoretical analysis of the magnetoelectric interaction has indicated that direct electric control of magnetization is hard to achieve [12]. Domains with the same magnetic structure but opposite direction of polarization were shown to be degenerate in the bulk material and unstrained films. However, the partial polarization switching events with, for example, only z component reversed, are also possible in bismuth ferrite. Such switching events are accompanied by the reorientation of the ferroelectric axis and can also change the easy magnetization direction. Indeed, electrically induced changes of the in-plane projection of the antiferromagnetic order parameter were detected experimentally in relatively thick films [13]. In the following experiments, thinner films with simplified domain structure and exchange coupled ferromagnetic layer of CoFe were used to demonstrate the electric control of magnetization [14]. The rotation of the magnetization by 90° in CoFe at room temperature was achieved by the application of the in-plane electric field. Owing to these experiments, the magnetoelectric random access memory (MERAM) cell, that was proposed earlier [15], has become feasible. The sketch of a cell, reproduced from Ref. [11], is shown in Fig. 1.4. Single bit of information is encoded as a magnetization direction of the lower ferromagnetic layer. Due to the exchange coupling to the underlying multiferroic it is possible to switch the

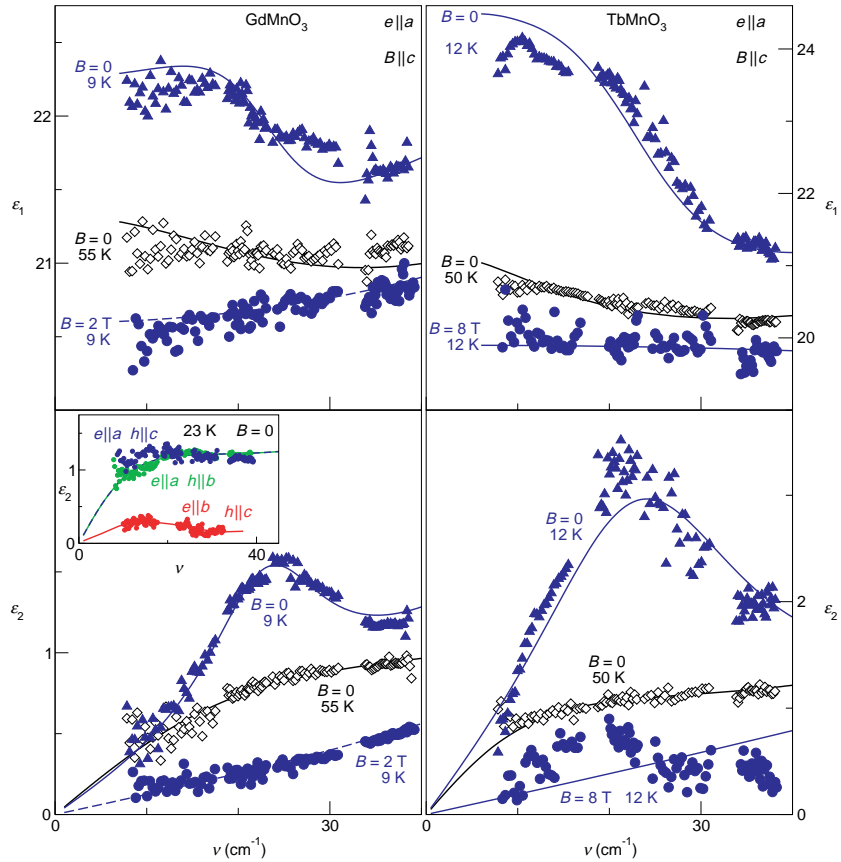


Figure 1.5: Terahertz spectra of the real part (upper panels) and imaginary part (lower panels) of dielectric function in GdMnO_3 (left panels) and TbMnO_3 (right panels). Symbols represent experimental data, solid lines – fits with Lorentzians. The novel excitation, called electromagnon, arises in both materials in a magnetically ordered (spin cycloidal) state (absorption maxima in the lower panels at $T = 9\text{--}12\text{ K}$ and $B = 0$, blue triangles, compare with the high temperature data, black diamonds). The inset demonstrates the electro-dipole activity ($e||a, \tilde{h}$ -independent) of electromagnons. The application of magnetic field along the c axis suppresses the cycloidal spin order and causes the electromagnons to disappear, demonstrating their magnetic origins (the data at $B = 2\text{ T}$ for GdMnO_3 and at $B = 8\text{ T}$ for TbMnO_3 , blue circles). The data are taken from Ref. [16].

magnetization via applied voltage, as described above. The state of the cell is read out as a magnetoresistance of the trilayer, where the upper ferromagnetic layer has the fixed direction of magnetization.

The discussion of magnetoelectric multiferroics has concerned only the quasistatic properties so far. The high frequency characteristics are also of great interest, both for applications and fundamental research. On the one hand, the lowest lying excitations will determine the performance of magnetoelectric memory. On the other hand, it is not clear if the presence of magnetoelectric interaction will only slightly renormalize the existing excitations, or if completely new ones will arise. The last question was first considered theoretically in the period of first magnetoelectric studies [17, 18]. The strong mixing of polar (phonons) and magnetic (magnons) excitations was found to exist

only at nonzero wave vectors, when their frequencies coincide. At small wave vectors, relevant for spectroscopic studies, the admixture of electric component to the magnetic excitations and vice versa were small due to large difference of bare resonance frequencies. The first experimental signs of mixed magnetoelectric excitations were detected in GdMn_2O_5 [19]. In this work an increased absorption around 140 GHz was observed at the multiferroic transition temperature. However, it remained unclear, whether these excitations retain their magnetoelectric nature in the ground state at lowest temperatures. The cornerstone of the magnetoelectric dynamics was the observation of broad and very intensive absorption modes in the already mentioned rare earth manganites GdMnO_3 and TbMnO_3 [16]. The most important results of this work are reproduced in Fig. 1.5. The left panels show the data for Gd manganite, the right panels - for Tb manganite. The imaginary part of dielectric constant ε_2 , responsible for the absorption of radiation, is shown in the lower panels. The electrically and magnetically unordered phase above 45 K is characterized by the broad absorption plateau in both materials (black open symbols in Fig. 1.5). The absorption gradually rises upon cooling and transforms into broad peak around 20 cm^{-1} in the cycloidal phase at $T < 15 \text{ K}$ (blue triangles). This high frequency excitation is also visible as a step-like feature in the real part of dielectric constant ε_1 , plotted in the upper panels.

The inset in the lower left panel of Fig. 1.5 shows the data for various orientations of radiation relative to crystallographic axes. Such a polarization analysis allows to unambiguously determine the selection rules for the novel excitation. The absence of substantial absorption in the geometry represented by red colour means that the mode can be excited neither by magnetic field oriented along c axis nor by electric field along b axis. On the other hand, the presence of the mode in the geometry corresponding to the blue colour evidences its excitation by either magnetic field along c axis or electric field along a axis. This leaves only electric field along a axis as a selection rule showing electric nature of this excitation. The application of a magnetic field along crystallographic c axis is known to suppress the spin cycloid and spontaneous electric polarization in these materials [20]. At the same time, the novel excitation disappears in these conditions (blue circles in Fig. 1.5) pointing to the magnetic nature of the mode. The closeness of the resonance frequency of these excitations (20 cm^{-1}) to the typical frequencies of magnons together with the pure electric selection rules have led to the name *electromagnons*. The observation of electromagnons in orthorhombic rare earth manganites is supplemented by the rich possibilities to influence their properties in external magnetic fields. This combination makes these materials good model systems for studying the magnetoelectric dynamics.

1.2 Rare earth manganites RMnO_3

All orthorhombic rare earth manganites have a common crystal structure, but nevertheless exhibit different magnetic orderings. Only a few of them with a particular cycloidal spin arrangement, which causes ferroelectricity, are the main topic of the present thesis. It is instructive, however, to consider first a broader range of materials on both sides of

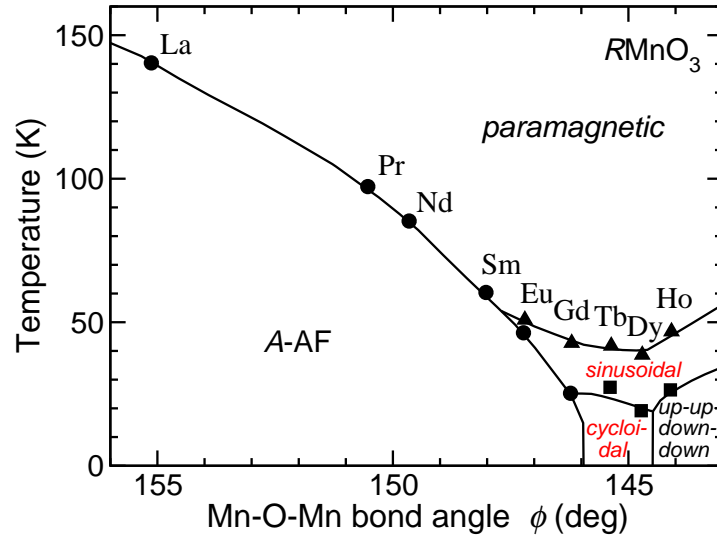


Figure 1.6: Mn-O-Mn bond angle magnetic phase diagram of rare earth manganites $RMnO_3$. Materials with La, Pr, Nd and Sm show the single transition into the antiferromagnetic A-type phase. Rare earth manganites starting with Eu possess an intermediate incommensurate sinusoidally modulated phase. The low temperature phase for $EuMnO_3$ is A-type antiferromagnet, for Tb and Dy rare earths - cycloidal incommensurate order, and for Ho manganite - so called “up-up-down-down” commensurate spin order. Depending on a magnetic history, the samples of $GdMnO_3$ can show both A-type or sinusoidal spin structures. The ordering effects of rare earth spins are neglected here. The data are taken from Ref. [21].

cycloidal order in the phase diagram Fig. 1.6. This allows to establish crucial trends in a series of rare earth manganites that lead to the formation of frustrated cycloidal spin structure. The considerations in this section, being qualitative in nature, help to better understand the physical phenomena involved.

1.2.1 Crystal structure

Orthorhombic rare earth manganites are characterized by the same perovskite structure with $GdFeO_3$ -type distortions. Before considering the real structure, it is easier to start with the ideal cubic arrangement, shown in Fig. 1.7. It is possible to construct the perovskite ABO_3 from the alternating layers of BO_2 and AO . These layers, viewed from the top, are shown in the two bottom frames of Fig. 1.7. The front view of the structure, highlighting the positions of BO_2 and AO layers, is represented in the upper two frames. Oxygen atoms are shown as small magenta circles, “B” atoms - as medium blue circles and “A” atoms - as large green circles. Although the cubic structure has the same lattice constants in all three dimensions, crystallographic axes are marked as different and rotated by 45° in the ab plane to coincide with the orthorhombic setting in Fig. 1.8. The cubic unit cell is marked by the solid gray line. In both upper frames and the lower left frame it coincides with the B-O bonds shown as a black lines. The B-O bonds form the diagonals of BO_6 octahedron, which is better seen in the projection of three dimensional view on the right side of Fig. 1.7. Here, the octahedron is shown by both black diagonals and cyan edges, together with the directions of orthorhombic axes. As

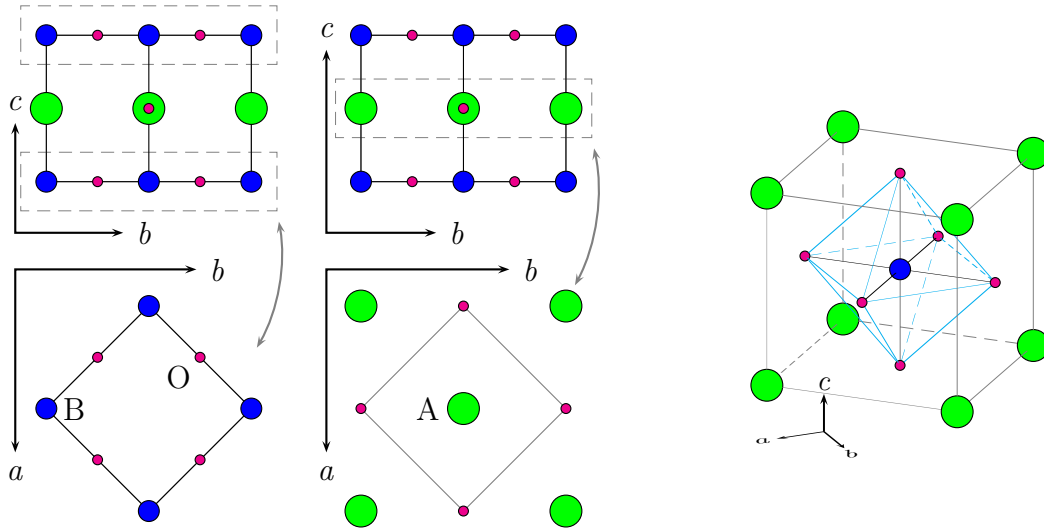


Figure 1.7: Crystal structure of an ideal cubic perovskite ABO_3 . Projections of different atomic layers into bc and ab planes in the $Pbnm$ setting are shown in the left part. Upper two frames are the front views of the three dimensional structure, lower two frames are the top views of BO_2 (left frame) and AO (right frame) layers. Large green circles denote the A ions, medium blue circles - the B ions and small magenta circles represent the oxygen ions. Gray lines show the boundary of the unit cell. The cell boundary coincides with B-O-B bonds, shown as black lines, in both upper, and lower left views. B-O bonds form diagonals of BO_6 octahedron, which is highlighted by cyan lines in the three dimensional projection in the right part of the figure.

will be shown below, the octahedral environment of Mn atoms plays an important role for magnetic properties in rare earth manganites.

The real perovskite structures are nearly never perfectly cubic. The reason is that it is hard to fulfil the relation between the radii of “A” and “B” ions, which is required for the cubic lattice. In the case of rare earth manganites the radius of the rare earth ion is rather small. This leads to the so-called GdFeO_3 -type distortions. These distortions basically consist of a complex tilting of MnO_6 octaedra in order to fill extra space around the rare earth ion. They are represented in Fig. 1.8, which shows the crystal structure of TbMnO_3 . The positions of atoms are plotted on a scale, the sizes of ions are reduced for the sake of clarity. The top views of MnO_2 and TbO layers, that are parallel to the ab plane, are in the lower panels, the front view of the structure is repeated in the upper panels. The unit cell, marked by solid gray lines, is doubled along the c direction and is increased by a factor of $\sqrt{2}$ with simultaneous rotation by 45° in the ab plane in comparison with the cubic structure. The upper left panel highlights the tilting of one MnO_6 octahedron, shown by its edges in cyan. Considering magnetic properties, there is another much more important distortion of MnO_6 octaedra. It is best seen in the lower left panel of Fig. 1.8, where MnO_4 sections of two octaedra are depicted by cyan lines. Namely, the distances between Mn and O atoms are different for two diagonals of MnO_4 sections. Direct calculations from the atomic positions [22] in case of TbMnO_3 give 1.88 \AA for the shorter Mn-O bond in the MnO_2 plane, 1.93 \AA for Mn-O bond in the c direction and 2.28 \AA for the longer Mn-O bond in the MnO_2 plane. The direction of the

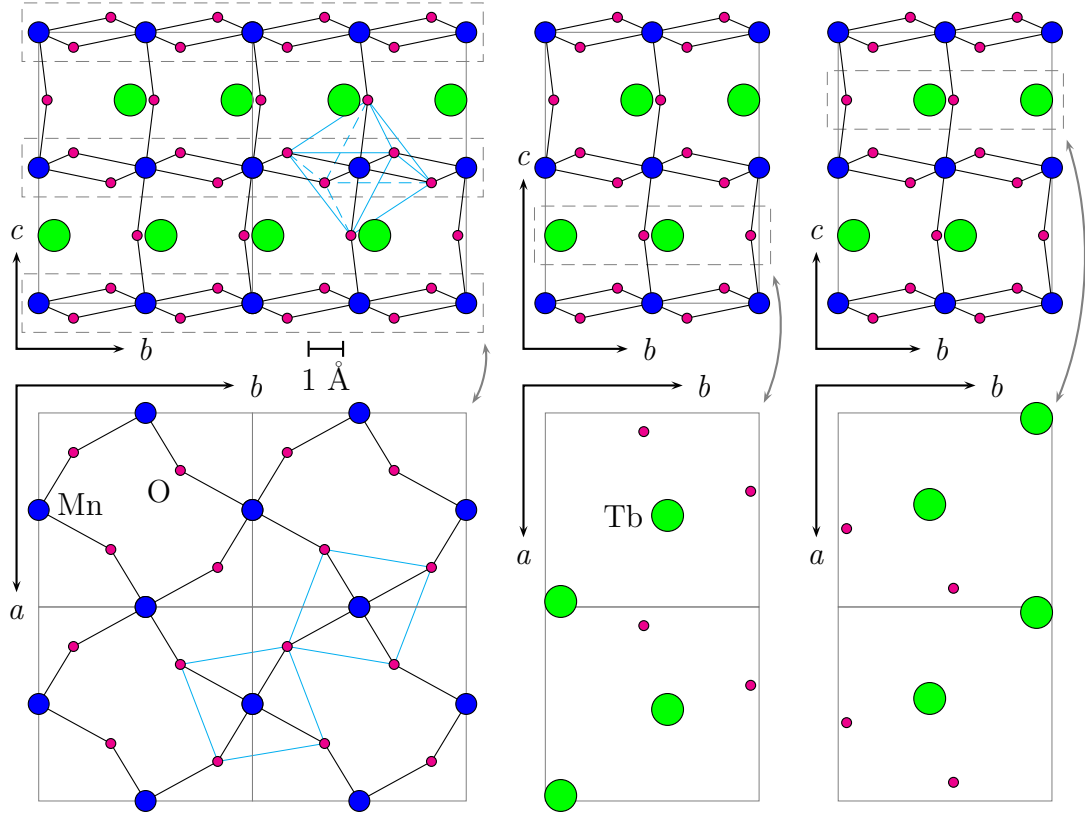


Figure 1.8: Crystal structure of the orthorhombic rare earth manganites $RMnO_3$ with $R = Tb$ as an example. The same type of projections into the crystallographic bc and ab planes in $Pbnm$ setting is used as in Fig. 1.7. Big green circles - rare earth ions, medium blue circles represent Mn ions and small magenta circles are oxygen ions. Gray lines mark the border of the unit cell, black lines represent the Mn-O bonds. Two different types of TbO planes are shown in the right frames. Two MnO_2 planes differ only in the positions of oxygen atoms along the c direction and result in the same ab view (lower left frame). The whole MnO_6 octahedron is represented by cyan lines in the upper left frame, which demonstrates the tilting of MnO_6 octahedra due to size mismatch of the rare earth ion. MnO_4 sections of two MnO_6 octahedra, shown in the lower left frame, visualize the elongations of the one side of octahedra in alternating directions due to Jahn-Teller effect.

longer diagonal alternates from one octahedron to the other. This phenomenon, which is called cooperative Jahn-Teller distortion, will be discussed in more details below.

Summarizing the structural properties of rare earth manganites, the lattice constants of relevant compounds are shown in Table 1.1. The designation of the axes is the same as in Fig. 1.8 and is given in the nonstandard $Pbnm$ setting of the space group # 62, as it is common in the literature. Whenever available, the atomic positions were used to calculate Mn-O-Mn angle ϕ of the bonds in the ab MnO_2 planes. This angle plays an important role in determining magnetic ground state and it is used in the phase diagram Fig. 1.11. The data for pure compounds $EuMnO_3$ and $GdMnO_3$ are taken from Ref. [23], and for $TbMnO_3$, $DyMnO_3$ and $YMnO_3$ - from Ref. [22]. The lattice parameters of the solid solutions $Eu_{1-x}Y_xMnO_3$ for $x = 0, 0.1, 0.2, 0.3$ and 0.5 are taken from Ref. [24],

Material	a [Å]	b [Å]	c [Å]	ϕ [°]
EuMnO_3	5.340	5.866	7.448	146.47
GdMnO_3	5.318	5.866	7.431	145.98
TbMnO_3	5.293	5.838	7.403	145.36
DyMnO_3	5.279	5.834	7.378	144.70
YMnO_3	5.242	5.803	7.364	144.49
$\text{Eu}_{1.0}\text{Y}_{0.0}\text{MnO}_3$	5.345	5.864	7.458	146.47
$\text{Eu}_{0.9}\text{Y}_{0.1}\text{MnO}_3$	5.337	5.864	7.447	146.27
$\text{Eu}_{0.8}\text{Y}_{0.2}\text{MnO}_3$	5.331	5.868	7.438	146.07
$\text{Eu}_{0.7}\text{Y}_{0.3}\text{MnO}_3$	5.320	5.860	7.428	145.88
$\text{Eu}_{0.6}\text{Y}_{0.4}\text{MnO}_3$	5.307	5.843	7.415	145.68
$\text{Eu}_{0.5}\text{Y}_{0.5}\text{MnO}_3$	5.304	5.856	7.409	145.48

Table 1.1: Structural parameters of some orthorhombic rare earth manganites. The lattice constants a , b and c are given in $Pbnm$ crystallographic setting. The Mn-O-Mn bond angle ϕ in the MnO_2 planes is calculated from the atomic positions for the pure compounds and then interpolated for the Eu-Y mixture. The data are taken from Refs. [22, 23, 24, 25] (see text for details).

and from Ref. [25] for $x = 0.4$. As there were no data for atomic positions in the family of $\text{Eu}_{1-x}\text{Y}_x\text{MnO}_3$, linear interpolation between pure EuMnO_3 and YMnO_3 was used to obtain Mn-O-Mn bond angle.

1.2.2 Jahn-Teller effect and orbital order

MnO_6 octaedra in rare earth manganites are stretched along one of their diagonals. This stretching is called Jahn-Teller effect [26] and is caused by the interaction of Mn $3d$ electrons with the potential of the surrounding oxygen ions. This phenomenon occurs only if the undistorted state of Mn is orbitally degenerate and, therefore, depends strongly on the number of $3d$ electrons on manganese ions. The element valencies in rare earth manganites are $\text{R}^{3+}\text{Mn}^{3+}\text{O}_3^{2-}$, leaving four $3d$ electrons on Mn sites.

If the effective negative charge of oxygen atoms would be homogeneously distributed on a sphere around Mn, the energy levels of $3d$ electrons would rise, but still they would be degenerate. The wave functions of these states are the well-known atomic orbitals, which can be characterized by orbital number $l = 2$ and magnetic number $m = 0, \pm 1, \pm 2$. This case correspond to the spherical environment on the left side of Fig. 1.9. If the charges are localized on the real positions of oxygen atoms, the reduced symmetry of their potential can lift the degeneracy of $3d$ states. The eigenstates will also change and should be first constructed from the linear combinations of original atomic orbitals. In the case of octahedral environment they are symmetric and antisymmetric superpositions of two $m = \pm 2$ orbitals, symmetric and antisymmetric combinations of $m = \pm 1$ orbitals and $m = 0$ orbital (see middle part of Fig. 1.9). It is easy to see that the wave functions of three of new states point towards edges of octahedron (t_{2g} states) and of two other states - towards verticies (e_g states). If the charges are held at the same

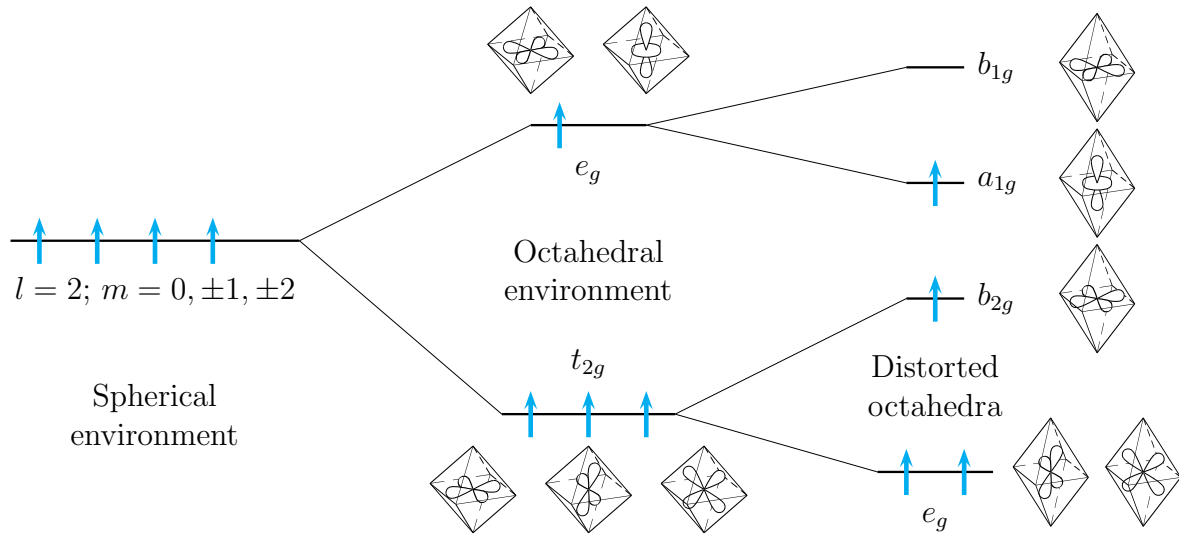


Figure 1.9: Splitting of 3d energy levels in the crystal field. Five degenerate energy levels of atomic 3d orbitals in equivalent spherical field are shown in the left part of the figure. Localizing the ligand charges in the octahedral arrangement lifts fivefold degeneracy into threefold t_{2g} and twofold e_g energy levels (middle of the figure). Stretching of octahedron along one direction with simultaneous compression within perpendicular plane splits the energy levels further into twofold e_g and non degenerate b_{2g} , a_{1g} and b_{1g} levels, shown in the right part of the figure. For the four 3d electrons of Mn^{3+} ion, represented by cyan arrows, the tetragonal distortion is favourable as it lowers the total energy of the system.

distance from Mn atom and only redistributed towards the vertices of the octahedron, e_g states would interact more with the repulsive potential and rise in energy, while t_{2g} states would fall. The average energy of all five levels would be approximately the same as the single degenerate level before redistribution.

The effect, as described above is called the crystal field splitting. The magnitude of this splitting in manganites is smaller than the Hund energy, which results from the Coulomb repulsion between two electrons with the opposite spins, placed on the same orbital. Therefore, the state of Mn^{3+} ion with four electrons will be as shown in the middle part of Fig. 1.9, first filling all different orbitals with single electron. The total spin of such arrangement is $S = 2$ (high spin configuration). Octahedral environment breaks spherical and cylindrical rotational symmetries, therefore, the orbital moment is no longer a preserved quantity. Indeed, the new eigenstates are formed from orbitals with the opposite magnetic numbers and projection of orbital moment on a predefined direction is zero for all new states. Although another basis of eigenstates could be chosen for t_{2g} levels, and they have a pseudo-orbital moment with effective $l = 1$, they are all filled for Mn^{3+} ion and the orbital moment can still be assumed to be fully quenched in rare earth manganites.

Let us assume now that two opposite oxygen atoms in the MnO_6 octahedron are moved away from Mn atom, while four other oxygen atoms in the plane perpendicular to this diagonal are moved toward the center by amount needed to conserve the volume of the octahedron. The elastic energy required for the distortion out of equilibrium position

is quadratic in the magnitude of displacements. According to similar considerations as above, t_{2g} levels will split into e_g and b_{2g} levels, and e_g states - into a_{1g} and b_{1g} (right side of Fig. 1.9). The average energy of new e_g and b_{2g} levels will be roughly the same as the former t_{2g} level, so there will be no change in the total energy of three electrons in these states. The average energy of a_{1g} and b_{1g} levels will also be the same as the former e_g level, but as only lower state is occupied, there will be a gain in the total energy of the whole system. This energy gain could be shown to be linear in the magnitude of displacements, so that the distorted state is always more favourable than the symmetrical octahedral arrangement. This is a loose application of Jahn-Teller theorem [26]. It states that for any configuration of atoms not lying on a straight line and being in a degenerate state, a distortion will occur that will lift the degeneracy.

Thus far, only one MnO_6 octahedron was considered. However, each oxygen atom is a shared vertex of two octaedra in the perovskite lattice (see Fig. 1.8). The collective distortions of MnO_6 octaedra are called cooperative Jahn-Teller effect in this case. In the rare earth manganites it occurs in the MnO_2 layers, parallel to the ab plane, with the alternating direction of the elongated diagonals. As the last occupied orbital is oriented along these diagonals, such an arrangement leads to the orbital order, shown in the left panel of Fig. 1.10. Blue orbitals represent the filled a_{1g} Mn states, gray orbitals - empty b_{1g} Mn states, and small magenta orbitals - filled p states of oxygen ions, which are directed along the Mn-O-Mn bonds. As can be seen, the oxygen orbitals always connect one filled with one empty Mn orbitals in the ab plane. This is different from the pattern in the crystallographic c direction, shown in the right panel of Fig. 1.10. Only empty b_{1g} orbitals with the larger extent along the c axis are shown here. Now, the p orbitals of oxygen atoms connect empty manganese states. Such orbital anisotropy leads to the anisotropic exchange interaction between Mn spins, which is considered below.

The orbital order can be destroyed by high temperatures as shown in the upper panel of Fig. 1.11. The transition temperatures, as detected by the drop in resistivity, are plotted by open black circles. The structural transition at the same temperature $T \approx 750$ K in LaMnO_3 was also detected by the neutron diffraction [27]. The lattice parameters become cubic above this temperature, so that $a' = c/2 = a/\sqrt{2} = b/\sqrt{2}$ is the pseudocubic spacing. The point symmetry remains orthorhombic, however, indicating that the Jahn-Teller effect becomes dynamic. Increasing the atomic number of rare earth element decreases its ionic radius and enhances GdMnO_3 -type tilting of MnO_6 octaedra (seen as a decrease of Mn-O-Mn bond angle from the cubic 180°). As the transition temperature to the orbital disordered state steadily increases and cannot be detected for elements heavier than Sm at all, the orbital order seems to be stabilized in strongly distorted rare earth manganites.

1.2.3 Magnetic interactions and phase diagram

Some qualitative predictions about expected exchange interactions in rare earth manganites can be obtained within the Hubbard model [28], which accounts for two main interactions: the on-site Coulomb repulsion U , when two electrons with opposite spins are put into the same orbital, and the hopping energy t which stems from the overlap

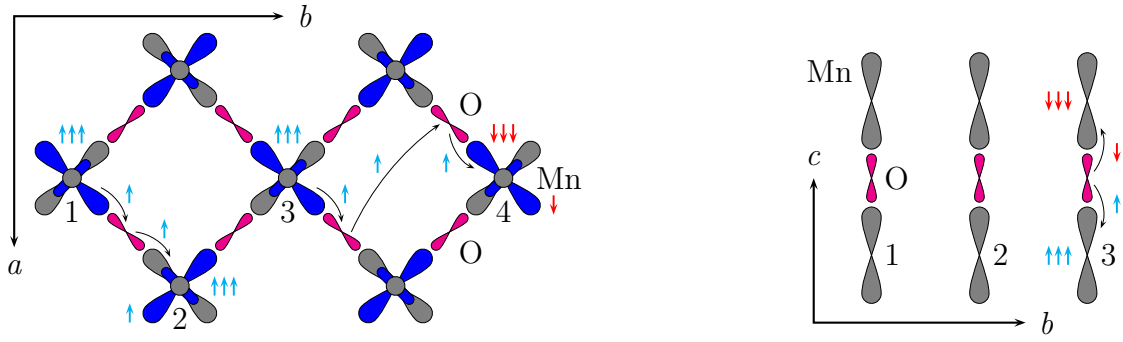


Figure 1.10: Orbital order in rare earth manganites. The alternating order of filled a_{1g} (blue) and empty b_{1g} (gray) orbitals in the MnO_2 planes is shown in the left frame. Cyan or red arrows denote electron spins. The groups of three arrows represent low lying e_g and b_{2g} electrons. Single arrows correspond to a_{1g} electrons which can virtually hop into nearest and next-nearest neighbours. The exchange interaction between nearest neighbour orbitals ($\text{Mn}(1)\text{-O-Mn}(2)$ path) is ferromagnetic, according to Goodenough-Kanamori-Anderson rules. The next-nearest neighbour exchange interaction (along $\text{Mn}(3)\text{-O-O-Mn}(4)$ path) is expected to be antiferromagnetic, as the hopping occurs between filled orbitals. The order along c axis is depicted in the right panel. Here, only the most relevant for the exchange empty b_{1g} orbitals are shown. The expected exchange between empty orbitals is antiferromagnetic.

of atomic orbitals in the crystal. In the case $t \gg U$, the model system is metallic with the width of conduction band of the order of t . On the other side, when $U \gg t$, the system is in the state known as a Mott-Hubbard insulator with the energy separation between the first excited states and the ground state of the order of U . The latter is a good approximation in the rare earth manganites which are all good insulators. In zero approximation, electrons are distributed according to the formal valencies of elements, so all oxygen ions are completely filled and manganese ions have four $3d$ electrons. The hopping term t is introduced as a small perturbation. The consideration of the perturbed state with a small admixture of the excited states, which have some electrons “hopped” to another atoms (sites), leads to the corrections of the second order in t . These corrections strongly depend on the orientations of spins on different sites and are proportional to the effective exchange constants J . Performing the actual calculations for the systems with multiple occupied and empty orbitals is rather involved, even within the Hubbard model. In the case of indirect hopping via oxygen orbitals they have led to the formulation of the semi-empirical Goodenough-Kanamori-Anderson rules [29]. What follows is the application of these rules to rare earth manganites. The hopping processes leading to the admixed excited states are not the only allowed in each case, and they are presented only to visualize the expected exchange interactions.

Exchange interaction between nearest neighbour filled and empty Mn sites ($\text{Mn}(1)\text{-O-Mn}(2)$ path in the left panel of Fig. 1.10) is expected to be weakly ferromagnetic. The electron with either spin can hop from the filled oxygen orbital to the empty orbital of $\text{Mn}(2)$. The electron with the same spin can now move from the filled $\text{Mn}(1)$ state into the released oxygen orbital so the whole process looks like electron from the filled $\text{Mn}(1)$

orbital has hopped to the empty Mn(2) orbital. Energy correction in the second order of perturbation theory depends inversely on the energy of the excited state. The energy of the state, when all electrons on Mn(2) site have the same direction of spin (as shown in Fig. 1.10) is lower than for the state with one spin reversed. Therefore, the energy gain is larger for spins on Mn(1) and Mn(2) atoms aligned parallel to each other, which can be described by effective ferromagnetic exchange constant J .

As the GdFeO_3 distortion of perovskite structure increases, the distance between one pair of the opposite oxygen atoms in the ab MnO_2 planes decreases, while for the other pair increases (see Fig. 1.8). This can lead to the hopping processes along the shortened O-O path and next-nearest neighbour exchange interaction between Mn spins. Due to superimposed orbital order, this interaction will be stronger along the b axis and is represented by Mn(3)-O-O-Mn(4) path in Fig. 1.10. As the exchange is taking place between two filled orbitals it is expected to be antiferromagnetic. The electron from the filled oxygen orbital can hop into the filled Mn(4) orbital only if it has the opposite spin relative to electrons in on the Mn(4) site. The formed vacancy can be filled by the electron with the same spin from the other oxygen site, and the new vacancy - in turn by the electron from Mn(3) filled orbital. Such a process leads to the largest energy gain in the case of antiparallel spin alignment on Mn(3) and Mn(4) sites, which can be described by the effective antiferromagnetic exchange constant J_{nnn} .

Along the c axis, exchange interaction takes place between two empty Mn $3d$ orbitals and is expected to be antiferromagnetic (schematically shown in the right panel of Fig. 1.10). Here, one electron from the filled oxygen orbital can hop into one Mn site, while the other electron - into the other Mn site. As the same orbital can only have electrons with different spins, the energy gain from the exchange will be larger for antiparallel spin orientation on the different Mn sites. This interaction is described by the effective antiferromagnetic exchange constant J_c .

It is possible now to describe the magnetic phase diagram of rare earth manganites in the lower panel of Fig. 1.11, at least qualitatively. Solid circles denote the transition temperature into A -type antiferromagnetic state (see also Fig. 1.12), solid triangles - into incommensurate sinusoidally modulated state, and solid squares - into cycloidal or “up-up-down-down” states. The dependence on the rare earth element is presented by the Mn-O-Mn bond angle ϕ . The data for pure compositions, shown by the black color, is taken from Ref. [21]. In order to obtain the bond angle ϕ , the authors of the last paper have used atomic positions from Ref. [22] for pure compositions except Sm, Eu and Gd manganites. For the last three compounds, a linear interpolation between NdMnO_3 and TbMnO_3 was used. The data for solid solutions of $\text{Eu}_{1-x}\text{Y}_x\text{MnO}_3$, plotted by the green color, is the same as in Fig. 5.1, and is taken from Ref. [30]. The ϕ values for EuMnO_3 and YMnO_3 are calculated from the atomic positions and the linear interpolation is then used for intermediate compositions. The different procedures to obtain bond angle ϕ for pure EuMnO_3 is the reason of the discrepancy between corresponding black and green symbols.

If the nearest neighbour interaction within ab planes dominates, the spins will align in ferromagnetic layers. The stacking of these layers along the c direction is antiferromagnetic, leading to the A -type antiferromagnetic order, in the notation of Wollan and

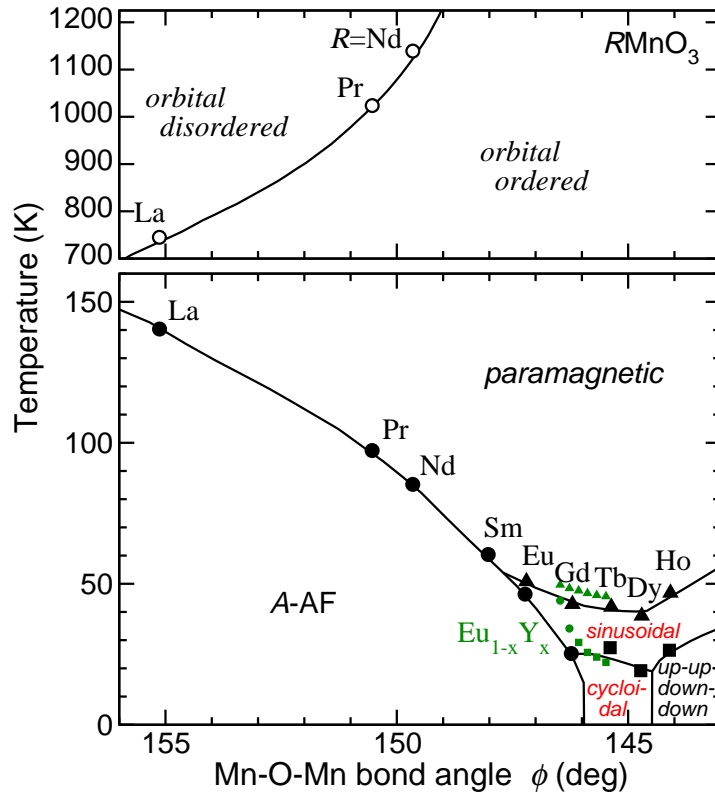


Figure 1.11: Mn-O-Mn bond angle phase diagram of rare earth manganites $RMnO_3$. Upper panel shows the dependence of transition temperatures from the orthorhombic orbital ordered phase to the pseudocubic orbital disordered phase upon bond angle ϕ . No transition was detected for rare earths Sm to Ho. Lower panel demonstrates the magnetic phase diagram. Black points were obtained for pure compositions, green points are for $Eu_{1-x}Y_xMnO_3$ solid solutions. Compounds with La, Pr, Nd and Sm show the single transition into the antiferromagnetic A-type phase. Rare earth manganites starting with Eu possess intermediate incommensurate sinusoidally modulated phase. The low temperature phase for $EuMnO_3$ is A-type antiferromagnet, for Tb and Dy rare earths - cycloidal incommensurate order, and for Ho manganite - so called “up-up-down-down” commensurate spin order. Depending on magnetic history, the samples of $GdMnO_3$ can show both A-type or sinusoidal spin structures. The ordering effects of rare earth spins are neglected here. The data for open and closed black symbols and black lines are taken from Ref. [21], the data for the green points - from Ref. [30] and Table 1.1.

Koehler [31] (see the left panel of Fig. 1.12). This is the case for rare earth manganites on the left part of the phase diagram with the small distortion of the structure and negligible next-nearest neighbour interaction. Moving to the other side of the phase diagram, Mn-O-Mn bond angle decreases from 180° , optimal for the ferromagnetic nearest neighbour exchange. Therefore, the ferromagnetic exchange constant J will decrease. On the other hand, the increased distortions shorten the distance between one pair of oxygen atoms, increasing the antiferromagnetic Mn-O-O-Mn interaction. If the next-nearest neighbour interaction dominates in the ab planes, the spins will tend to form two antiferromagnetic sublattices, embedded one into other with almost absent interaction between them. The presence of single ion anisotropy (easy axis) can stabilize the so-called “up-up-down-down” spin order (shown in the right panel of Fig. 1.12),

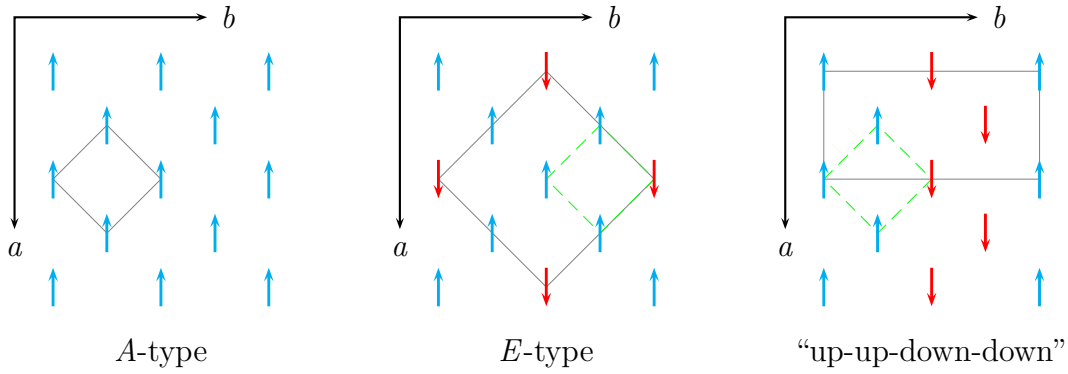


Figure 1.12: Commensurate spin structures relevant for rare earth manganites. Only spin arrangements within ab planes are shown. The order along the c axis is simple antiferromagnetic for all types. Gray lines mark the border of the magnetic unit cell in the ab plane. The designations for A - and E -types were given in Ref. [31]. The name “up-up-down-down” comes from the spin order encountered by following Mn zigzag chains along b axis. E -type and “up-up-down-down” spin structures look the same on the scale of the simplest cubic cell (marked by green dashed line), which was probably the reason for the misidentification in Ref. [21] (see text for details).

observed in HoMnO_3 . In the intermediate case, the strong spin frustration is present within the ab layers, leading to a formation of novel cycloidal state at low temperatures. The details of this frustrated spin order is the topic of the next chapter.

The last remark that has to be mentioned concerns a misidentification of “up-up-down-down” as an E -type antiferromagnetic order. This mistake is present in Ref. [21], but it has been corrected in Fig. 1.11. The patterns within ab planes for A -, E -type and “up-up-down-down” spin orders are schematically shown in Fig. 1.12. The directions of spins are chosen arbitrarily, and can be different in the real magnetic structures. Both A - and E -types of antiferromagnetic order were proposed to describe magnetic phases in the $\text{La}_{1-x}\text{Ca}_x\text{MnO}_3$ doped compounds [31]. The magnetic unit cell of these structures requires at most doubling of the simplest cubic cell along all three directions, and is marked in Fig. 1.12 by solid gray lines. It is clearly seen that the E -type and “up-up-down-down” spin arrangements are different. The possible source of the misidentification could be the fact, that the simplest square blocks of both spin structures look very much alike: they always contain three spins in one direction and one spin - in the other.

2 Magnons

In a crystal lattice a small displacement of atoms from their equilibrium positions causes forces that tend to bring atoms back. Due to inertia of atoms such displacements are accompanied by the oscillations of atoms in the vicinity of their equilibrium. As the atoms are coupled with each other, the full set of equations of motion has to be solved to obtain the oscillation modes which are called *phonons*. These collective oscillations have a form of plane waves characterized by the frequency ω , wave vector \mathbf{q} and the polarization (direction of the movement). Relations connecting ω with \mathbf{q} are called dispersion relations and they depend on the parameters of the crystal lattice. If there are atoms which carry nonzero electric charge, some of these waves result in electric dipole moment that is not vanishing after averaging across the whole crystal. The oscillating electric moment of such *optical phonons* can interact with the oscillating electric field of the same frequency causing resonant absorption of light. In other words, optical phonons are responsible for the *electro-active* absorption in optical spectroscopy. Note that due to very high speed of light the electromagnetic waves of matching frequency have almost zero wave vector and optical phonons are located at the point with $\mathbf{q} \approx 0$ on the dispersion relation.

Analogously to the crystal lattice, magnetically ordered material additionally forms a spin lattice. Small oscillations of spins around their equilibrium orientations also have a form of plane waves and are called *magnons*. Magnons with nonvanishing average magnetization can also interact with electromagnetic waves but via an ac magnetic field. Depending on the magnetic ground state such optical magnons are termed either *ferromagnetic resonances (FMR)* or *antiferromagnetic resonances (AFMR)*. Therefore the magnons are responsible for the *magneto-active* absorption. In materials with magnetoelectric interaction however, magnons can gain electric activity (and phonons - magnetic). This is definitively the case in rare earth manganites and comprises the main topic of this thesis.

The purpose of this section is to show the crucial properties of magnons on a set of simple model systems building the theoretical basis for further experimental investigations. As the cycloidal magnetic structure in the ground state of frustrated manganites is rather complex, we start with simple models then discuss more complicated structures and finally consider 3-dimensional cycloidal antiferromagnets. Detailed theoretical techniques used to describe magnons in such unusual spin structures are also presented. The dynamics of local spins can be well described within classical electrodynamics. Therefore, we restrict ourselves here to the classical treatment.

2.1 Underlying equations

The equation of motion of magnetization in continuous media is described by the Landau-Lifshitz equation [32]:

$$\frac{\partial \mathbf{M}}{\partial t} = \gamma \mathbf{H}_{eff} \times \mathbf{M}.$$

This equation has a clear physical meaning: magnetization is proportional to the spin density which represents an angular momentum. The equation of motion is now the Newton's second law: the change of angular momentum on the left side equals the net torque on the right side. The torque tries to align the magnetization along the effective field but this leads to the precession of the moment around its equilibrium direction. In order to account for dissipation an additional term is usually added to the right side. This damping term can be written in different forms which significantly differ only for large dampings. In Landau-Lifshitz form [32] the equation of motion becomes:

$$\frac{\partial \mathbf{M}}{\partial t} = \gamma \left(\mathbf{H}_{eff} \times \mathbf{M} - \lambda \frac{\mathbf{M} \times (\mathbf{M} \times \mathbf{H}_{eff})}{M^2} \right),$$

where $\gamma = g|e|/(2mc)$ - gyromagnetic ratio, λ - damping parameter and \mathbf{H}_{eff} - effective magnetic field acting upon an element of the sample with a local magnetization \mathbf{M} . The effective field is determined by the variational derivative of free energy by the magnetization \mathbf{M} :

$$\mathbf{H}_{eff} = -\frac{\delta F}{\delta \mathbf{M}}.$$

For the scope of this work it is sufficient to consider quasi-classical approximation when the spins are considered as vectors with a fixed length (Heisenberg spins). In this case the magnetization can be written as $\mathbf{M} = -g\mu_B \mathbf{S} = -g|e|\hbar/(2mc)\mathbf{S}$. At temperatures well below magnetic ordering the free energy F approaches internal energy E which is the quasiclassical Hamiltonian H . The equation of motion for the j -th spin \mathbf{S}_j becomes then:

$$\frac{\partial \mathbf{S}_j}{\partial t} = \frac{g|e|}{2mc} \mathbf{H}_{eff,j} \times \mathbf{S}_j + \frac{\lambda \mathbf{S}_j \times (\mathbf{S}_j \times \mathbf{H}_{eff,j})}{\hbar S^2}; \quad \frac{g|e|\hbar}{2mc} \mathbf{H}_{eff,j} = \frac{\delta H}{\delta \mathbf{S}_j}. \quad (2.1)$$

The ac magnetic field \mathbf{h} of incident radiation is introduced directly into the effective magnetic field \mathbf{H}_{eff} . In this case the linear equation (2.1) could be solved giving dependency $\mathbf{M}(\omega, \mathbf{q}, \mathbf{h})$. The tensor of dynamic magnetic susceptibility $\hat{\chi}$ is now directly obtained from the definition $\mathbf{M} = \hat{\chi} \mathbf{h}$. However in most cases only the dispersion relation of the magnons $\omega(k)$ together with the picture of the spins' motion are of interest. In these cases both the exciting magnetic field and dissipation term can be omitted and the equation (2.1) is solved as the eigenvalue and eigenvector problem. The eigenvalues give the dispersion relation and the corresponding eigenvectors - the associated motion of the spins.

2.2 Ferromagnets

In ferromagnetic materials all spins tend to align along the same direction. Ferromagnets are the simplest magnetically ordered materials to consider and they are treated here to introduce the basic techniques used for theoretical description of magnons.

The simplest model of dielectric ferromagnet is obtained by assuming that the exchange interaction between adjacent spins is negative. The corresponding 1D Hamiltonian reads:

$$H = -J \sum_j (\mathbf{S}_j \cdot \mathbf{S}_{j+1}). \quad (2.2)$$

In the ground state all spins are aligned along the same direction $\mathbf{S}_j = \mathbf{S}_0$ and the ground energy is $E = -JNS^2$. In the following the systems with further terms like anisotropy will be considered building upon the basic ferromagnet described by Hamiltonian (2.2).

2.2.1 Ferromagnet with easy axis anisotropy in magnetic field

Firstly, a ferromagnet with easy axis anisotropy and in external magnetic field along the same axis will be considered. It is described by the following Hamiltonian:

$$\begin{aligned} H &= -J \sum_j (\mathbf{S}_j \cdot \mathbf{S}_{j+1}) - K \sum_j (\mathbf{S}_j^{(z)})^2 - \sum_j (\mathbf{H} \cdot \mathbf{M}_j) = \\ &= -J \sum_j (\mathbf{S}_j \cdot \mathbf{S}_{j+1}) - K \sum_j (\mathbf{n}_z \cdot \mathbf{S}_j)^2 + \frac{g|e|\hbar}{2mc} \sum_j (\mathbf{H} \cdot \mathbf{S}_j). \end{aligned}$$

The anisotropic term $-K(\mathbf{n}_z \cdot \mathbf{S}_j)^2$ makes the z direction energetically favourable and in the ground state all spins are aligned along the easy axis: $\mathbf{S}_j = S_0 \mathbf{n}_z$. Here \mathbf{n}_z - the unit vector in the positive direction of the z axis. The term $-(\mathbf{H} \cdot \mathbf{M}_j)$ is just the Zeeman energy of magnetic moments in external magnetic field.

The first step in determining the magnon dispersion is to find the variation of Hamiltonian with respect to the j -th spin. In this case

$$\begin{aligned} \delta H &= -J \delta \mathbf{S}_j \cdot (\mathbf{S}_{j-1} + \mathbf{S}_{j+1}) - 2K(\mathbf{n}_z \cdot \mathbf{S}_j)(\mathbf{n}_z \cdot \delta \mathbf{S}_j) + \frac{g|e|\hbar}{2mc} (\mathbf{H} \cdot \delta \mathbf{S}_j) = \\ &= \delta \mathbf{S}_j \cdot \left(-J(\mathbf{S}_{j-1} + \mathbf{S}_{j+1}) - 2K(\mathbf{n}_z \cdot \mathbf{S}_j)\mathbf{n}_z + \frac{g|e|\hbar}{2mc} \mathbf{H} \right). \end{aligned}$$

The effective magnetic field acting upon j -th spin is then:

$$\frac{g|e|\hbar}{2mc} \mathbf{H}_{eff,j} = \frac{\delta H}{\delta \mathbf{S}_j} = -J(\mathbf{S}_{j-1} + \mathbf{S}_{j+1}) - 2K(\mathbf{n}_z \cdot \mathbf{S}_j)\mathbf{n}_z + \frac{g|e|\hbar}{2mc} \mathbf{H}.$$

As expected, the effective field $\mathbf{H}_{eff,j}$ contains the unmodified external field \mathbf{H} . The anisotropy acts in the same way as the magnetic field trying to align the spins along the easy axis. The first term in the effective field represents the coupling of adjacent spins; the j -th spin tends to point toward the direction averaged across two neighbouring spins.

The effective field $\mathbf{H}_{eff,j}$ should be substituted into equation (2.1). We search for a solution in form of a plane wave:

$$\mathbf{S}_j = \mathbf{S}_0 + \mathbf{A}e^{i(qaj-\omega t)}. \quad (2.3)$$

The amplitude \mathbf{A} of the wave is assumed to be much smaller than the equilibrium spin \mathbf{S}_0 . Thus, the terms quadratic in \mathbf{A} can be omitted from the equation (2.1). From the condition of a constant length of each spin \mathbf{S}_j the vector amplitude \mathbf{A} within the same accuracy should be orthogonal to \mathbf{S}_0 : $\mathbf{A} \cdot \mathbf{S}_0 = 0$ ($A_z = 0$).

The substitution yields:

$$\begin{aligned} \frac{\partial}{\partial t} (\mathbf{S}_0 + \mathbf{A}e^{i(qaj-\omega t)}) = & \left(-\frac{J}{\hbar} (2\mathbf{S}_0 + \mathbf{A}e^{i(qa(j+1)-\omega t)} + \mathbf{A}e^{i(qa(j-1)-\omega t)}) - \right. \\ & \left. -\frac{2K}{\hbar} (\mathbf{n}_z \cdot \mathbf{S}_0)\mathbf{n}_z + \frac{g|e|}{2mc}\mathbf{H} \right) \times (\mathbf{S}_0 + \mathbf{A}e^{i(qaj-\omega t)}). \end{aligned}$$

The dissipation term λ is assumed to be zero and will be discussed separately. Omitting quadratically small terms and reducing by the common factor $e^{i(qaj-\omega t)}$, we get:

$$\begin{aligned} -i\omega\mathbf{A} = & \frac{J}{\hbar} (\mathbf{S}_0 \times \mathbf{A}) (e^{iqa} + e^{-iqa} - 2) - \frac{2KS}{\hbar} (\mathbf{n}_z \times \mathbf{A}) + \frac{g|e|}{2mc} (\mathbf{H} \times \mathbf{A}); \\ i\omega\mathbf{A} = & \left(\frac{2JS}{\hbar} (1 - \cos(qa)) + \frac{2KS}{\hbar} + \frac{g|e|H}{2mc} \right) (\mathbf{n}_z \times \mathbf{A}). \end{aligned}$$

The last vector equation is actually a system of two linear equations in variables A_x and A_y :

$$\begin{cases} i\omega A_x + \left(\frac{2JS}{\hbar} (1 - \cos(qa)) + \frac{2KS}{\hbar} + \frac{g|e|H}{2mc} \right) A_y = 0 \\ -\left(\frac{2JS}{\hbar} (1 - \cos(qa)) + \frac{2KS}{\hbar} + \frac{g|e|H}{2mc} \right) A_x + i\omega A_y = 0 \end{cases}. \quad (2.4)$$

The condition for the existence of nonzero solutions of the system (2.4) is the eigenvalue problem for coefficient matrix and non-trivial solutions are the eigenvectors of this matrix. The determinant directly gives the dispersion relation:

$$\begin{aligned} -\omega^2 + \left(\frac{2JS}{\hbar} (1 - \cos(qa)) + \frac{2KS}{\hbar} + \frac{g|e|H}{2mc} \right)^2 &= 0; \\ \omega = \frac{2JS}{\hbar} (1 - \cos(qa)) + \frac{2KS}{\hbar} + \frac{g|e|H}{2mc}. \end{aligned}$$

It is convenient, especially for further considerations, to introduce the following parameters:

$$\omega_0 = \frac{2JS}{\hbar}; \quad \kappa = \frac{K}{J}; \quad h = \frac{g|e|H\hbar}{2mc2JS}. \quad (2.5)$$

The dispersion relation can be written then as:

$$\omega/\omega_0 = 1 - \cos(qa) + \kappa + h.$$

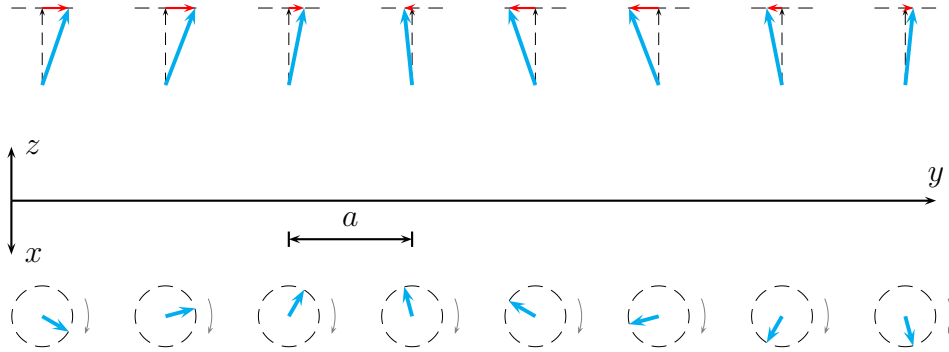


Figure 2.1: Schematic representation of a spin wave in a typical ferromagnet. The black dashed arrows represent the ground state, the cyan thick arrows - orientations of spins in a wave and red arrows are the deviations of spins from their equilibrium orientations. Upper panel is a front view, lower panel is the top view. The spins in the top view are rotating along circular orbits (black dashed circles) in the clockwise direction (pointed by gray arrows).

Substituting the found expression for ω back into the system (2.4) the polarization of the spin wave is easily found:

$$A_x = iA_y. \quad (2.6)$$

Thus, the result well known from many textbooks on magnetism is obtained: the spin waves in a simple ferromagnet have a quadratic dispersion in the long wavelength limit and exhibit a gap if either easy axis anisotropy or external magnetic field are present (see, for example, Fig 2.2). The spins precess around their equilibrium directions with the spins moving along circular orbits, as shown in Fig. 2.1.

2.2.2 The treatment of the exciting field and dissipation

Examination of the interaction of spins with the exciting magnetic field of incident radiation allows to establish the connection between microscopic quantities describing spin subsystem and the optical parameters measurable in experiments like magnetic susceptibility $\hat{\chi}$. As was shown above, for magnons the easy axis anisotropy acts in the same way as an external static magnetic field. Therefore it is assumed zero for simplicity ($K = 0$). The magnetic field of the incident radiation has the form of a plane wave. However, on the scale of magnons the wave vector of light can be assumed to be zero with a good accuracy, $\mathbf{q} = 0$. The magnetic field can be written then as $\mathbf{h}e^{-i\omega t}$. The effective magnetic field acting upon j -th spin becomes:

$$\frac{g|e|\hbar}{2mc}\mathbf{H}_{eff,j} = -J(\mathbf{S}_{j-1} + \mathbf{S}_{j+1}) + \frac{g|e|\hbar}{2mc}\mathbf{H} + \frac{g|e|\hbar}{2mc}\mathbf{h}e^{-i\omega t}.$$

The amplitude \mathbf{A} of the spin wave is now assumed to be not only much smaller than the equilibrium spin \mathbf{S}_0 but also of the same order as the exciting field \mathbf{h} . Thus, the

terms containing product $\mathbf{h} \cdot \mathbf{A}$ can be also omitted from the equation (2.1). It is easy to see that the effective field $\mathbf{H}_{eff,j}$ enters the equation (2.1) only as a vector product $\mathbf{H}_{eff,j} \times \mathbf{S}_j$. After omitting quadratically small terms the exciting field \mathbf{h} appears in the equation of motion only as $\mathbf{h} \times \mathbf{S}_0$. Therefore the component of \mathbf{h} along the equilibrium direction \mathbf{S}_0 does not play any role and will be assumed to be zero, so that $\mathbf{h} \perp \mathbf{S}_0$. The additional term in the equation of motion due to the excitation field is:

$$\frac{g|e|}{2mc} \mathbf{h} \times \mathbf{S}_0.$$

The dissipative term can be transformed as:

$$\frac{\lambda}{\hbar} \frac{\mathbf{S}_j \times (\mathbf{S}_j \times \mathbf{H}_{eff,j})}{S^2} = \frac{\lambda}{\hbar} \left(\mathbf{S}_j \frac{(\mathbf{S}_j \cdot \mathbf{H}_{eff,j})}{S^2} - \mathbf{H}_{eff,j} \right)$$

and after substituting the effective field, the plane wave of the form (2.3), and omitting quadratically small terms we get:

$$\frac{\lambda}{\hbar} \left(\mathbf{S}_j \frac{(\mathbf{S}_j \cdot \mathbf{H}_{eff,j})}{S^2} - \mathbf{H}_{eff,j} \right) = -\frac{H}{\hbar S} \lambda \mathbf{A} e^{-i\omega t} - \frac{\lambda}{\hbar} \mathbf{h} e^{-i\omega t}.$$

To simplify the subsequent expressions, the dimensionless damping coefficient α_d and resonant frequency in the absence of damping $\tilde{\omega}_0$ are introduced as follows:

$$\lambda = \alpha_d |M| = \alpha_d \hbar S \frac{g|e|}{2mc}; \quad \tilde{\omega}_0 = \frac{g|e|H}{2mc}.$$

Substituting these definitions into equation of motion (2.1) the following system of coupled equations is obtained:

$$\begin{cases} (-i\omega + \tilde{\omega}_0 \alpha_d) A_x - \tilde{\omega}_0 A_y = \frac{g|e|S}{2mc} (h_y - \alpha_d h_x) \\ \tilde{\omega}_0 A_x + (-i\omega + \tilde{\omega}_0 \alpha_d) A_y = \frac{g|e|S}{2mc} (-h_x - \alpha_d h_y) \end{cases}.$$

After solving this system, the amplitude $\mathbf{A} = (A_x, A_y)$ is obtained as a linear function of incident magnetic field $\mathbf{h} = (h_x, h_y)$ (both $A_z = 0$ and $h_z = 0$):

$$\mathbf{A} = \frac{\frac{g|e|S}{2mc}}{\tilde{\omega}_0^2(1 + \alpha_d^2) - \omega^2 - 2i\omega\tilde{\omega}_0\alpha_d} \begin{pmatrix} -\tilde{\omega}_0(1 + \alpha_d^2) + i\alpha_d\omega & -i\omega \\ i\omega & -\tilde{\omega}_0(1 + \alpha_d^2) + i\alpha_d\omega \end{pmatrix} \mathbf{h}.$$

The dynamic magnetization of a ferromagnet $\mathbf{m} = (m_x, m_y)$ can be now obtained as $\mathbf{m} = -ng|e|\hbar/(2mc)\mathbf{A} = \hat{\chi}\mathbf{h}$, where n is a volume density of spins. In the case when absorption is not very large, $\alpha_d^2 \ll 1$, this yields a well-known expression [33] for dynamic susceptibility tensor of a ferromagnet:

$$\hat{\chi} = \frac{\Delta\chi\tilde{\omega}_0^2}{\tilde{\omega}_0^2 - \omega^2 - 2i\omega\tilde{\omega}_0\alpha_d} \begin{pmatrix} 1 - i\alpha_d\omega/\tilde{\omega}_0 & i\omega/\tilde{\omega}_0 \\ -i\omega/\tilde{\omega}_0 & 1 - i\alpha_d\omega/\tilde{\omega}_0 \end{pmatrix}.$$

Thus, the components of magnetic susceptibility have a Lorentz-like form featuring a resonance at $\omega = \tilde{\omega}_0$ with the amplitude $\Delta\chi$. Introducing the saturation magnetization $M_s = nSg|e|\hbar/(2mc)$ the amplitude can be written as:

$$\Delta\chi = \left(\frac{g|e|}{2mc}\right)^2 \frac{\hbar S n}{\tilde{\omega}_0} = \frac{g|e|}{2mc} \frac{M_s}{\tilde{\omega}_0} = \frac{M_s}{H}.$$

One notable consequence of this result is the violation of the Lyddane-Sachs-Teller relation, valid for permittivity. It basically says that $\Delta\varepsilon \sim 1/\tilde{\omega}_0^2$ whereas for permeability, as shown above, $\Delta\mu \sim 1/\tilde{\omega}_0$.

2.2.3 Ferromagnet with next-nearest-neighbour interaction

As the last example the ferromagnet with next-nearest-neighbour interaction will be considered. In the case when this interaction is antiferromagnetic a quite interesting crossover to noncollinear spin order can occur. Already such a simple model resembles the behaviour observed in rare earth manganites. The Hamiltonian of the system reads:

$$H = -J \sum_j (\mathbf{S}_j \cdot \mathbf{S}_{j+1}) + J_{nnn} \sum_j (\mathbf{S}_j \cdot \mathbf{S}_{j+2}).$$

First, the ground state of the system should be found which is the arrangement of spins with the lowest possible energy. For the cycloidal or spiral spin arrangement the angle between any two adjacent spins is α and between any two next-nearest-neighbour spins is 2α . The energy of such spin order is

$$E = -JNS^2 (\cos(\alpha) - j_{nnn} \cos(2\alpha)),$$

where

$$j_{nnn} = \frac{J_{nnn}}{J} \quad (2.7)$$

is dimensionless next-nearest-neighbour interaction. The condition of the minimum of the energy with respect to α is then:

$$\sin(\alpha) (1 - 4j_{nnn} \cos(\alpha)) = 0. \quad (2.8)$$

This yields either $\sin(\alpha) = 0$ which is a collinear ferromagnetic state or $4j_{nnn} \cos(\alpha) = 1$ which has solutions only for $j_{nnn} > 1/4$. It can easily be shown that the noncollinear state is energetically favourable provided the last condition is satisfied, so the ferromagnetic order is stable only for $j_{nnn} < 1/4$.

The vector equation of motion of the spins in the ferromagnetic state is:

$$\omega \mathbf{A} = \frac{2JS}{\hbar} \left(1 - \cos(qa) - \frac{J_{nnn}}{J} (1 - \cos(2qa)) \right) (\mathbf{n}_z \times \mathbf{A}),$$

with the dispersion relation

$$\omega/\omega_0 = 1 - \cos(qa) - j_{nnn} (1 - \cos(2qa))$$

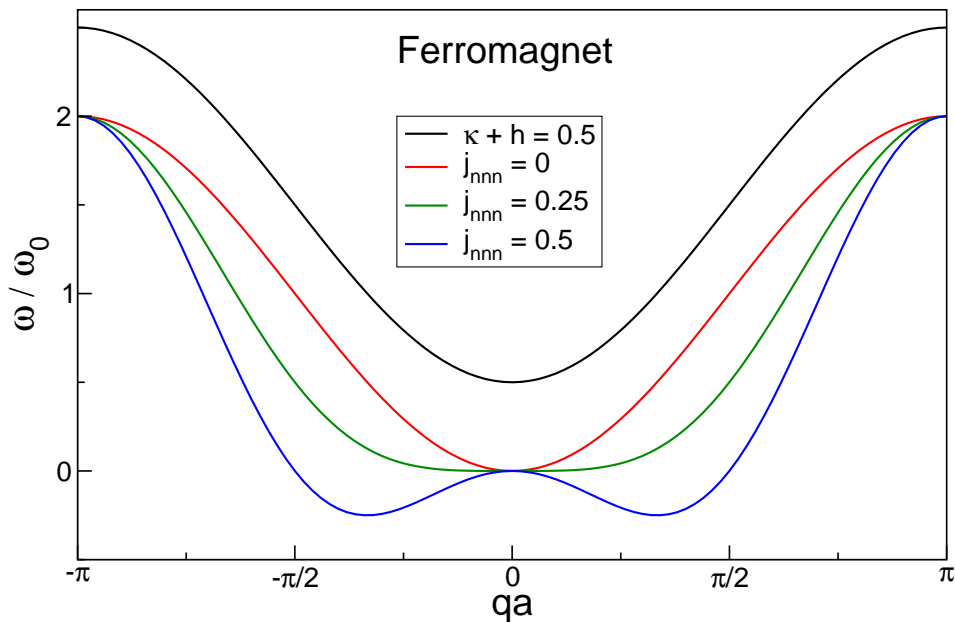


Figure 2.2: Magnon dispersions in ferromagnets with different additional terms in Hamiltonian: with easy axis anisotropy and in external magnetic field (black line), without any additional terms (red line), with antiferromagnetic next-nearest-neighbour interaction at the critical value (green line) and above critical value (blue line). The last curve has no physical meaning; the minima with negative energy indicate that the ferromagnetic state is unstable against transition into the new cycloidal or spiral ground state.

and the same polarization of the spin wave (2.6) as in a simple ferromagnet.

The condition of the minimum in the dispersion curve coincides exactly with (2.8) if the substitution $qa = \alpha$ is made. Therefore, the dispersion relation shows minima with negative energy for $j_{nnn} > 1/4$ (see Fig. 2.2). Such solutions have no physical meaning but they show that the system is unstable and another ground state should be first found. The magnons in a 3D cycloidal antiferromagnet are studied in details below and this short example is just illustrating that the properties of excitations in a system reflect also the stability of the ground state.

2.3 Ferrimagnets

Ferrimagnets are materials with more than one type of spins possibly aligned antiparallel but still showing nonzero spontaneous magnetization. In this sense they form an intermediate class between ferromagnets and antiferromagnets. Ferrimagnets are taken into consideration here as a typical example to derive the properties of magnons using standard solid state techniques with a unit cell containing two spins. The characteristics of the magnons in an antiferromagnet could be then obtained as a limiting case of a ferrimagnet. On the other hand, antiferromagnets will be treated further below in the framework of the so-called co-rotating frame formalism. This technique is crucial for the consideration of the incommensurate cycloidal antiferromagnets but is much less

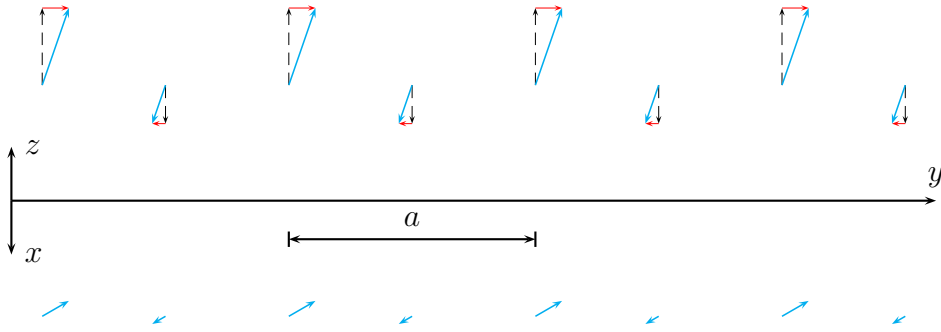


Figure 2.3: Schematic representation of a spin wave in a ferrimagnet for the lower frequency branch at $qa \rightarrow 0$ and $\Omega \rightarrow 0$. The black dashed arrows represent the ground state, the cyan thicker arrows - orientations of spins in a wave and red arrows are the deviations of spins from their equilibrium orientations. Upper panel is a front view, lower panel - top view. For this particular mode, the spins can change their orientation in arbitrary direction.

widespread. Therefore, the comparison of results obtained by both methods for simple antiferromagnets will provide the validation for this novel technique.

One of the simplest models of a ferrimagnet with antiferromagnetic coupling is described by the following one-dimensional Hamiltonian:

$$H = J \sum_j \left(\mathbf{S}_j^{(1)} \cdot \mathbf{S}_j^{(2)} + \mathbf{S}_j^{(2)} \cdot \mathbf{S}_{j+1}^{(1)} \right).$$

Here, two types of spins with different lengths S_1 and S_2 exist. The exchange constant is assumed to be the same along the spin chain (see also Fig. 2.3). As there are two nonequivalent spins in a magnetic unit cell now, two different equations of motion of the form (2.1) should be written, each with a separate effective field acting upon the spins of its own kind. For the model Hamiltonian given above these fields are:

$$\frac{g|e|\hbar}{2mc} \mathbf{H}_{eff,j}^{(1)} = J \left(\mathbf{S}_{j-1}^{(2)} + \mathbf{S}_j^{(2)} \right); \quad \frac{g|e|\hbar}{2mc} \mathbf{H}_{eff,j}^{(2)} = J \left(\mathbf{S}_j^{(1)} + \mathbf{S}_{j+1}^{(1)} \right).$$

The solution can be again obtained in the form of a plane wave, but with different vector amplitudes corresponding to spins of different length:

$$\mathbf{S}_j^{(1)} = \mathbf{S}_0^{(1)} + \mathbf{A} e^{i(qaj - \omega t)}; \quad \mathbf{S}_j^{(2)} = \mathbf{S}_0^{(2)} + \mathbf{B} e^{i(qaj - \omega t)}.$$

Here, the ground state values of spins are assumed to be $\mathbf{S}_0^{(1)} \uparrow \uparrow \mathbf{n}_z$, $\mathbf{S}_0^{(2)} \uparrow \downarrow \mathbf{n}_z$, $\mathbf{A} \perp \mathbf{n}_z$ and $\mathbf{B} \perp \mathbf{n}_z$ (see Fig. 2.3).

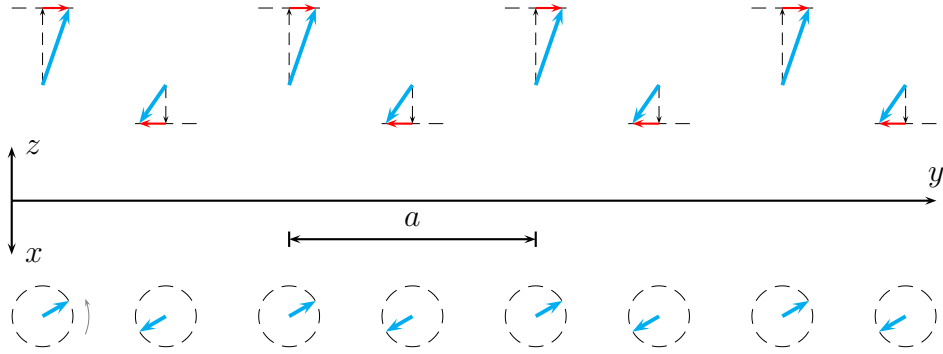


Figure 2.4: Schematic representation of a spin wave in a ferrimagnet for the higher frequency branch at $qa = 0$ and $\Omega = S_2 - S_1$. The black dashed arrows represent the ground state, the cyan thick arrows - orientations of spins in a wave and red arrows are the deviations of spins from their equilibrium orientations. Upper panel is a front view, lower panel - top view. The spins in the top view are rotating in the counterclockwise direction (gray arrow).

The two vector equations of motion for each sort of spins are:

$$\begin{cases} i\omega \mathbf{A} = \frac{J}{\hbar} (2S_2(\mathbf{n}_z \times \mathbf{A}) + S_1(\mathbf{n}_z \times \mathbf{B}) (1 + e^{-iqa})) \\ -i\omega \mathbf{B} = \frac{J}{\hbar} (2S_1(\mathbf{n}_z \times \mathbf{B}) + S_2(\mathbf{n}_z \times \mathbf{A}) (1 + e^{iqa})) \end{cases}$$

They are equivalent to the following system of four equations with four variables A_x , A_y , B_x and B_y , where the notation $\Omega = \hbar\omega/(2J)$ is used:

$$\begin{cases} i\Omega A_x + S_2 A_y + S_1 \frac{1 + e^{-iqa}}{2} B_y = 0 \\ -S_2 A_x + i\Omega A_y - S_1 \frac{1 + e^{-iqa}}{2} B_x = 0 \\ -S_2 \frac{1 + e^{iqa}}{2} A_y + i\Omega B_x - S_1 B_y = 0 \\ S_2 \frac{1 + e^{iqa}}{2} A_x + S_1 B_x + i\Omega B_y = 0 \end{cases} \quad (2.9)$$

Expanding the determinant of this system the following characteristic equation is obtained:

$$\Omega^4 - (S_1^2 + S_2^2 - S_1 S_2 (1 + \cos(qa))) \Omega^2 + \left(\frac{S_1 S_2}{2} (1 - \cos(qa)) \right)^2 = 0.$$

The solutions of this equation are two branches of magnon dispersion in the model ferrimagnet:

$$2\Omega_{1,2} = \sqrt{S_1^2 + S_2^2 - 2S_1 S_2 \cos(qa)} \pm (S_1 - S_2). \quad (2.10)$$

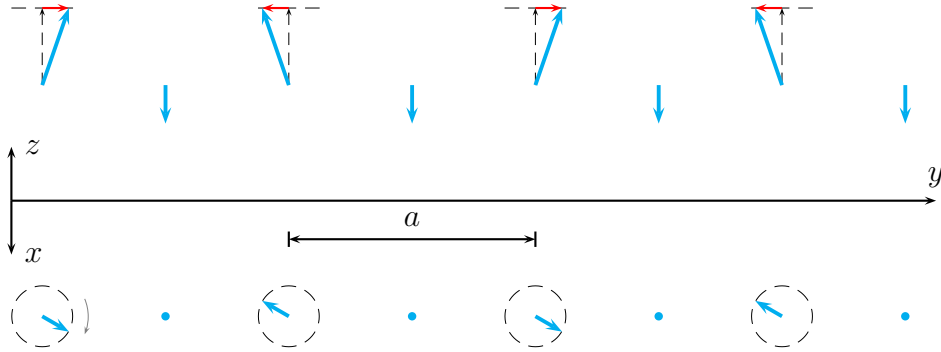


Figure 2.5: Schematic representation of a spin wave in a ferrimagnet for the lower frequency branch at $qa = \pi$ and $\Omega = S_2$. The black dashed arrows represent the ground state, the cyan thick arrows - orientations of spins in a wave and red arrows are the deviations of spins from their equilibrium orientations. Upper panel is a front view, lower panel - top view. The smaller spins do not move at all while the bigger spins rotate in the top view in the clockwise direction shown by the gray arrow.

Figure 2.7 illustrates them for a few representative ratios S_2/S_1 .

Substituting the obtained dispersion relations into the system (2.9) the polarization of spin waves can be found. It has a somewhat complicated character, two limiting cases, $qa = 0$ and $qa = \pi$, will be discussed below:

$qa = 0, \Omega = 0$ The only constraint which the system (2.9) imposes is $S_2\mathbf{A} + S_1\mathbf{B} = 0$ - the deviation of a spin is proportional to the length of spin in the ground state. This zero frequency mode has a meaning of changing the ground state orientation of spins in an arbitrary direction (see Fig. 2.3). The mode also has a nonvanishing magnetization in the direction of the bigger spin and therefore can interact with external magnetic field.

$qa = 0, \Omega = \mathbf{S}_1 - \mathbf{S}_2$ In this long wavelength spin wave the deviations of spins of different kind are the same: $\mathbf{A} + \mathbf{B} = 0$, and the spins are moving along circular orbits: $A_y = \iota A_x$ (see Fig. 2.4). Contrary to the previous mode the dynamic components of the magnetic moments are compensated across the unit cell and there is no magnetization associated with this mode.

$qa = \pi, \Omega = \mathbf{S}_2$ In the lower frequency short wavelength spin mode the smaller spins do not participate at all: $\mathbf{B} = 0$, and the bigger spins are moving like in the ferromagnet: $A_x = \iota A_y$ (Fig. 2.5).

$qa = \pi, \Omega = \mathbf{S}_1$ On the other hand, the spin mode where the bigger spins are fixed, $\mathbf{A} = 0$, and only smaller spins are moving, $B_y = \iota B_x$, is a higher frequency mode (Fig. 2.6).

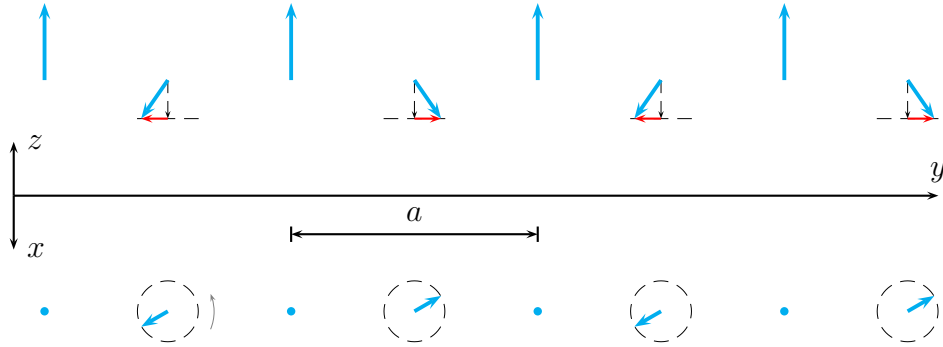


Figure 2.6: Schematic representation of a spin wave in a ferrimagnet for the higher frequency branch at $qa = \pi$ and $\Omega = S_1$. The black dashed arrows represent the ground state, the cyan thick arrows - orientations of spins in a wave and red arrows are the deviations of spins from their equilibrium orientations. Upper panel is a front view, lower panel - top view. In this mode, the bigger spins are still while the smaller spins rotate in the top view in the counterclockwise direction shown by the gray arrow.

A simple antiferromagnet can be obtained assuming $S_2 = S_1 = S$. In this case the two ferrimagnetic branches (2.10) become degenerate and simplified to a well-known expression [34]:

$$\frac{\omega}{\omega_0} = \left| \sin \left(\frac{qa}{2} \right) \right|, \quad (2.11)$$

where definition (2.5) is used for ω_0 . At $qa = \pi$ any linear combination of these two modes is also allowed in an antiferromagnet. We should take this into account when considering the results for a simple antiferromagnet.

2.4 Simple collinear antiferromagnet

Antiferromagnetic materials possess magnetic order but with fully compensated magnetic moments, so the net magnetization is zero. There are a lot of ways to realize antiferromagnetic state, especially in three dimensional crystals. The incommensurate cycloidal order relevant for the low temperature phases of some rare earth manganites is a rather complicated possibility and requires for its treatment extended theoretical tools. Here, the simplest one dimensional collinear antiferromagnet will be considered in the framework of so-called co-rotating frame formalism in order to introduce this technique. Without substantial complications the model antiferromagnet can be assumed being anisotropic with hard, medium and easy magnetic axes, respectively:

$$H = J \sum_j (\mathbf{S}_j \cdot \mathbf{S}_{j+1}) + K_x \sum_j (\mathbf{n}_x \cdot \mathbf{S}_j)^2 + K_y \sum_j (\mathbf{n}_y \cdot \mathbf{S}_j)^2.$$

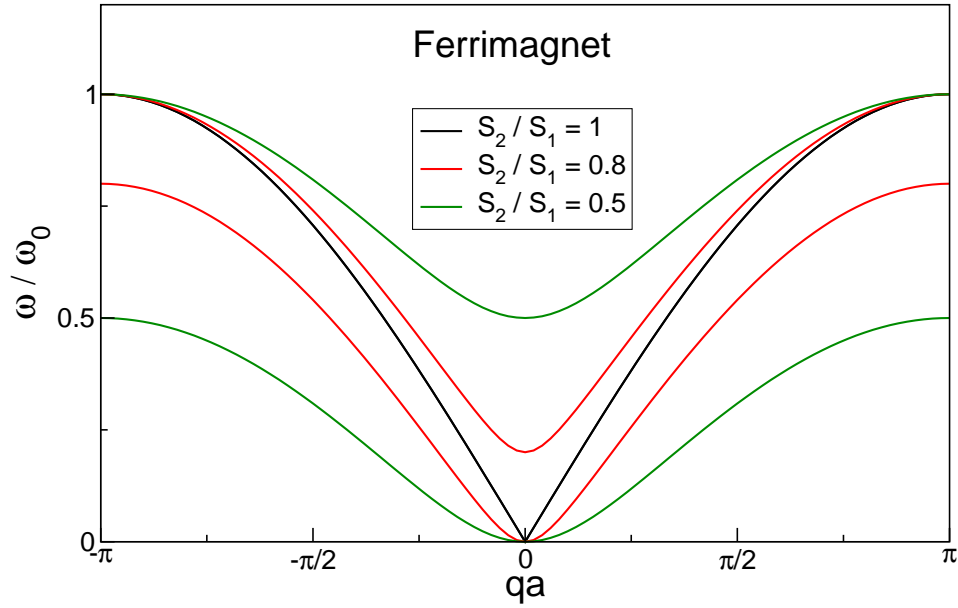


Figure 2.7: Two branches of magnon dispersion in a ferrimagnet with different spin ratios S_2/S_1 . The black curves corresponds to the case of a pure antiferromagnet where two magnon branches are degenerate. The green curves are plotted for the same spin ratio as used in schematic drawings 2.3 - 2.6.

The spins in the ground state are aligned along the easy z axis but with alternating direction, which can be schematically denoted as “up-down-up-down-...” order (see also Fig. 2.8). The key idea here is to introduce such a reference frame which gets rotated by 180 degrees around the x axis when moving from one spin in a chain to the next. In such reference frame the central spin points always “up”. Moreover, all other spins also have the fixed direction independently upon which spin is chosen as “central” one: the nearest neighbours are antiparallel with the central spin, the next nearest neighbours are parallel and so on. In some sense, the alternating antiferromagnetic order in real space is transformed into the uniform ferromagnetic order in the co-rotating space. As the Hamiltonian of this system is uniform from the beginning, this eliminates the need to include two spins in a unit cell which can be viewed as a simplification in the case of collinear antiferromagnet. It should be noted that the “rotations” in the description above should not be interpreted literally; they are applied to spins only and do not change the orientation of crystallographic axes, for example.

In order to proceed with a formal considerations it is convenient to introduce the operator \hat{R}_α of rotation around the x axis by the angle α . In the component matrix notation it is:

$$\hat{R}_\alpha = \begin{pmatrix} 1 & 0 & 0 \\ 0 & \cos(\alpha) & \sin(\alpha) \\ 0 & -\sin(\alpha) & \cos(\alpha) \end{pmatrix}. \quad (2.12)$$

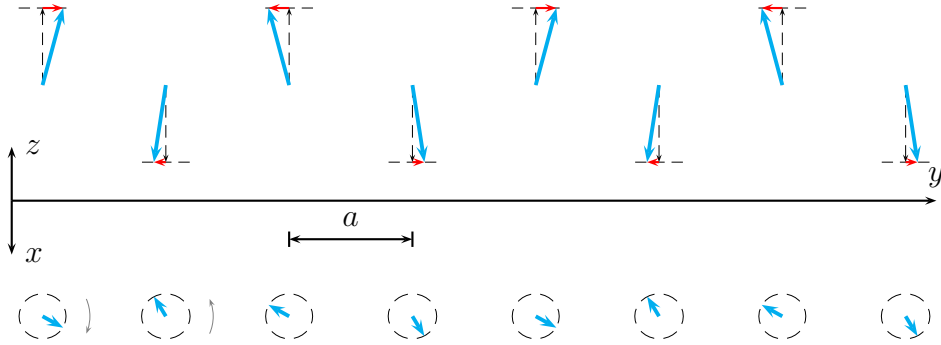


Figure 2.8: Schematic representation of a spin wave at $qa = \pi/2$ in the anisotropic antiferromagnet. The black dashed arrows represent the ground state, the cyan thick arrows - orientations of spins in a wave and red arrows are the deviations of spins from their equilibrium orientations. Upper panel is a front view, lower panel - top view. The spins in the top view are rotating along almost circular orbits (black dashed ellipses) in the alternating directions (pointed by the gray arrows).

For example, if $\alpha = \pi$:

$$\hat{R}_\pi = \begin{pmatrix} 1 & 0 & 0 \\ 0 & -1 & 0 \\ 0 & 0 & -1 \end{pmatrix}.$$

Of course, the rotations around the same axis are commutative and additive: $\hat{R}_\alpha \hat{R}_\beta = \hat{R}_\beta \hat{R}_\alpha = \hat{R}_{\alpha+\beta}$. Therefore, we may write $(\hat{R}_\beta)^j = \hat{R}_{j\beta}$. The antiferromagnetic ground state can be written now as $\mathbf{S}_j = \hat{R}_{j\pi} \mathbf{S}_0$, where $\mathbf{S}_0 \parallel \mathbf{n}_z$.

The last key element in the current approach is to consider not only the ground state in the co-rotating frame but the amplitude of a spin wave as well:

$$\mathbf{S}_j = \hat{R}_{j\pi} (\mathbf{S}_0 + \mathbf{A} e^{i(qaj - \omega t)}) = \begin{pmatrix} 0 \\ 0 \\ (-1)^j S \end{pmatrix} + \begin{pmatrix} A_x \\ (-1)^j A_y \\ 0 \end{pmatrix} e^{i(qaj - \omega t)}. \quad (2.13)$$

As the new approach first appears only when the solution of the vector equation of motion is searched for in particular form (2.13), all previous steps like calculating effective magnetic field stay intact. One complication with this approach is that the rotation operator does not commute with the operations of vector or scalar products. This means that the vector equation of motion should be expanded into components and therefore the component form is included in (2.13).

Performing aforementioned substitutions and after simplifications and using definitions (2.5) the following system which describes spin waves in a collinear antiferromagnet

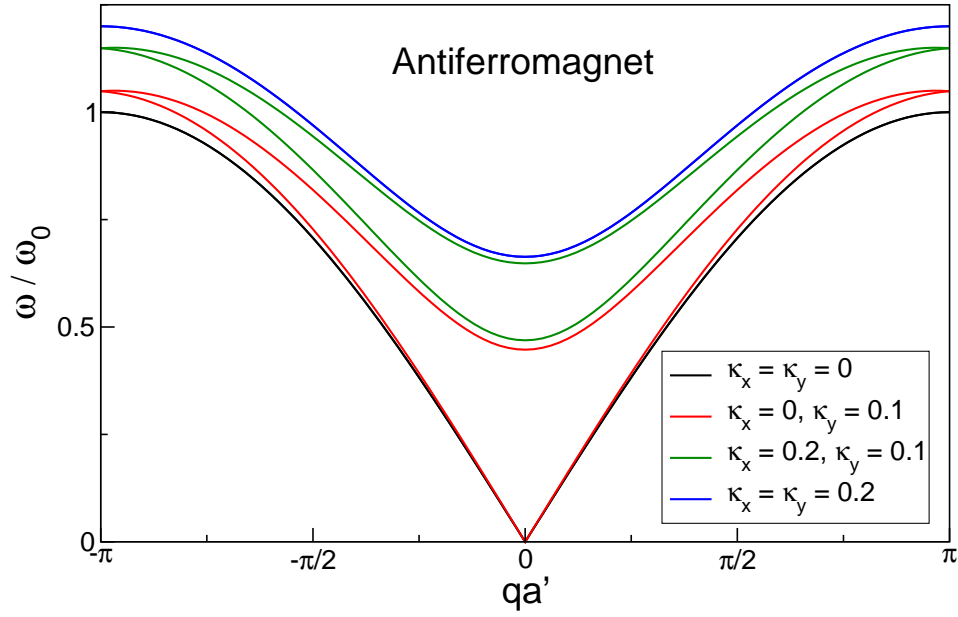


Figure 2.9: Two branches of magnon dispersion in different antiferromagnets. The black line corresponds to the case of a fully isotropic antiferromagnet where two magnon branches are degenerate. An antiferromagnet with easy plane anisotropy is represented by the red curves, while degenerate branches in an antiferromagnet with easy axis anisotropy are shown by the blue line. The green curves represent a fully anisotropic antiferromagnet and are plotted for the same parameters as used in Figures 2.8, 2.10 and 2.11.

is obtained:

$$\begin{cases} i\frac{\omega}{\omega_0}A_x + (1 + \kappa_y - \cos(qa))A_y = 0 \\ -(1 + \kappa_x + \cos(qa))A_x + i\frac{\omega}{\omega_0}A_y = 0 \end{cases}. \quad (2.14)$$

The magnon dispersion is then easily derived:

$$\omega/\omega_0 = \sqrt{(1 + \kappa_x + \cos(qa))(1 + \kappa_y - \cos(qa))}. \quad (2.15)$$

It is important to note that parameter a here is a distance between adjacent spins and not the size of the magnetic unit cell which is $a' = 2a$ (see Fig. 2.11). It is therefore possible to say that in the co-rotating frame formalism the “reduced” unit cell and “extended” Brillouin zone (with $-\pi < qa < \pi$) are considered. In order to compare the current results with the predictions made for ferrimagnets the substitution $a \rightarrow a'/2$ should be made. The dispersion relation is then defined across two Brillouin zones, $-2\pi < qa' < 2\pi$ and should be folded back into the first Brillouin zone to obtain the second magnon branch. Performing this procedure and assuming the antiferromagnet isotropic, $\kappa_x = \kappa_y = 0$, exactly the expression (2.11) comes out. The folded magnon dispersion for some representative values of anisotropy are shown in Fig. 2.9

The polarization, which is another important property of spin waves, is given in the

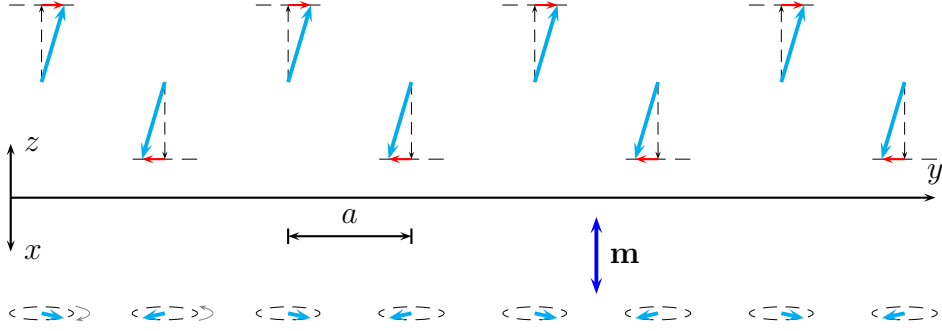


Figure 2.10: Schematic representation of a magnon at $qa = 0$ in an anisotropic antiferromagnet. The black dashed arrows represent the ground state, the cyan thick arrows - orientations of spins in a wave and red arrows are the deviations of spins from their equilibrium orientations. Upper panel is a front view, lower panel - top view. The spins in the top view are rotating along elliptical orbits (black dashed ellipses) in the alternating directions (pointed by the gray arrows). This magnon possesses nonvanishing dynamic magnetization along the x axis shown by the thick blue arrow.

co-rotating frame by:

$$\sqrt{1 + \kappa_x + \cos(qa)}A_x = \nu\sqrt{1 + \kappa_y - \cos(qa)}A_y. \quad (2.16)$$

In order to obtain polarization in the laboratory reference frame, spin rotation (2.13) should be applied. All schematic drawings 2.8, 2.10 and 2.11 have been plotted taking this fact into account.

Figure 2.8 schematically shows the spin wave in a fully anisotropic antiferromagnet for $qa = \pi/2$. This is a magnon at the boundary of the magnetic Brillouin zone in Fig. 2.9. The magnon at $qa = -\pi/2$ has the same motion of spins except that the deviation of each second spin should be reversed. As the frequencies of these two magnons are exactly the same (green curves at $qa' = \pi$ in Fig. 2.9), any linear combination of them is also allowed. It is easy to see now that the sum of these two spin waves gives the magnon shown in Fig. 2.5 while their difference is the magnon in Fig. 2.6.

The magnons at the center of the magnetic Brillouin zone are more interesting as the magnetization does not vanish after averaging the spin deviations across the whole crystal. These magnons can therefore interact with the magnetic component of radiation and can be seen as absorption peaks in the optical spectroscopy.

The magnon schematically shown in Fig. 2.10 corresponds to $qa = 0$ in the co-rotating frame. The main motion of spins occurs in the y direction and the properties of the antiferromagnet along this direction (anisotropy $\kappa_y \neq 0$ in this case) determine both the frequency of the magnon and the magnitude of the small deviations in the x direction (see dispersion relation (2.15) and polarization (2.16)). However, it is this small component of spins along the x direction that is responsible for the magnetic moment associated with

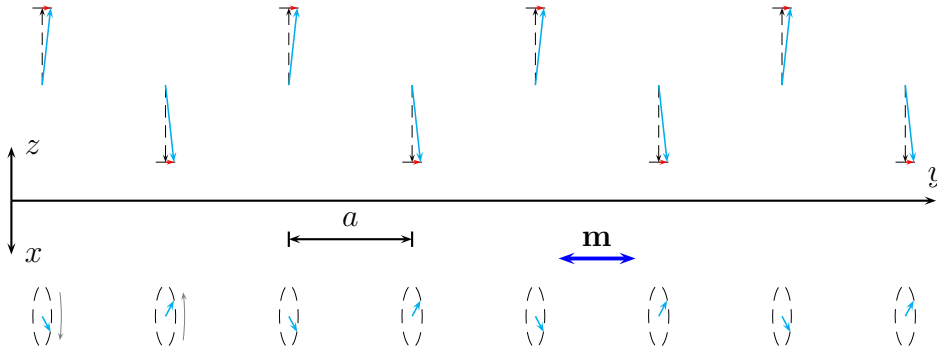


Figure 2.11: Schematic representation of a magnon at $qa = \pi$ in the anisotropic antiferromagnet. The black dashed arrows represent the ground state, the cyan thicker arrows - orientations of spins in a wave and red arrows are the deviations of spins from their equilibrium orientations. Upper panel is a front view, lower panel - top view. The spins in the top view are rotating along elliptical orbits (black dashed ellipses) in the alternating directions (pointed by the gray arrows). This spin wave has nonzero dynamic magnetization along the y axis shown by the thick blue arrow.

this magnon. The bigger component along the y direction is fully compensated already inside the magnetic unit cell. The magnon at $qa = \pi$ shown in Fig. 2.11 is very similar but with the main motion of spins along the x direction and magnetic moment along the y direction. It is interesting to trace, how the wave with $qa = \pi \neq 0$ in the co-rotating frame is still able to produce a magnetic moment with $q = 0$. The key component here is the static antiferromagnetic order which can be considered as a frozen standing spin wave with $qa = \pi$. As the spin waves are small deviations superimposed with the static order, they are “interacting” with the static standing wave in some sense and can get shifted in the \mathbf{q} -space by the wave vector \mathbf{Q} of the static order. The details of this process differ in each case and are contained in the expression (2.13). Namely, the x component is left intact while the y component always gets shifted. This property of spin waves is also responsible for the difference between magnon branches even in the degenerate cases. Although the frequencies of two branches can coincide for all wave vectors, they still have different polarizations which can be accessed in experiments like polarized neutron scattering or polarization analysis in optical spectroscopy. For example, two magnon branches for a fully isotropic antiferromagnet (black curve in Fig. 2.9) are degenerate. However, the magnon at $qa = 0$ on one branch has spin deviations along the x direction, while the magnon on the other branch - along the y direction. Note, that the linear combination of these two magnons correspond to the zero frequency spin wave shown in Fig. 2.3.

Selective shifting of wave vector depending on polarization makes dispersion representation in Figure 2.9 not entirely correct. The problem can be well seen in Fig. 2.11 for example. Although the y components of spins point in the same direction and have

the wave vector $qa' = 0$ as shown in Fig. 2.9, the x components point in alternating directions and have $qa' = 2\pi$ (or $qa = \pi$). Therefore, the x and y components of the same magnon come from different Brillouin zones. In other words, the first and the second Brillouin zones are not equivalent. If the spin wave dispersion is measured with some polarization sensitive technique, one magnon branch in the first Brillouin zone would turn into the other branch in the next Brillouin zone and vice versa. The inequivalence of Brillouin zones is not very significant in the case of simple antiferromagnet considered here. However, in the case of incommensurate antiferromagnet the absence of magnetic Brillouin zone and shifting of wave vectors lead to quite unusual magnon dispersion.

2.5 Cycloidal incommensurate antiferromagnet

The low temperature magnetic order in multiferroic manganites like TbMnO_3 , DyMnO_3 , $\text{Eu}_x\text{Y}_{1-x}\text{MnO}_3$ in the doping range $0.2 < x \leq 0.5$ and, depending on the cooling history, also in GdMnO_3 appears to be incommensurate cycloidal with the spins lying either in bc or ab planes. This has been proved using neutron diffraction at least for TbMnO_3 [35]. For the first time, the spiral and cycloidal magnetic orderings were proposed simultaneously in connection with different materials in the late 1950s (see, for example, Ref. [36]). Shortly afterwards, the magnon spectra were calculated using co-rotating frame technique [37]. The first theoretical model describing ground state ordering in orthorhombic manganites appeared almost at the same time as the the discovery of induced ferroelectricity [21]. Already at that time it was stressed out that the competition between ferromagnetic nearest-neighbour and antiferromagnetic next-nearest-neighbour interactions in MnO_2 planes plays the main role for the establishment of frustrated magnetic order.

The important step towards description of excitations in multiferroic manganites was the work [38] where the mixed spin-phonon Hamiltonian was considered. The authors have also used the co-rotating frame technique and made a number of predictions regarding electro- and magneto-active modes in optical spectroscopy and the positions of peaks in the inelastic neutron scattering spectra. However the limited information included in this paper and the large number of topics covered have made it rather hard for inexperienced reader to comprehend the model proposed. The simpler model considering the magnetic subsystem only was published later [39] and contains possibly the most detailed and closest description of the model that will be presented below. The spin-phonon interaction in the form suggested in [38] will be considered indirectly later by introducing the Dzyaloshinskii-Moriya term as a small perturbation.

2.5.1 The unit cell and Brillouin zone

Contrary to one dimensional models above, the spatial coordinates of nearest and next-nearest neighbours play an important role in three dimensional antiferromagnets. Figure 2.12 schematically shows the positions of manganese atoms which are assumed the only magnetic ions in the model. Different exchange paths taken into account in Hamilto-

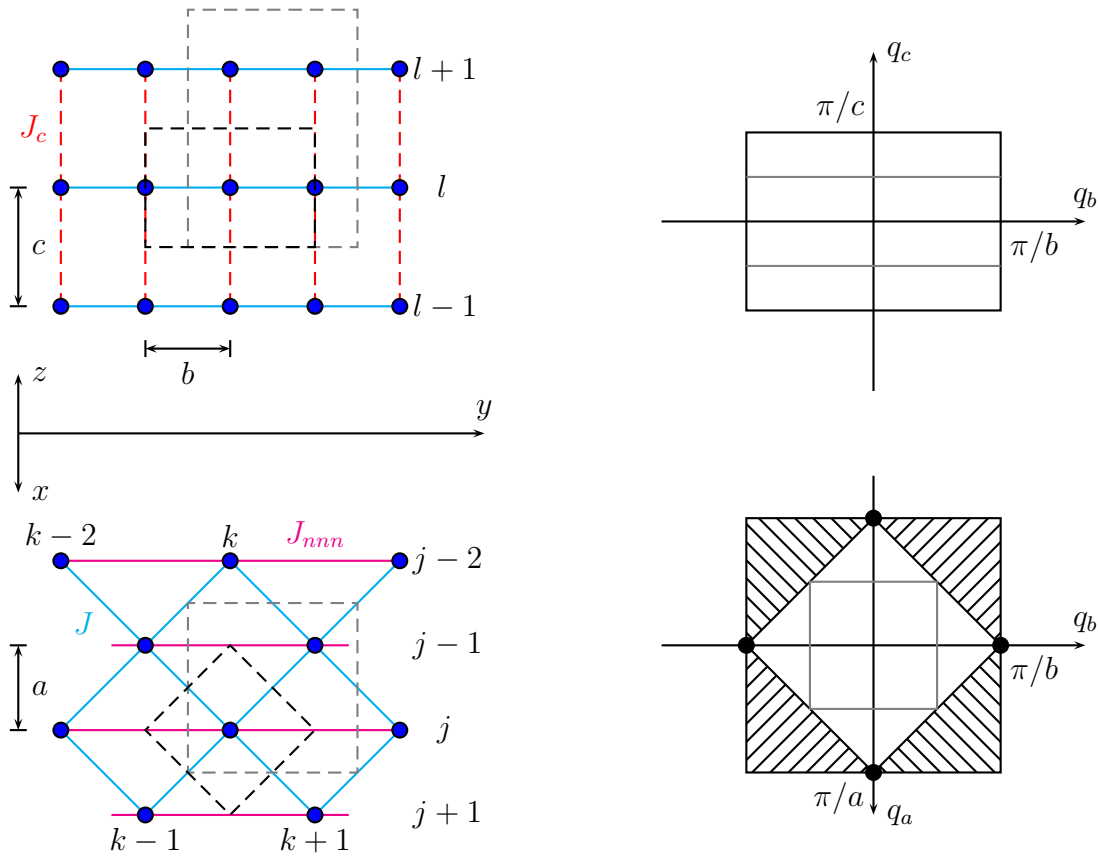


Figure 2.12: Schematic representation of the orthorhombic (gray dashed rectangle) and cubic (black dashed rectangle) unit cells used in the Heisenberg model of cycloidal antiferromagnet (left side). Upper panels are front views, lower panels - top views. Only manganese atoms (blue circles) relevant for the magnetism are shown. The lines represent different exchange interactions: the nearest-neighbour ferromagnetic interaction J (cyan lines), the next-nearest-neighbour antiferromagnetic interaction J_{nnn} (magenta lines) and interlayer antiferromagnetic interaction J_c (red dashed lines). The coordinate system, the indexing scheme and definitions of lattice parameters a , b and c used in the text are also shown. The corresponding orthorhombic (gray rectangles) and cubic (black rectangles) Brillouin zones are presented in the right side. The hatched triangles are also formally accessible in the dispersion relation but represent physically redundant areas and should be discarded (see text for the details).

nian below are also shown. After cooperative Jahn-Teller distortions the crystallographic unit cell becomes orthorhombic and contains four Mn spins (gray dashed rectangles in the left side of Fig. 2.12). However, using co-rotating frame technique, it is possible to consider fewer different spins in the reduced cell. Indeed, the antiferromagnetic interlayer order can be easily treated with the unit cell halved along the $z \parallel c$ direction, as was shown above. Moreover, the incommensurate cycloidal order within MnO_2 planes makes it impossible to introduce a magnetic unit cell at all. The obvious choice of a reduced cell with only one spin would be the cubic unit cell. The drawback of such a choice is that the propagation vector of spin cycloid is oriented along the diagonal of the cubic cell (see Fig. 2.12) which would make the spin modulation wave vector multicomponent in the cubic coordinates. Therefore, the indexing is still done along orthorhombic principal

axes (see Fig. 2.12) but with the halved spacing along both x and y axes. Note that the cell spanned across the associated spacing parameters a , b and c is not a unit cell even for undistorted cubic structure: the in-plane translations would produce twice as much Mn sites as actually present. However, it is easy to account for this fact: the site with indices (j, k) is occupied if and only if the indices j and k have the same parity (both are even or both are odd). For example, assuming that initial indices j and k are both zero, the site (j, k) in Fig. 2.12 is occupied. The sites $(j, k \pm 2)$ and $(j \pm 2, k)$ are also occupied, but not the sites $(j, k \pm 1)$ or $(j \pm 1, k)$. Thus, it is actually the counting scheme of the atoms on a square lattice rotated by 45 degrees to the coordinate system.

The choice of the too small reduced cell automatically implies that the associated Brillouin zone, shown in the right side of Fig. 2.12 would be too large. The solution is also quite simple: in this case it is necessary to discard the hatched triangles in the Fig. 2.12 and the remaining diamond-shaped area is again the Brillouin zone of the cubic unit cell.

It should be noted that the seemingly excessive complications with the choice of the reduced cell are common in the community. The careful consideration of works [40, 41], for example, shows that the authors use the orthorhombic unit cell parameters $a' = 2a$ and $b' = 2b$, at least in the MnO_2 planes. However the dispersion relations are plotted up to the values $q_b < 2\pi/b'$, crossing the boundary of the second orthorhombic Brillouin zone, which is equivalent to $q_b < \pi/b$, staying inside the first cubic Brillouin zone, used in the present variant.

Another notation for the wave vectors is common inside the neutron scattering community. The wave vectors are expressed in the units of the translation vectors in the reciprocal space [42]. For example, the wave vector $(0, 1, 0)$ in crystallographic units corresponds to the vector $(0, \frac{2\pi}{b'}, 0)$ in the physical units which equals to $(0, \frac{\pi}{b}, 0)$ in the present notation. The wave vector of the static spin cycloid $(0, 0.28, 0)$ [43] transforms then in the same way into the physical vector $(0, \frac{0.28\pi}{b}, 0)$.

2.5.2 Cycloidal antiferromagnet with easy plane anisotropy

The basic model which is able to reproduce the ground state of frustrated rare earth perovskites but still can be treated analytically is described by the following Hamiltonian:

$$H = \sum_l \sum_j \sum_{k=j, j\pm 2, \dots} \left(-J(\mathbf{S}_{j,k,l} \cdot \mathbf{S}_{j-1, k+1, l}) - J(\mathbf{S}_{j,k,l} \cdot \mathbf{S}_{j+1, k+1, l}) + \right. \quad (2.17)$$

$$\left. + J_{nnn}(\mathbf{S}_{j,k,l} \cdot \mathbf{S}_{j, k+2, l}) + J_c(\mathbf{S}_{j,k,l} \cdot \mathbf{S}_{j, k, l+1}) + K(\mathbf{n}_x \cdot \mathbf{S}_{j,k,l})^2 \right).$$

The first two terms represent the ferromagnetic superexchange between two nearest Mn spins via oxygen orbitals (cyan lines in the left side of Fig. 2.12). The third term is an antiferromagnetic exchange between next-nearest manganese atoms along the y direction via two oxygen atoms (magenta lines in Fig. 2.12). The fourth term describes the antiferromagnetic coupling along the z direction between MnO_2 layers (red dashed lines). The last single ion anisotropy term makes yz an easy plane to fix the direction

of possible spin cycloid as observed experimentally. Without the anisotropy both spin cycloids in the yz and xy planes and also the proper screw spin arrangement along the y axis would be all degenerate. It is easy to see that the form of (2.17) together with special summation rules discussed above account for each exchange path exactly once (see also Fig. 2.12 for the indexing scheme).

Like in the case of a simple antiferromagnet, the rotation operator (2.12) is applied to the fixed spin vectors to obtain both the ground state and the spin waves. This operator describes both, the antiferromagnetic ordering along the z direction, and cycloidal order along the y direction. As both of them can be obtained via rotations around the x axis the presence of two different magnetic orders along different axes does not lead to significant complications:

$$\begin{aligned} \mathbf{S}_{j,k,l} &= \hat{R}_{k\alpha+l\pi} (\mathbf{S}_0 + \mathbf{A}e^{i(\mathbf{q}\mathbf{r}-\omega t)}) = \hat{R}_{k\alpha+l\pi} (\mathbf{S}_0 + \mathbf{A}e^{i(q_a a j + q_b b k + q_c c l - \omega t)}) = \\ &= (-1)^l S \begin{pmatrix} 0 \\ \sin(k\alpha) \\ \cos(k\alpha) \end{pmatrix} + \begin{pmatrix} A_x \\ (-1)^l \cos(k\alpha) A_y \\ -(-1)^l \sin(k\alpha) A_y \end{pmatrix} e^{i(q_a a j + q_b b k + q_c c l - \omega t)}. \end{aligned} \quad (2.18)$$

The spins form the cycloid along the y direction with the angle α between two nearest neighbours.

In order to find the ground state of the system, dynamic part will be assumed zero, $\mathbf{A} = 0$ and the expression (2.18) substituted into Hamiltonian (2.17). The energy of such spin configuration is then:

$$E = -JNS^2(2 \cos(\alpha) - j_{nnn} \cos(2\alpha) + j_c),$$

where definitions (2.7) and

$$j_c = \frac{J_c}{J} \quad (2.19)$$

are used. Minimizing the ground state energy the following equation is obtained:

$$\sin(\alpha)(1 - 2j_{nnn} \cos(\alpha)) = 0.$$

The noticeable difference from the similar equation (2.8) for one dimensional spin chain is a smaller factor outside j_{nnn} . This reflects different number of nearest and next-nearest neighbours in one and three dimensional models: in one dimensional chain each spin has two nearest and two next-nearest neighbours while in the three dimensional model each spin interact with four in-plane nearest neighbors and only two next-nearest spins along the y direction.

The trivial solution $\alpha = 0$ corresponds to A -type antiferromagnetic ordering typical for rare earth manganites on the left hand side compared to Gd in the phase diagram 1.11. It is again easy to show that the non-trivial solution $\cos(\alpha) = 1/(2j_{nnn})$ corresponding to (generally) incommensurate cycloidal order has the lowest energy in the whole range of its existence. Therefore, the transition from A -type to cycloidal spin order occurs at the critical value $j_{nnn} = 1/2$ within the current model. Equation $\cos(\alpha) = 1/(2j_{nnn})$ has generally two solutions: with positive and negative angle α . These two solutions

correspond to the spin cycloids rotating in the opposite directions and they can be obtained one from the other by the spatial inversion. As will be shown below, the direction of spin rotation in the cycloid characterizes the direction of spontaneous electric polarization in the ferroelectric domain.

Consideration of dynamic properties of the cycloidal antiferromagnet starts with the calculation of the effective magnetic field $\mathbf{H}_{eff,j,k,l}$ acting upon spin $\mathbf{S}_{j,k,l}$. In present case it has more terms as in the previous sections due to larger number of adjacent interacting neighbours:

$$\begin{aligned} \frac{g|e|\hbar}{2mc}\mathbf{H}_{eff,j,k,l} = & -J(\mathbf{S}_{j-1,k+1,l} + \mathbf{S}_{j+1,k+1,l} + \mathbf{S}_{j-1,k-1,l} + \mathbf{S}_{j+1,k-1,l}) + \\ & + J_{nnn}(\mathbf{S}_{j,k+2,l} + \mathbf{S}_{j,k-2,l}) + J_c(\mathbf{S}_{j,k,l+1} + \mathbf{S}_{j,k,l-1}) + 2K(\mathbf{n}_x \cdot \mathbf{S}_{j,k,l})\mathbf{n}_x \end{aligned}$$

Substituting the effective magnetic field into equation of motion (2.1) the spin waves are searched for in the form (2.18). After simple but rather lengthy calculations in the component form it is possible to obtain the following system of equations:

$$\begin{cases} i\frac{\omega}{\omega_0}A_x + P(\mathbf{q})A_y = 0 \\ -Q(\mathbf{q})A_x + i\frac{\omega}{\omega_0}A_y = 0 \end{cases} \quad (2.20)$$

The dispersion relation of magnons in a cycloidal antiferromagnet is now easily found:

$$\frac{\omega}{\omega_0} = \sqrt{P(\mathbf{q})Q(\mathbf{q})}, \quad (2.21)$$

together with the polarization of spin waves:

$$\sqrt{Q(\mathbf{q})}A_x = i\sqrt{P(\mathbf{q})}A_y. \quad (2.22)$$

Here $P(\mathbf{q})$ and $Q(\mathbf{q})$ are defined as following:

$$\begin{aligned} P(\mathbf{q}) &= 2\cos(\alpha)(1 - \cos(q_a a)\cos(q_b b)) + j_{nnn}\cos(2\alpha)(\cos(2q_b b) - 1) + j_c(1 - \cos(q_c c)); \\ Q(\mathbf{q}) &= \kappa + 2\cos(\alpha) - 2\cos(q_a a)\cos(q_b b) + j_{nnn}(\cos(2q_b b) - \cos(2\alpha)) + j_c(1 + \cos(q_c c)), \end{aligned}$$

where definitions (2.5), (2.7) and (2.19) for ω_0 , j_{nnn} , j_c and κ are used. The expressions $P(\mathbf{q})$ and $Q(\mathbf{q})$ in the form above can be used to determine the properties of magnons in both A -type and cycloidally ordered phases by substituting the appropriate values of α . As the magnetically induced ferroelectricity and electromagnons appear only in frustrated cycloidal phase, only cycloidal state will be considered further. After substitutions $\cos(\alpha) = 1/(2j_{nnn})$ and $\cos(2\alpha) = 1/(2j_{nnn}^2) - 1$ the expressions $P(\mathbf{q})$ and $Q(\mathbf{q})$ are simplified to:

$$\begin{aligned} P(\mathbf{q}) &= 2j_{nnn}\sin^2(q_b b) - \frac{\cos(q_b b)}{j_{nnn}}(\cos(q_a a) - \cos(q_b b)) + j_c(1 - \cos(q_c c)); \\ Q(\mathbf{q}) &= \kappa + \frac{1}{2j_{nnn}} - 2\cos(q_a a)\cos(q_b b) + j_{nnn}(1 + \cos(2q_b b)) + j_c(1 + \cos(q_c c)). \end{aligned}$$

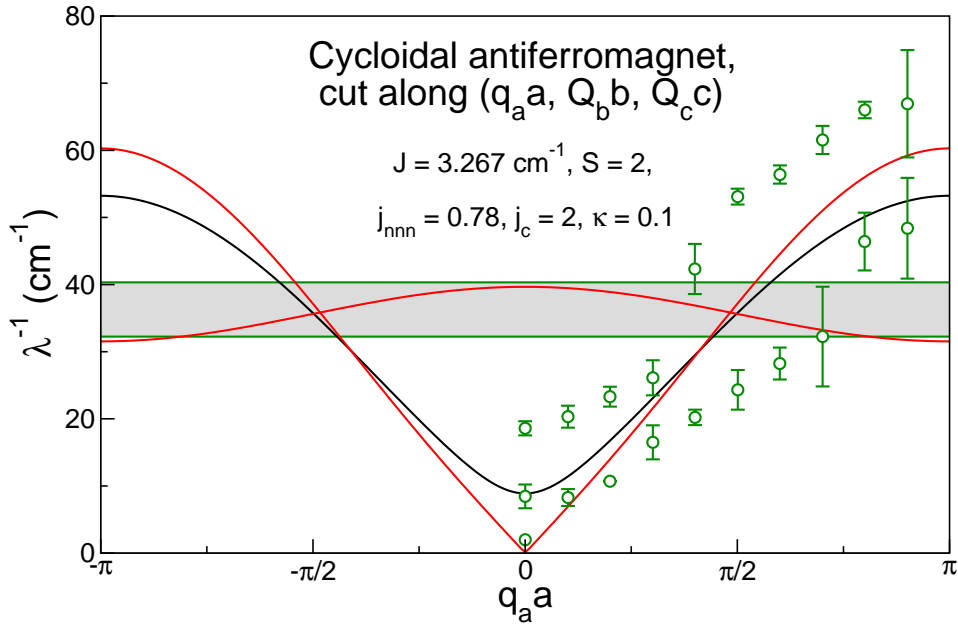


Figure 2.13: Magnon dispersion in a cycloidal antiferromagnet for a direction parallel to the x axis and passing through the static modulation wave vector \mathbf{Q} . The black line is the unshifted dispersion of magnetic moments polarized along the x axis while the red lines correspond to shifted dispersions of two modes polarized in yz plane. The model parameters used are taken from Ref. [39]. Green circles with error bars are experimental data from Ref. [44] measured by inelastic neutron scattering. The gray band around $30 - 40 \text{ cm}^{-1}$ was interpreted by the authors of [44] as a crystal field excitation of Tb^{3+} ions, but could be well fitted by a magnon branch as well.

As in the case of simple collinear antiferromagnet, the rotations (2.18) should be applied to both the dispersion (2.21) and polarization (2.22). This rotation leads to the shifting of wave vectors by the static modulation vector which can be best seen from the static order:

$$\hat{\mathbf{R}}_{k\alpha+l\pi} \mathbf{S}_0 = (-1)^l S \begin{pmatrix} 0 \\ \sin(k\alpha) \\ \cos(k\alpha) \end{pmatrix} = \frac{S}{2} \begin{pmatrix} 0 \\ -i \\ 1 \end{pmatrix} e^{i\mathbf{Q}\mathbf{r}} + \frac{S}{2} \begin{pmatrix} 0 \\ i \\ 1 \end{pmatrix} e^{-i\mathbf{Q}\mathbf{r}}, \quad (2.23)$$

where $\mathbf{Q} = (0, \frac{\alpha}{b}, \frac{\pi}{c})$. The alternative expression above was obtained using complex relations $\cos(k\alpha) = (e^{ik\alpha} + e^{-ik\alpha})/2$, $\sin(k\alpha) = (e^{ik\alpha} - e^{-ik\alpha})/(2i)$ and $(-1)^l = e^{i\pi l} = e^{-i\pi l}$. Thus, the static magnetic order in cycloidal phase consists of two waves with opposite wave vectors. The polarizations of these waves are not equal and would correspond to the left and right circularly polarized waves if they had nonzero frequency. Exchanging the amplitudes of static waves is equivalent to the change $\alpha \rightarrow -\alpha$ and represent the spin cycloid rotating in the opposite direction. Such cycloid also satisfies the solution $\cos(\alpha) = 1/(2j_{nnn})$ and corresponds to another possible domain in the sample.

From the structure of the static order it could be expected that the dynamic wave vector in the co-rotating frame would be shifted by both static vectors in the laboratory

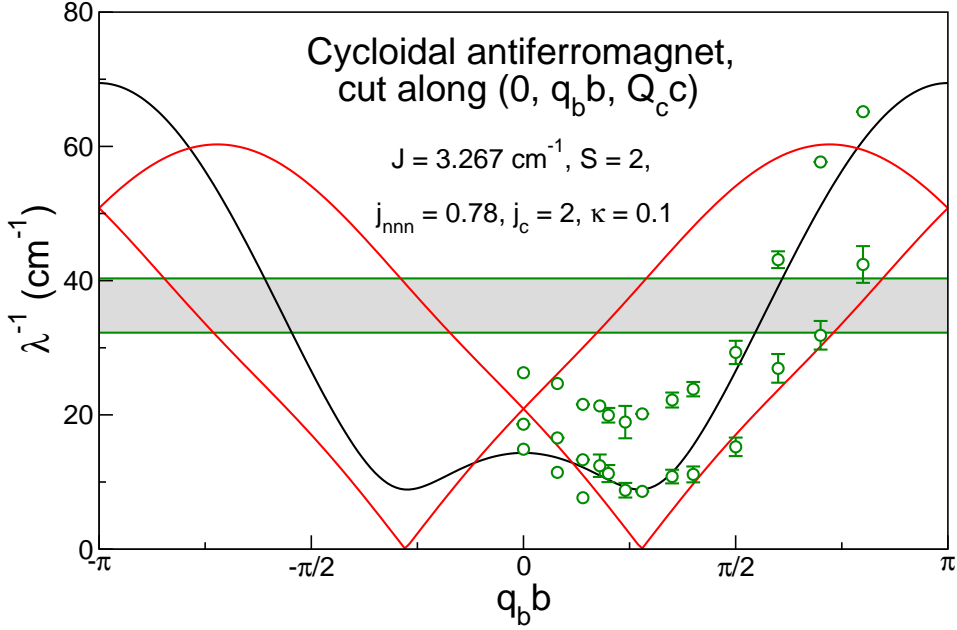


Figure 2.14: Magnon dispersion in a cycloidal antiferromagnet for a direction parallel to the y axis and passing through the static modulation wave vector \mathbf{Q} . The notations of solid lines and parameters used are the same as in the Fig. 2.13. The neutron scattering data shown as green circles together with the gray absorption band are taken from Ref. [44].

frame. Indeed, the dynamic part of (2.18) can be transformed to:

$$\hat{\mathbf{R}}_{k\alpha+l\pi} \mathbf{A} e^{i\mathbf{q}\mathbf{r}} = A_x \begin{pmatrix} 1 \\ 0 \\ 0 \end{pmatrix} e^{i\mathbf{q}\mathbf{r}} + \frac{A_y}{2} \begin{pmatrix} 0 \\ 1 \\ i \end{pmatrix} e^{i(\mathbf{q}+\mathbf{Q})\mathbf{r}} + \frac{A_y}{2} \begin{pmatrix} 0 \\ 1 \\ -i \end{pmatrix} e^{i(\mathbf{q}-\mathbf{Q})\mathbf{r}}. \quad (2.24)$$

The magnon in a cycloidal antiferromagnet consists of three components: the one component is linearly polarized along the x axis with the unchanged wave vector \mathbf{q} and two components with wave vectors $\mathbf{q} + \mathbf{Q}$ and $\mathbf{q} - \mathbf{Q}$ polarized circularly in the yz plane. The sum of two circular polarizations does not yield linear polarization because circular components have different wave vectors. As the static modulation vector \mathbf{Q} is incommensurate with the lattice parameter b , the wave vector shifting can not be represented by the reduced magnetic Brillouin zone and should be done directly.

2.5.3 Inelastic neutron scattering spectra

One of the best methods to obtain the properties of magnetic subsystem is the neutron diffraction. The cycloidal spin order in TbMnO_3 was established by analyzing elastic neutron Bragg reflections [35]. On the other hand, the access to magnon dispersion at arbitrary wave vectors is enabled via inelastic neutron scattering experiments which will be briefly discussed below.

Figures 2.13 - 2.15 show the predicted dispersion curves of magnons in a cycloidal antiferromagnet along different directions. The black line in each figure shows the un-

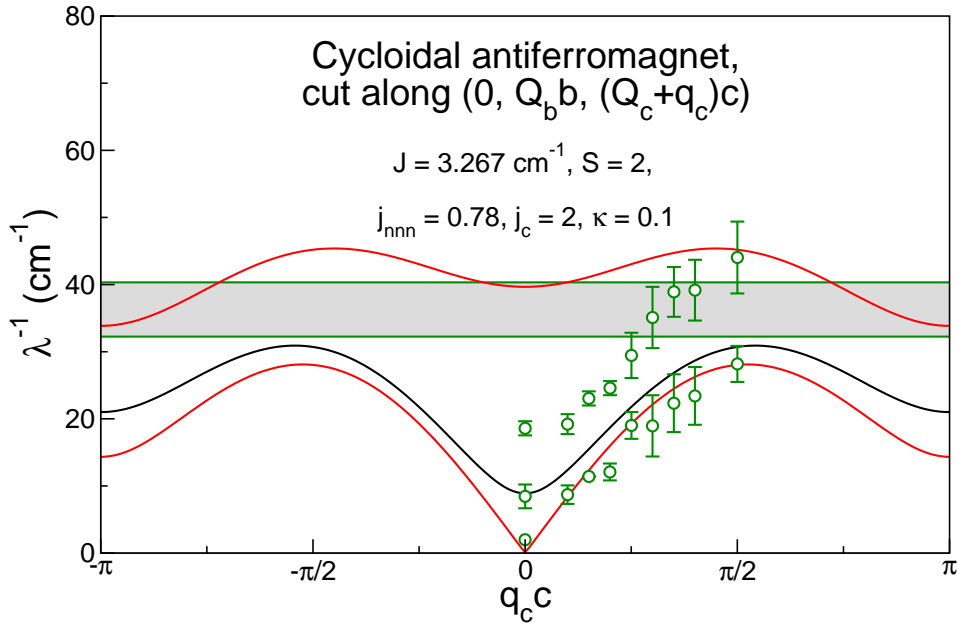


Figure 2.15: Magnon dispersion in a cycloidal antiferromagnet for a direction parallel to the z axis and passing through the static modulation wave vector \mathbf{Q} . The notations of solid lines and parameters used are the same as in the Fig. 2.13. The neutron scattering data shown as green circles together with the gray absorption band are taken from Ref. [44]. The band around $30 - 40 \text{ cm}^{-1}$ was interpreted as a crystal field excitation of Tb^{3+} ions, but could be also attributed to a magnon branch as well.

shifted dispersion of the x components of spins while two red lines represent the two possible polarizations of spin components in the yz plane. The cuts of a Brillouin zone were chosen to coincide with the neutron scattering experiments [44]. The data reported there are reproduced as green circles with error bars and provide a valuable test of the present model. The parameters of the model are taken from Ref. [39]. The authors of Ref. [39] also used neutron scattering data [44] to estimate exchange constants but have not provided any fits of the experimental spectra.

Overall, the model fits the data rather well on the qualitative basis and can be even said to fit the data semi-quantitatively. The most noticeable disagreement is the absence of the highest energy magnon branch in Fig. 2.14 in experimental data. The careful reading of Ref. [44] shows that the region of the reciprocal space where this branch is expected was not accessible in the scattering geometry which could explain this discrepancy. The model also predicts the existence of weakly dispersive branches close to 40 cm^{-1} in the wave vector scans along x and z directions (see Figs. 2.13 and 2.15). However, these branches exactly overlap with the absorption band (the gray shaded frequency intervals in Figs. 2.13 - 2.15) which was interpreted as a crystal field excitation of Tb^{3+} ions by the authors of [44]. It is possible that either this absorption band is actually the missing magnon branch, or Tb crystal field excitation hampers the detection of magnons in this energy interval. To clarify this question further investigations possibly involving other experimental techniques are necessary. In any case, the model describes the neutron scattering data rather well, especially given the fact that

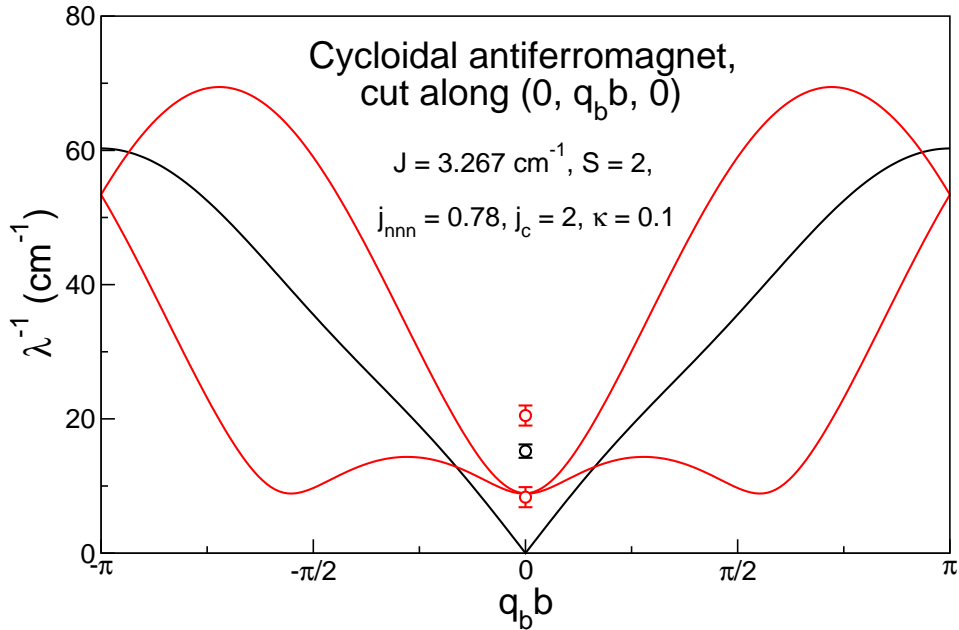


Figure 2.16: Magnon dispersion in a cycloidal antiferromagnet in the vicinity of Γ point. The notations of solid lines and parameters used are the same as in Fig. 2.13. The black and red circles with error bars show magnetic absorption lines in TbMnO_3 observed at $T = 22$ K in THz spectroscopy.

no refinement of exchange constants was made to obtain better fits. Such a refinement can be made taking the polarization of spin waves into account, which is available both from the model predictions and the experiments, at least partially. This task requires the deeper understanding of neutron scattering geometries with the access to the raw data and is beyond the scope of this thesis.

2.5.4 Antiferromagnetic resonances in optical spectroscopy

The magnons can also be seen in optical spectroscopy as magneto-active absorption lines. Due to very high speed of light the wave vector of these magnons is almost zero, $\mathbf{q} \approx 0$, and corresponds to the Γ point in the Brillouin zone. Figure 2.16 shows dispersion curves around Γ point for the same cycloidal antiferromagnet as in Figs. 2.13 - 2.15. The black line is the unshifted dispersion of the magnon with magnetic moment along the x axis while red lines are two magnons with polarization in yz plane. As the energies of magnons only in Γ point are of interest, the choice of the cut along the y direction in Fig. 2.16 is quite arbitrary.

The black and red circles with error bars are frequencies of AFMR lines observed in TbMnO_3 at $T = 22$ K. The measurements were performed on single crystals in a polarized THz beam and carry valuable experimental information about the magnon polarization. The black point denotes the magnon observed when the magnetic field of radiation is oriented along the x axis while two red points are magnons observed along the y direction. The higher frequency magnon can also be observed along the z axis (see also Fig. 7.3). Except for the lower frequency magnon along the y direction there

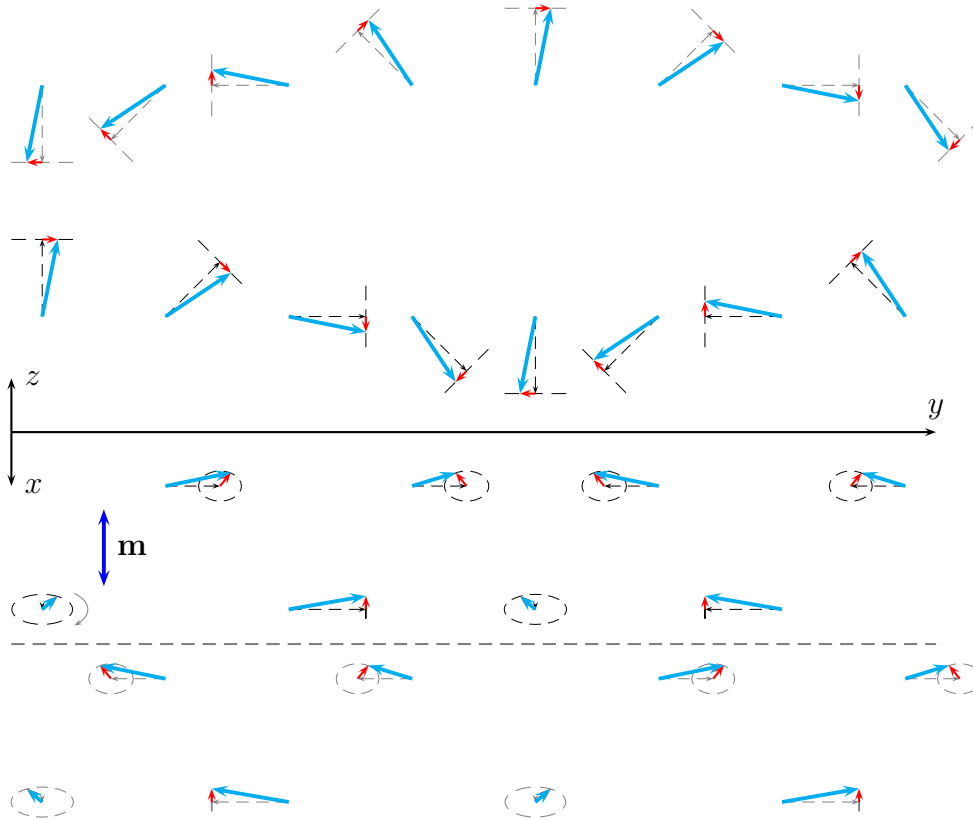


Figure 2.17: Schematic representation of a magnon at $\mathbf{q} = 0$ in the cycloidal antiferromagnet. The black dashed arrows represent the ground state, the cyan thicker arrows - orientations of spins in a wave and red arrows are the deviations of spins from their equilibrium orientations. Upper panel is a front view, lower panel - top view. The upper row of spins in the front view and lower row of spins in the top view with equilibrium spin orientations in gray show spins in the next layer along the z direction. The spins in the co-rotating frame are moving along elliptical orbits (black dashed ellipses) as shown by the gray arrow. This spin wave has nonzero dynamic magnetization along the x axis shown by the thick blue arrow.

are substantial deviations of the experimental data from the predictions of the model which will be discussed below.

The mode with magnetic moment along the x direction which originates from the unshifted dispersion in the co-rotating frame has zero frequency within the present model. The schematic movement of spins in this mode is illustrated in Fig. 2.17. The upper part of the figure is a front view of two layers of spins ordered antiferromagnetically along the z direction. The ground state spin cycloid is well seen in this representation. To obtain additional information about deviations of spins from their equilibrium orientations the top view is also required and is shown in the lower part of the figure. The view of one of the layers is shifted and separated by a gray dashed line from the view of another layer for clarity. All spins always have the same inphase deviations and the same orientations in the co-rotating frame. They are translated into inphase

oscillations of spin orientations along the x direction in the laboratory frame giving rise to uniform magnetic moment along this axis. Contrary, the components of spins along y and z directions are canceled out across the whole crystal due to continuous rotation of the ground state spin orientation. Substituting $\mathbf{q} = 0$ into equations (2.21) and (2.22) shows that both the frequency and amplitude of this mode along the x axis are zero due to $P(0) = 0$. The movements of spins in this case are simplified to uniform rotation of the whole cycloid around the x axis or, in other words, to the change in the phase of the static cycloid. The mode is therefore often called *phason* in the literature. There is also a general explanation why the frequency of the phason is zero: all spins are equivalent even taking Hamiltonian (2.17) into account, so it is possible to chose any spin to point, for example, strictly in the positive z direction without changing the energy of the system. Now, due to the incommensurability of the spin cycloid with the lattice constant, it is always possible to find some location on the spin cycloid to put the spin pointing in the positive z direction so that the spin at a given fixed location would point in the arbitrary predefined direction. Therefore, all spin cycloids with the spin at a given location pointing in any direction have the same energy so it is possible to continuously rotate the spin cycloid without changing its energy. Such property of the phason remains intact even after introduction of any anisotropy in the plane of spin cycloid as long as it does not violate translational invariance of the Hamiltonian and the ground state stays incommensurate. The possible explanation of the nonzero frequency of the phason observed experimentally is the pinning of the spin cycloid on various defects [45]. In such scenario the ground state remains incommensurate cycloidal in average. The randomly distributed defects introduce spin direction anisotropy on their sites also braking translational invariance. The emerging $P(0) \neq 0$ in equations (2.21) and (2.22) leads to both nonzero frequency and magnetic moment along the x axis of the phason and it is this case that is explicitly shown in Fig. 2.17.

Another contribution to the optical absorption is produced by two degenerate magnons with the wave vectors $\mathbf{q} = \pm\mathbf{Q}$ in the co-rotating frame. Examining polarization of these magnons in the laboratory frame using equation (2.24) it is easy to see that these magnons have nonzero magnetic moment which rotates in the yz plane clock- or counterclockwise depending on the sign of the wave vector. The degeneracy of these two magnons would be lifted in the presence of anisotropy in the plane of spin cycloid and the new splitted modes will be linearly polarized. It is therefore better to examine the symmetric and antisymmetric superpositions of the magnons at $\mathbf{q} = \pm\mathbf{Q}$ which represent two possible linearly polarized modes. According to (2.24), the symmetric combination is polarized along the y axis while antisymmetric - along the z axis.

Figure 2.18 schematically shows the antisymmetric mode. Being the combination of two propagating magnons with opposite wave vectors, this mode is a standing wave. The nodes are located at the sites with the spins pointing along the z direction whereas the antinodes are located at spins along the y direction. The x and y components of magnetic moment cancel out after averaging across the whole crystal and only the z component makes a contribution to the optical absorption. The higher experimentally observed AFMR mode (upper red circle in Fig. 2.16) can be attributed to this mode as it has z polarization too. The fact that it is also observed along the y axis can be explained

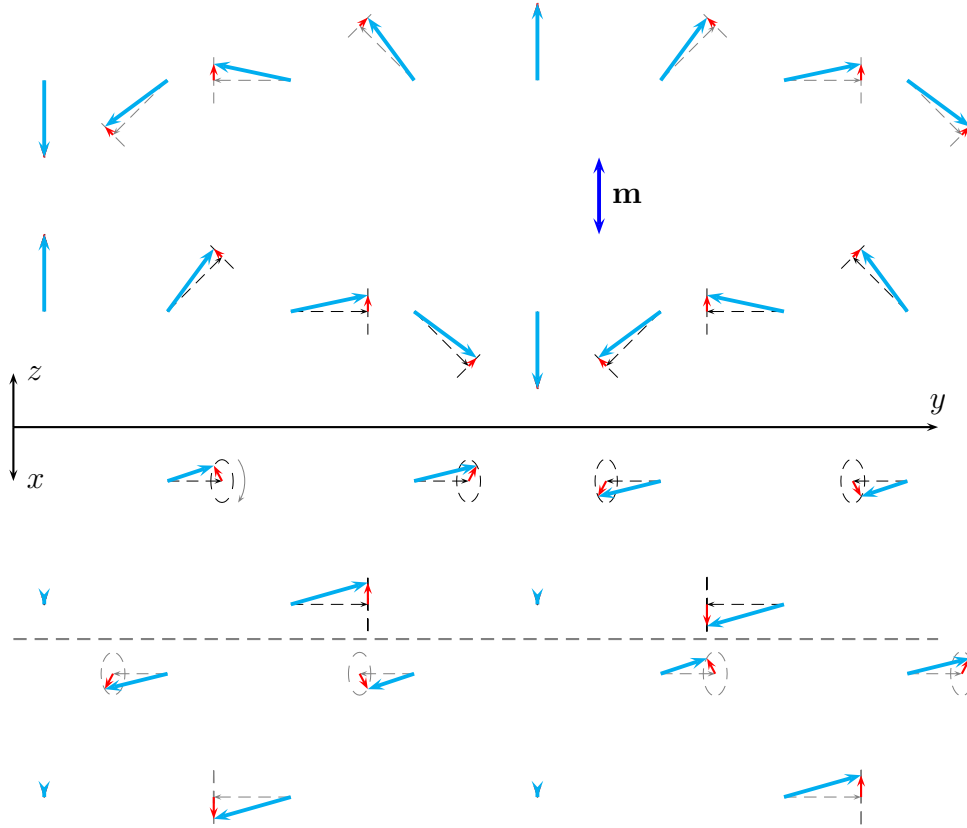


Figure 2.18: Schematic representation of the antisymmetric combination of magnons with $\mathbf{q} = \pm\mathbf{Q}$ in the cycloidal antiferromagnet. The notations are the same as in Fig. 2.17. The spins in the co-rotating frame are moving along elliptical orbits (black dashed ellipses) as shown by the gray arrow. This mode is a standing wave with the nodes on the spins pointing along the z direction and it has nonzero dynamic magnetization along this axis shown by the thick blue arrow.

assuming some remaining elliptical polarization of the mode instead of pure linear. The symmetric mode shown in Fig. 2.19 has similar structure as the antisymmetric one and is discussed in more detail below. It has dynamic magnetic moment in the y direction which coincides with experimentally observed excitation condition of the lower AFMR mode (lower red circle in Fig. 2.16).

In summary, although the current model has some shortcomings like inability to describe nonzero frequency of the phason or the splitting of the modes in yz plane, it still predicts the existence of three AFMR modes with correct excitation conditions. It also delivers a valuable information about the movement of individual spins in the analytical form. Moreover, other models can introduce more complicated interactions as small perturbations over the ground state and the excitations we derived in this chapter.

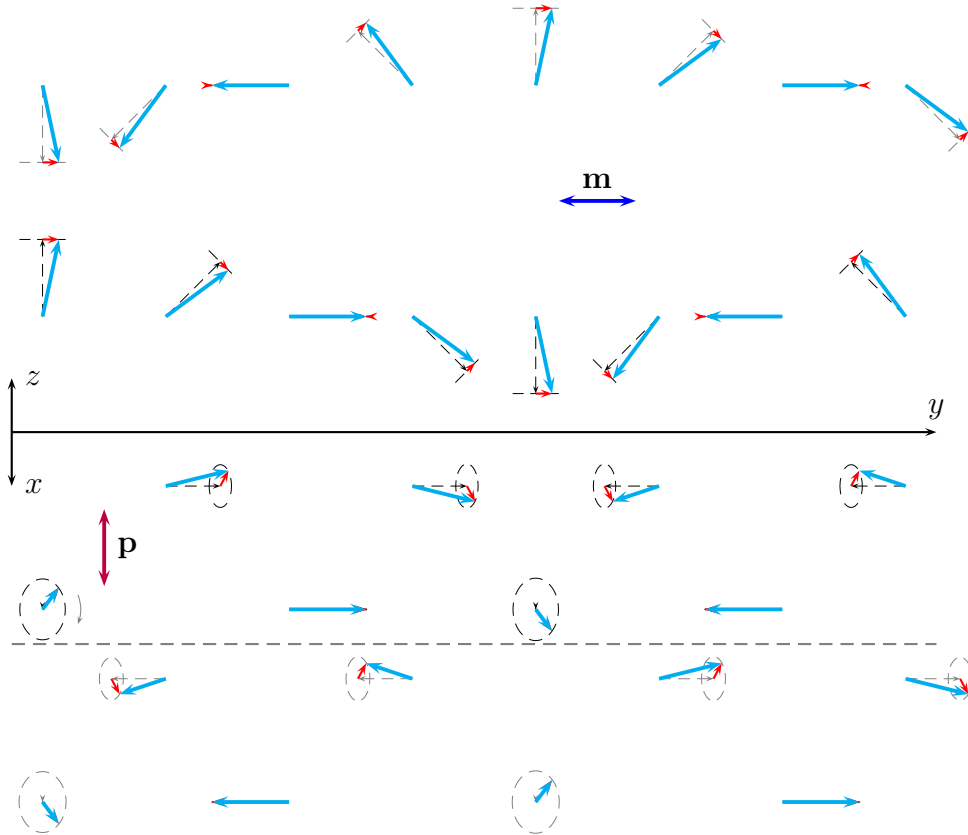


Figure 2.19: Schematic representation of the symmetric combination of magnons with $\mathbf{q} = \pm\mathbf{Q}$ in the cycloidal antiferromagnet. The notations are the same as in Fig. 2.17. The spins in the co-rotating frame are moving along elliptical orbits (black dashed ellipses) as shown by the gray arrow. This mode is a standing wave with the nodes on the spins pointing along the y direction and it has nonzero dynamic magnetization along this axis shown by the thick blue arrow. In the presence of IDM interaction the mode also gains an electric dipole along the x axis shown as a thick purple arrow.

2.5.5 Inverse Dzyaloshinskii-Moriya model of electromagnons

The first model proposed to describe the static electric polarization [46] and the strong optical absorption [38] both emerging in the cycloidal state of rare earth manganites was based on the inverse Dzyaloshinskii-Moriya (IDM) interaction. Another name widespread in the literature and used by authors of Ref. [38] is the spin current model. This interaction, first introduced phenomenologically [47], is basically a correction to a superexchange which accounts for the spin-orbit coupling [48]. In its general form the single term is written as:

$$H_{IDM,j} = \sum_{\alpha} \mathbf{d}_{\alpha} \left(\mathbf{r}_{j+\frac{1}{2}} \right) \cdot (\mathbf{S}_j \times \mathbf{S}_{j+1}).$$

The Dzyaloshinskii-Moriya vectors \mathbf{d}_{α} depend on the local symmetry of the bond connecting two spins. In case of the perovskite structure of rare earth manganites the

following vectors are allowed by the symmetry of Mn₂O bonds [49]:

$$\mathbf{d}_\alpha = \gamma \left(\delta_{j \rightarrow j+1} \times \mathbf{r}_{j+\frac{1}{2}} \right).$$

Here, γ is the strength of the interaction, vector $\delta_{j \rightarrow j+1}$ connects Mn spins j and $j+1$, and $\mathbf{r}_{j+\frac{1}{2}}$ is the displacement of the oxygen atom from the middle of the Mn-Mn bond. Using the properties of the mixed vector product the following expression for the IDM interaction part of the Hamiltonian can be obtained:

$$H_{IDM} = \gamma \sum_j \left(\delta_{j \rightarrow j+1} \times \mathbf{r}_{j+\frac{1}{2}} \right) \cdot (\mathbf{S}_j \times \mathbf{S}_{j+1}) = \gamma \sum_j \mathbf{r}_{j+\frac{1}{2}} \cdot ((\mathbf{S}_j \times \mathbf{S}_{j+1}) \times \delta_{j \rightarrow j+1}).$$

Taking the coordinate system and summation rules used in the present work into account, the IDM part takes the form:

$$\begin{aligned} H_{IDM} = -\gamma \sum_l \sum_j \sum_{k=j,j\pm 2, \dots} & \left(\mathbf{r}_{j-\frac{1}{2}, k+\frac{1}{2}, l} \cdot (\delta_{-1,1,0} \times (\mathbf{S}_{j,k,l} \times \mathbf{S}_{j-1, k+1, l})) + \right. \\ & \left. + \mathbf{r}_{j+\frac{1}{2}, k+\frac{1}{2}, l} \cdot (\delta_{1,1,0} \times (\mathbf{S}_{j,k,l} \times \mathbf{S}_{j+1, k+1, l})) \right), \end{aligned} \quad (2.25)$$

where vectors $\delta_{-1,1,0}$ and $\delta_{1,1,0}$ are:

$$\delta_{-1,1,0} = \begin{pmatrix} -a \\ b \\ 0 \end{pmatrix}; \quad \delta_{1,1,0} = \begin{pmatrix} a \\ b \\ 0 \end{pmatrix}.$$

In order to find displacements $\mathbf{r}_{j+\frac{1}{2}}$ and, therefore, the electric polarization \mathbf{P} , consideration of the phononic part of the Hamiltonian is required. Re-examination of the full spin Hamiltonian is also needed to account for the influence of the Jahn-Teller distortions on the magnetic structure. However, if the interaction constant γ is assumed to be small it is possible to use the ground state (2.23) and magnons (2.24) to calculate both static and dynamic spin induced polarizations in a perturbative manner. Indeed, the additional IDM energy (2.25) is linear in the displacement. Adding to the general quadratic term, the IDM interaction will lead to the shift of equilibrium atom positions in order to minimize total energy. On the qualitative basis the shifts of oxygen atoms will occur in the following directions with roughly the same amplitudes:

$$\mathbf{r}_{j-\frac{1}{2}, k+\frac{1}{2}, l} \uparrow \uparrow \delta_{-1,1,0} \times (\mathbf{S}_{j,k,l} \times \mathbf{S}_{j-1, k+1, l}); \quad \mathbf{r}_{j+\frac{1}{2}, k+\frac{1}{2}, l} \uparrow \uparrow \delta_{1,1,0} \times (\mathbf{S}_{j,k,l} \times \mathbf{S}_{j+1, k+1, l}).$$

An average electric polarization \mathbf{P} is then proportional to:

$$\mathbf{P} \sim \sum_l \sum_j \sum_{k=j,j\pm 2, \dots} \left(\mathbf{r}_{j-\frac{1}{2}, k+\frac{1}{2}, l} + \mathbf{r}_{j+\frac{1}{2}, k+\frac{1}{2}, l} \right) \sim \sum_l \sum_j \sum_{k=j,j\pm 2, \dots} \mathbf{P}_{j,k,l},$$

with the partial space dependent polarization

$$\mathbf{P}_{j,k,l} = \delta_{-1,1,0} \times (\mathbf{S}_{j,k,l} \times \mathbf{S}_{j-1, k+1, l}) + \delta_{1,1,0} \times (\mathbf{S}_{j,k,l} \times \mathbf{S}_{j+1, k+1, l}).$$

The expressions above contain products of spins which are assumed to be complex numbers. In order to obtain the real physical quantities it is necessary to take real or imaginary parts from the final result. Maintaining all intermediate expressions in complex form greatly simplifies the calculus. However, care should be taken in handling expressions containing the product of two or more complex quantities as $\text{Re}(ab) \neq \text{Re}(a)\text{Re}(b)$ for complex a and b . Namely, there are two types of products. One is a mathematical separation of the complex amplitude of the wave as in $A \cdot \exp(i(\mathbf{k}\mathbf{r} - \omega t))$, where the product should be taken in the complex form. Another type is the product of two real physical quantities like $\mathbf{S}_{j,k,l} \times \mathbf{S}_{j+1,k+1,l}$, where the product of the real or imaginary parts of the factors is indeed used. In the case above this does not lead to much of complications as only the zero and first order terms in amplitude \mathbf{A} are of interest. The expression for the static spin order (2.23) is real as a whole and for the real p and complex a it is possible to exchange the operations of multiplication and taking real or imaginary part: $\text{Re}(pa) = p\text{Re}(a)$.

Substituting expressions (2.23) and (2.24) for the total spin $\mathbf{S}_{j,k,l} = \hat{\mathbf{R}}_{k\alpha+l\pi}\mathbf{S}_0 + \hat{\mathbf{R}}_{k\alpha+l\pi}\mathbf{A}e^{i\mathbf{q}\mathbf{r}}$, the partial space dependent polarization $\mathbf{P}_{j,k,l}$ up to the terms linear in the wave amplitude \mathbf{A} can be easily found:

$$\begin{aligned} \mathbf{P}_{j,k,l}(\mathbf{q}) = & 2bS^2 \sin(\alpha) \begin{pmatrix} 0 \\ 0 \\ 1 \end{pmatrix} + 2bSA_y e^{i\mathbf{q}\mathbf{r}} \cos(\alpha) (\cos(q_a a) e^{iq_b b} - 1) \begin{pmatrix} 0 \\ 0 \\ 1 \end{pmatrix} + \\ & + SA_x e^{i(\mathbf{q}+\mathbf{Q})\mathbf{r}} \begin{pmatrix} ib (\cos(q_a a) e^{iq_b b} - e^{i\alpha}) \\ a \sin(q_a a) e^{iq_b b} \\ ia \sin(q_a a) e^{iq_b b} \end{pmatrix} + \\ & + SA_x e^{i(\mathbf{q}-\mathbf{Q})\mathbf{r}} \begin{pmatrix} -ib (\cos(q_a a) e^{iq_b b} - e^{-i\alpha}) \\ -a \sin(q_a a) e^{iq_b b} \\ ia \sin(q_a a) e^{iq_b b} \end{pmatrix}. \end{aligned}$$

The first term without wave amplitude \mathbf{A} gives the static part of electric polarization \mathbf{P}_0 . For the spin cycloid in the yz plane it has the only component along the z axis $P_0^{(z)} \sim NbS^2 \sin(\alpha)$ and it vanishes in the collinear phase. It also changes sign upon reversal of α , showing that the antiferromagnetic domains are simultaneously the ferroelectric domains.

The other terms linear in \mathbf{A} represent the dynamic part of electric polarization \mathbf{P}_A . In order to prevent the canceling out during summation over the crystal these terms should have no harmonic spatial dependence. This is achieved either at $\mathbf{q} = 0$ for the second term or at $\mathbf{q} = \pm\mathbf{Q}$ for the last two terms. In the first case the whole term will be still zero due to the factor $\cos(q_a a) e^{iq_b b} - 1 = 0$ at $\mathbf{q} = 0$. In the second case y and z components will be zero as they both contain factor $\sin(q_a a) = 0$ because of $Q_a = 0$. Taking only the space independent part of electric polarization into account, the only remaining component along the x axis is:

$$P_{j,k,l}^{(x)}(+\mathbf{Q}) = P_{j,k,l}^{(x)}(-\mathbf{Q}) = 2bSA_x \sin(\alpha).$$

Both magnons at $\mathbf{q} = +\mathbf{Q}$ and $\mathbf{q} = -\mathbf{Q}$ have the same contribution to the dynamic electric polarization. This means that the antisymmetric superposition of these magnons

shown in Fig. 2.18 has no electric moment while the symmetric combination has electric dipole moment along the x direction $P_A^{(x)} \sim NbSA_x \sin(\alpha)$ shown as a thick purple arrow in Fig. 2.19. The symmetric mode thus represents an electromagnon which is active along the x axis for the yz spin cycloid. Like the static polarization, the electromagnon disappears in the collinear phase. The simultaneously present magnetic moment along the y direction of this mode gives rise to a linear dynamic magnetoelectric effect given by a nonzero element χ_{xy} of the magnetoelectric tensor.

A detailed examination of the motion of spins in the symmetric mode provides a more intuitive explanation of the origin of IDM electromagnon commonly found in the literature. In the moment of time as illustrated in Fig. 2.19 all spins pointing in the positive z direction have deviations in the negative direction of the x axis and vice versa, the spin pointing in the negative z direction deviate in the positive x direction. Therefore, the spin cycloid in the whole crystal is slightly rotated around the y axis at this moment of time and the movement of spins in the symmetric mode can be viewed as a small oscillatory rotation of the cycloid. Now, the electric polarization is determined by the orientation of spins only and should also slightly rotate around the y axis away from its ground state direction along the z axis. Such rotations give rise to the dynamic component of electric moment along the x axis.

2.5.6 Heisenberg exchange model of electromagnons

One important prediction of the previous model is the coupling of the excitation condition of electromagnon to the orientation of the spin cycloid. However, the experimental findings have shown the opposite, as electromagnons were always excited by an electric field along the x direction, irrespectively whether the spin cycloid was in xy or yz planes. Such discrepancy stimulated the search for new underlying mechanisms. A successful attempt is the exchange striction model of spin-phonon coupling based on the symmetric Heisenberg exchange (HE) [40, 50].

The nearest-neighbour exchange constant J depends generally upon the positions \mathbf{r} of the oxygen atoms in Mn-O-Mn bonds and it is possible to expand it in Taylor series:

$$J(\mathbf{r}) = J(0) + \frac{\partial J}{\partial \mathbf{r}} \cdot \mathbf{r} = J(0) + \frac{\partial J}{\partial \phi} \frac{\partial \phi}{\partial \mathbf{r}} \cdot \mathbf{r}. \quad (2.26)$$

Here ϕ is the Mn-O-Mn bond angle (see Fig. 2.20). In this case the most important dependency comes not from the displacement of oxygen atoms itself, but indirectly from the change of Mn-O-Mn bond angle caused by the displacements. The exchange constant J is maximal for the straight angle $\phi = \pi$ and decreases with decreasing angle as it follows from the Goodenough-Kanamori-Anderson rules. The equilibrium angle ϕ_0 substantially differs from π for rare earth manganites in question (see Fig. 1.11), so the nonvanishing first derivative $\partial J / \partial \phi > 0$ exists and is the same for all Mn-O-Mn bonds. On the other hand, the tilting Jahn-Teller distortions, schematically shown in Fig. 2.20, lead to the alternating derivative $\partial \phi / \partial \mathbf{r}$. Using the same indexing scheme as in Fig. 2.12, the derivative can be represented as $\partial \phi / \partial x \sim (-1)^k$. Assuming that the oxygen displacements are caused by the applied electric field \mathbf{E} it is possible to write

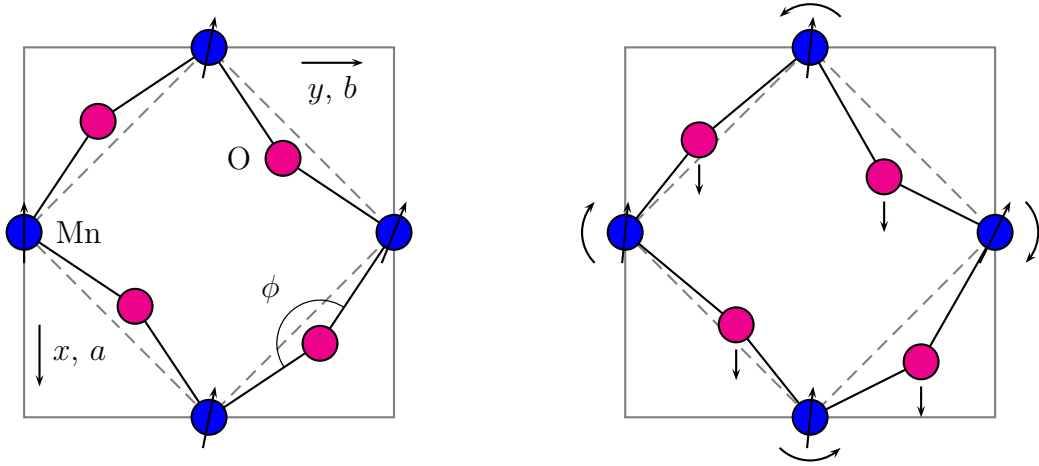


Figure 2.20: Scheme of the symmetric Heisenberg exchange interaction accounting for the Jahn-Teller distortions in rare earth manganites. The ab crystallographic plane of the orthorhombic unit cell with the most important for the model tilting distortions is shown in the left frame. The blue circles are Mn atoms with the spins shown as black arrows. The magenta circles represent the oxygen atoms with the black lines along Mn-O-Mn bonds. The dashed gray lines show the bonds in the undistorted perovskite structure. The uniform shift of all oxygen atoms along the a direction shown on the right side causes the modulation of the ferromagnetic nearest neighbour exchange along the b axis. The exchange constant between the left and two middle Mn spins is increased while the exchange constant between the right and the middle spins is decreased. The induced spin rotations are shown by the black curved arrows.

$\mathbf{r} \sim \mathbf{E}$ and $r_x \sim E_x$. Substituting (2.26) into the general expression for the exchange interaction $J(\mathbf{S}_j \cdot \mathbf{S}_{j+1})$, the first term gives the nearest-neighbour ferromagnetic exchange already included in (2.17). The second term is the required spin-phonon coupling and can be expressed as [40]:

$$H_{HE} = -gE_x \sum_l \sum_j \sum_{k=j,j\pm 2,\dots} (-1)^k ((\mathbf{S}_{j,k,l} \cdot \mathbf{S}_{j-1,k+1,l}) + (\mathbf{S}_{j,k,l} \cdot \mathbf{S}_{j+1,k+1,l})). \quad (2.27)$$

Within the present indexing scheme it is possible to write $(-1)^j$ instead of $(-1)^k$ under the sum. Indeed, $(-1)^{j-k} = 1$ as $j - k$ is always even. Now, $(-1)^k = (-1)^k \cdot 1 = (-1)^k (-1)^{j-k} = (-1)^j$. The physical meaning of such a symmetry will be clear below.

The coupling of magnons to the lattice vibrations occurs schematically as follows. The uniform shift of all oxygen atoms in the MnO_2 planes along the x axis, shown in the right frame of Fig. 2.20, causes the angle ϕ to increase for the two left Mn-O-Mn bonds and to decrease for the two right bonds. The increased exchange constant for the two left Mn-O-Mn bonds would cause the left Mn spin to align with the two central spins while the right Mn spin would tend to misalign with the central spins due to the decreased exchange constant for the two right bonds. The effective torques due to oxygen displacements act upon Mn spins in alternating directions while moving along the zigzag Mn chains in x or y directions. The torque forces are shown in the right frame of Fig. 2.20 by the curved arrows. Therefore, the uniform shift of oxygen atoms in MnO_2 planes caused, for example, by the uniform electric field along the x axis is expected to couple to the magnon at the boundary of the Brillouin zone.

The electric polarization can be easily found according to the thermodynamic relation $\mathbf{P} = -\partial H/\partial \mathbf{E}$. Analogously to the case of IDM interaction, the x component of the averaged polarization is given by:

$$P^{(x)} \sim \sum_l \sum_j \sum_{k=j, j\pm 2, \dots} P_{j,k,l}^{(x)},$$

with the space dependent polarization

$$P_{j,k,l}^{(x)} = (-1)^k ((\mathbf{S}_{j,k,l} \cdot \mathbf{S}_{j-1,k+1,l}) + (\mathbf{S}_{j,k,l} \cdot \mathbf{S}_{j+1,k+1,l})).$$

Substituting expressions (2.23) and (2.24) for the total spin $\mathbf{S}_{j,k,l}$, the following expression is easily found:

$$P_{j,k,l}^{(x)} = 2S(-1)^k (S \cos(\alpha) + A_y \sin(\alpha) (1 - \cos(q_a a) e^{i q_b b}) e^{i \mathbf{q} \mathbf{r}}).$$

The static term vanishes for the spin cycloid due to alternations of spin-phonon interaction along the y axis. However, it predicts a nonzero spontaneous polarization for the “up-up-down-down-...” spin order [40] typical for rare earth manganites at the right part of the incommensurate phases in the Mn-O-Mn bond angle diagram 1.11.

Contrary to the static term, the dynamic part of electric polarization exists only in the noncollinear magnetic structures as, otherwise, $\sin(\alpha) = 0$. In order to obtain the average dynamic polarization the wave exponent has to be $\exp(i \mathbf{q} \mathbf{r}) = \exp(i(\pm\pi/b)bk) = (-1)^k$ or $\exp(i \mathbf{q} \mathbf{r}) = \exp(i(\pm\pi/a)aj) = (-1)^j$. The seemingly four different wave vectors are actually the same and they are at the same point in the reciprocal space. They correspond to the four black circles in the corners of the Brillouin zone in Fig. 2.12. The ambiguous representation of the zone corner point explains the existence of two different notations for the spin-phonon coupling (2.27).

Figure 2.21 shows the exaggerated motion of spins for the zone corner magnon. It can be well seen that for the moment of time depicted in the figure the first two spins in the zigzag Mn chain are almost perfectly aligned with each other. Therefore the Mn-O-Mn bond between the first and the second Mn spins forms almost a straight angle. The same is also true for the third and fourth spins and so on. The second and the third spins in the chain are contrary quite misaligned so the Mn-O-Mn angle for this pair is considerably smaller than the straight angle. The average displacement of oxygen atoms required to produce such a pattern occurs in the positive x direction producing dynamic electric polarization $P_A^{(x)} \sim N S A_y \sin(\alpha)$ shown as a thick purple arrow in Fig. 2.21. In the next half period of spin wave oscillation the picture will be the opposite and the displacements of oxygen atoms will be in the negative direction of the x axis.

Up to now only the coupling of electric field along the x axis to the magnons was considered. In general, the uniform shift of all oxygen atoms in one of the crystallographic directions leads to the modulation of the exchange constants along other axes as well. Indeed, as can be easily seen from the crystal structure shown in Fig. 1.8, the shift of oxygen atoms along the x axis leads to the modulation of exchange constants along y and z directions, the shift in the y direction leads to modulations along x and

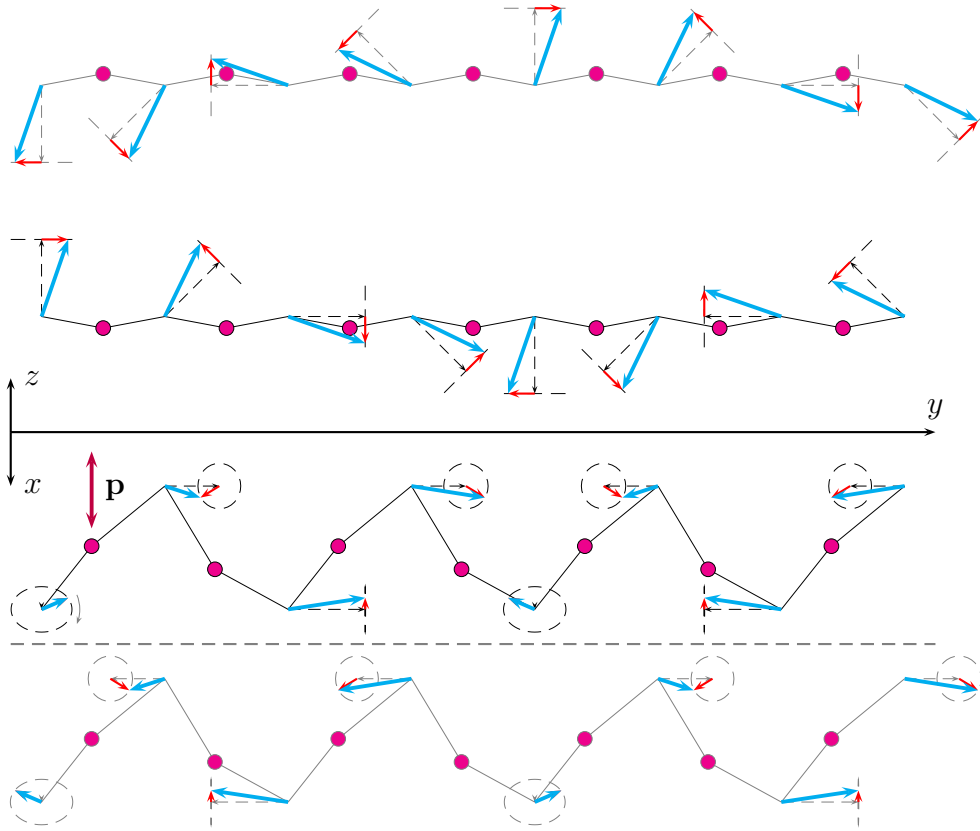


Figure 2.21: Schematic representation of the magnon in the corner of the Brillouin zone in the cycloidal antiferromagnet. The notations are the same as in Fig. 2.17 with additional magenta circles representing oxygen atoms in MnO_2 planes. The spins in the co-rotating frame are moving along elliptical orbits (black dashed ellipses) as shown by the gray arrow. In the presence of HE interaction the oxygen atoms move towards the center of Mn-O-Mn bond if the adjacent spins are almost collinear and in the opposite direction if spins are less aligned. The overall motion of oxygen atoms yields the electric dipole moment along the x axis shown as a thick purple arrow.

z directions and the shift in the z direction causes the modulation along the x axis. The new coupling terms along x and z axes do not result, however, in the excitations of magnons because the spin order along these directions is collinear and is not sensitive to the small modulation of exchange constant. It is the combination of the structural peculiarities of the distorted perovskites and the sensitivity of the cycloidal spin order to small perturbations of the exchange constant that leads to the unique excitation condition $e\|a$ of electromagnons within Heisenberg exchange model.

Further theoretical attempts based on the symmetric exchange to describe low frequency electromagnons also exist [41, 51]. One of the approaches is to include various additional terms into the spin Hamiltonian to obtain an elliptical cycloidal state. These elliptical distortions lead to the appearance of electro-activity at other wave vectors on the magnon branches with lower frequencies. However the amplitude of elliptical dis-

tortion required to obtain the observed strength of the low frequency electromagnon is too high and the origin of the low frequency electromagnon is still under the debate.

3 Experimental techniques

Most of the results in this thesis were obtained using quasi-optical spectrometry in the frequency range 60-1200 GHz ($2\text{-}40\text{ cm}^{-1}$). From the experimental point of view, this range fills the gap between microwave and far infrared regions of the electromagnetic spectrum. From the physical point of view, the photon energies match the magnons, i.e. excitations of the spin subsystem in a large number of magnetically ordered materials. As the ferroelectricity and magnetoelectric effects in rare earth manganites are caused by magnetic order, terahertz (THz) spectroscopy is a natural choice for the study of magnetoelectric dynamics in these systems. A general overview of Mach-Zehnder interferometric arrangement, some specific details of the most crucial components of the spectrometer, and the measurement procedure are discussed first. Details of the spectra treatment in the case of coherent radiation, typical for the present setup, are provided afterwards. The samples of rare earth manganites, studied in this work, are discussed in the last subsection.

3.1 Mach-Zehnder interferometer

A schematic drawing of a Mach-Zehnder spectrometer is shown in Fig. 3.1. The radiation originates from the backward wave oscillator (BWO), which can be viewed as a point-like source with a good accuracy [52, 53]. The lens in front of the BWO transforms the diverging spherical beam into the parallel one. The beam splitter consists of a wire grid polarizer. The radiation with electric field perpendicular to the wires passes through, while the radiation with electric field along the wires is almost perfectly reflected. This implies that the beams in the main and reference arms have orthogonal polarizations. Another wire grid polarizer in front of the beam splitter is used to adjust the amplitudes of the main and reference beams. Both beams are joined together in the same way – the polarizer with the setting, rotated by 90° relative to the beam splitter, reflects the main beam and passes the reference beam to the detector. As the polarizations of these two beams are still orthogonal to each other, they cannot interfere. A wire grid analyzer is placed before the detector to rotate the polarizations of the beams to the common direction. The combined beam is focused on the detector – a liquid helium cooled bolometer. Two lenses in the main arm are used to focus the beam on the sample, which is placed in the common focal plane of the lenses. The sample has to be at least 2-3 wavelengths in diameter in order to avoid diffraction effects. Smaller samples can also be measured, but only in the scanning mode, where the changes in transmittance as a function of magnetic field or temperature are of the interest (see below). Identical lenses are placed in the reference arm to compensate for the additional phase shift due to

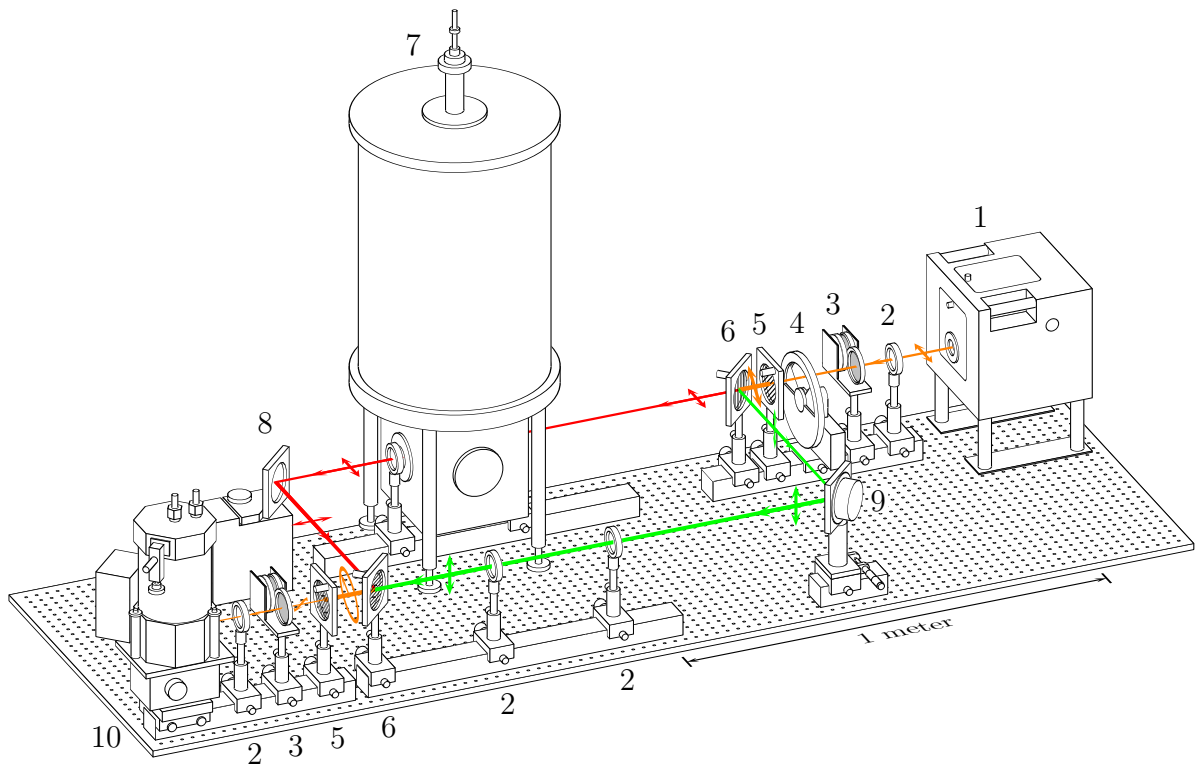


Figure 3.1: Scheme of a submillimeter Mach-Zehnder interferometer. The main arm with the sample is in the upper left of the scheme (red rays), while the reference arm is shown in the right bottom by the green rays. Short arrows indicate the polarization of the beams. 1 – backward wave oscillator (BWO), 2 – lenses, 3 – attenuators, 4 – chopper, 5 – wire grid polarizers, 6 – wire grid beam splitters, 7 – Oxford cryomagnet, 8 – movable mirror, 9 – oscillating mirror (phase modulator), 10 – bolometer.

the optical thickness of the lenses in the main arm. The beams in both arms are reflected by 45° incidence mirrors. One of the mirrors is able to oscillate at low frequency (around 20-30 Hz), while the other can be continuously moved within a range of 10 mm. Both of these degrees of freedom are necessary during the phase measurements. In order to apply magnetic fields up to 8 T and at temperatures ranging from 2 to 300 K, the sample is placed in a commercial cryomagnet from Oxford Instruments. It has four optical windows fitted with 50-70 μm thick Mylar (polyethylene terephthalate = PET foil), which is highly transparent for the radiation in the THz frequency range.

Backward wave oscillators are vacuum tube-based sources of continuous radiation. Free electrons are emitted by the heated cathode and accelerated by the voltages up to 6 kV. The electrons are collimated into a narrow beam by an external magnetic field and travel along the slow wave structure. The emitted waves travel in the opposite direction, which leads to the name BWO. The maximum energy transfer from the electron beam to the THz radiation takes place, when the effective phase velocity of the radiation coincides with the velocity of electrons. The velocity of electrons v_e is proportional to the square root of the accelerating voltage U , $v_e \propto \sqrt{U}$. Thus, by changing the voltage U , the frequency of the radiation can be tuned by a factor of 1.5-2. On the contrary, the

intensity of the outgoing radiation cannot be tuned intrinsically. A set of fixed attenuators is used instead, to meet the transmittance of particular samples. In order to cover the frequency range 38-1050 GHz, 9 backward wave oscillators of different construction are used. Compared to other sources of continuous THz radiation like photomixing generators or synchrotron radiation, BWOs are very compact and often provide much higher output intensities. The most observable drawback is almost complete cessation of the production (with only one single Russian company on the market). For more information about BWOs and other optical elements of the submillimeter Mach-Zehnder interferometer, see Ref. [53].

The liquid helium cooled bolometer is available commercially as a detector for far infrared spectral range. At the core of the bolometer is a small piece of semiconductor with a very high temperature coefficient of resistivity at 4 K. The incoming radiation heats the semiconductor and the rise of its temperature can be detected as a change of the resistance. Very low specific heat at helium temperatures also significantly increases the sensitivity of the bolometer. As the absorbed heat is measured directly, it also has almost frequency independent characteristic. However, such a detector does not have a well defined zero – the resistance can slowly drift with the time due to various factors. In order to overcome this feature and also to increase signal to noise ratio, a lock-in detection technique is used in both transmission and phase measurement modes.

In the transmission measurement mode, the reference arm is closed with a thick absorber of THz radiation, and only the main path is used. The beam is modulated mechanically by the chopper, which is made of a metal disc divided into sectors. The size of the sectors is chosen in such a way, that the radiation can fully pass through the empty sectors and is completely reflected by the metal ones. This ensures the maximal depth of the modulation. The detected signal as a function of frequency is measured twice: the first time without the sample, yielding the reference spectrum $I_{ref}(\omega)$, and the second time with the sample, obtaining $I_{sam}(\omega)$. The intensity transmission coefficient through the sample is calculated as $T(\omega) = |t(\omega)|^2 = I_{sam}(\omega)/I_{ref}(\omega)$. Here, $t(\omega)$ is the complex transmission coefficient (see the next section). The procedure above is accurate, if the radiation reflected from the sample can be ignored. In reality, however, this part of radiation is reflected back by various optical elements and still reaches the detector. The frequency-dependent interference of these secondary beams with each other and with the primary beam leads to the formation of a complex structure of maxima and minima in the observed spectrum. These irregular oscillations are superimposed to the intrinsic spectrum of the sample, giving it a “noisy” look (see Fig. 3.3, for example). However, the standing wave pattern is highly reproducible and can easily be obtained e.g. on the next day, provided the measurement arm was not changed in between. The limited sample volume in the Oxford cryomagnet (26 mm bore) with a lot of metallic cladding increases the effects of the standing waves. If higher quality spectra in zero magnetic fields are required, another cryostat with larger windows and sample volume is used. Another way is to measure the detector signal as a function of magnetic field or as a function of temperature at a fixed frequency. In most cases, the changes of the sample properties are not large enough to significantly alter the amplitude of the reflected wave or the diffraction pattern from the small sample. A much smoother curve

is obtained, allowing to detect fine changes in the optical parameters of the sample. Calibration without the sample is normally not performed, but the whole dependency is scaled to give the same value of transmission as obtained from the spectrum at the initial conditions (zero field or some fixed temperature).

In the phase measurement mode, both arms of the interferometer are opened. The main beam is phase modulated via the oscillating mirror, while the movable mirror in the reference beam adjusts the static phase shift. In order to better understand the procedure of phase stabilization, automatically performed by an electronic block of the spectrometer, a simple mathematical formulation would help. Assume that the electric field at the detector of the wave from the main arm is $E_{sam} \sin(\varphi_{sam} - \omega t)$, and of the wave from the reference arm is $E_{ref} \sin(\varphi_{ref} - \omega t)$. The power P detected by the bolometer is proportional to the time average of the square of the total electric field. The square of the total field can be transformed to

$$\begin{aligned} P(t) &\propto (E_{sam} \sin(\varphi_{sam} - \omega t) + E_{ref} \sin(\varphi_{ref} - \omega t))^2 = \\ &= E_{sam}^2 \sin^2(\varphi_{sam} - \omega t) + E_{ref}^2 \sin^2(\varphi_{ref} - \omega t) + \\ &+ E_{sam} E_{ref} (\cos(\varphi_{sam} - \varphi_{ref}) - \cos(\varphi_{ref} + \varphi_{sam} - 2\omega t)), \end{aligned}$$

with the time-averaged value

$$P \propto E_{sam}^2 + E_{ref}^2 + 2E_{sam}E_{ref} \cos(\varphi_{sam} - \varphi_{ref}).$$

As the fields E_{sam} and E_{ref} are assumed to be constant (not modulated), only the interference term can be detected by the lock-in amplifier. The arms of the interferometer are adjusted during initial assembly to have the same optical length without the sample and with the movable mirror near the middle of the range. The phase difference can be written then as

$$\varphi_{sam} - \varphi_{ref} = \varphi_t + \delta\varphi - \frac{2\pi}{\lambda}d - \frac{2\pi}{\lambda}\Delta l = \varphi_t - \frac{2\pi}{\lambda}(d + \Delta l) + \delta\varphi = \Delta\varphi + \delta\varphi.$$

Here, $\delta\varphi = (2\pi\delta l/\lambda) \cos(\Omega t)$ is the phase modulation of the main beam due to the oscillations of the mirror with the amplitude δl and frequency Ω , φ_t is the phase of the wave transmitted through the sample with the thickness d , $2\pi d/\lambda$ is the phase of the wave in the reference path gained on the same distance d as the thickness of the sample and Δl is the compensating displacement of the movable mirror. The necessity to subtract the term $2\pi d/\lambda$ in the expression above can be easily demonstrated, as follows. The transmission phase for a virtual sample made of air is $\varphi_t = 2\pi d/\lambda$. The term under discussion and φ_t cancel each other then, yielding $\Delta l = 0$, as expected. Rewriting the interference term, we get

$$P \propto E_{sam}E_{ref} \cos(\Delta\varphi + \delta\varphi) = E_{sam}E_{ref} (\cos(\Delta\varphi) \cos(\delta\varphi) - \sin(\Delta\varphi) \sin(\delta\varphi)).$$

Assuming moderate modulation depth $\delta\varphi = \delta\varphi_0 \cos(\Omega t) < 1$, the expression above can be expanded into Taylor series up to the terms quadratic in the amplitude $\delta\varphi_0$. The first term with $\cos(\delta\varphi)$ gives zero and second harmonic contributions in terms of modulation

frequency Ω . The zero frequency component is not detected experimentally and will be omitted in the following expression. The second term with $\sin(\delta\varphi)$ gives the first harmonic contribution:

$$P \propto -E_{sam}E_{ref} \cos(\Delta\varphi) \frac{\delta\varphi_0^2}{4} \cos(2\Omega t) - E_{sam}E_{ref} \sin(\Delta\varphi) \delta\varphi_0 \cos(\Omega t). \quad (3.1)$$

The algorithm of the automatic phase compensation procedure can now be easily explained. The amplitude of the first harmonic $A_1 \propto -E_{sam}E_{ref} \sin(\Delta\varphi) \delta\varphi_0$ depends on the displacement of the movable mirror Δl , because $\Delta\varphi = \varphi_t - 2\pi(d + \Delta l)/\lambda$. If A_1 is positive, the mirror is moved in one direction, otherwise – in the opposite direction. The mirror will then move towards the position where $\sin(\Delta\varphi) = 0$. The directions of the movements are chosen in such a way that $\Delta\varphi = 2\pi m$ are the stable points. The integer number m is called the interference order. From the stabilization condition $\Delta\varphi = 2\pi m = \varphi_t - 2\pi(d + \Delta l)/\lambda$ it follows that the mirror position is generally dependent on the wavelength: $\Delta l = (\varphi_t \lambda)/(2\pi) - d - m\lambda$. The only exception is when the interferometer is in the zero-th order. This fact is used to find it manually. Note that the optical thickness of the sample $(\varphi_t \lambda)/(2\pi) = nd$ is almost wavelength independent, unless a strong dispersion of the refractive index n is present. In zero-th interference order the mirror displacement is directly related to the transmission phase of the sample: $\Delta l = (\varphi_t \lambda)/(2\pi) - d$. The overall procedure is similar to the transmission measurements. The mirror position without the sample is obtained first, to get the calibration curve $\Delta l_{ref}(\omega)$. The measurement with the sample yields $\Delta l_{sam}(\omega)$. The required phase shift across the sample is now $\varphi_t(\omega) = 2\pi(\Delta l_{sam}(\omega) - \Delta l_{ref}(\omega) + d)/\lambda(\omega)$. If the phase shift is measured as a function of magnetic field or temperature, the calibration is not performed, but the whole curve can be shifted by a constant value, to coincide with the known point.

It can be easily seen from expression (3.1), that if the amplitude of the first harmonic is zero, the amplitude of the second harmonic is maximal and is proportional to the field in the main arm E_{sam} . Therefore, the absolute value of the complex transmission coefficient $|t(\omega)| = \sqrt{T(\omega)} \propto E_{sam}$ can be obtained by measuring the amplitude of the second harmonic. This mode is often used in the magnetic field or temperature scans.

During the measurements at room temperature without magnetic field, the sample can be removed for the calibration simply by hand. In the case when one of the cryostats is involved, a special sliding sample holder is used, allowing removal of the sample out of the beam. The Oxford cryomagnet has its superconducting windings in the form of two split coils, inducing magnetic field in the horizontal plane. The beam can pass through the central hole of the coils, or along the perpendicular direction between the coils. The change between these arrangements is achieved via rotating the whole cryomagnet by 90° with a lifting crane. The arrangement where the magnetic field is directed along the beam is called Faraday geometry, while the arrangement with the magnetic field perpendicular to the beam is called Voigt geometry.

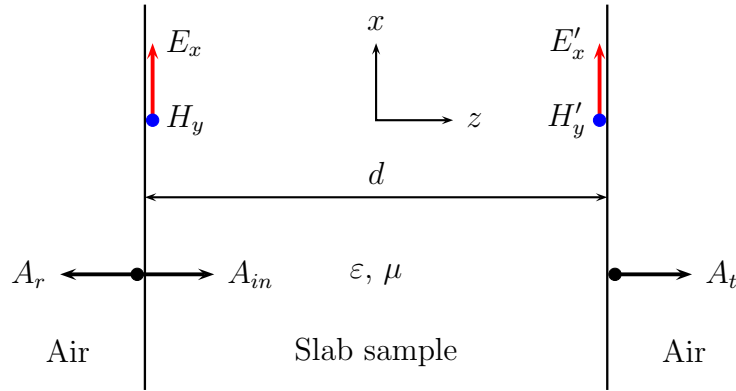


Figure 3.2: Cross section of the plane-parallel sample with the thickness d , permittivity ε and permeability μ . The incident wave with the amplitude A_{in} (shown as a black arrow) comes from the left. The reflected wave with the amplitude A_r propagates back in the negative z direction. The transmitted wave with the amplitude A_t travels further towards the detector. The cumulative electric field at the left boundary of the sample is denoted as E_x , on the right boundary – as E'_x (shown as red arrows). Similarly, the total magnetic field on the left boundary is H_y , and on the right boundary is H'_y (blue circles, magnetic fields are directed normal to the plane of the figure).

3.2 Analysis of the spectra

All measurements in the present work were done in the slab geometry under the normal incidence of the radiation onto the samples. The electric and magnetic fields of the beam were always directed along the principle axes of the dielectric $\hat{\varepsilon}$ and magnetic $\hat{\mu}$ tensors. In this case the complex transmission and reflection coefficients can be obtained in the simpler model, which assumes that the plane-parallel sample is isotropic with permittivity ε and permeability μ . The cross section of such a sample is shown in Fig. 3.2.

Assume that the linearly polarized incident wave with the amplitude A_{in} falls on the sample of the thickness d from the left. What should be calculated are the amplitudes of reflected A_r and transmitted A_t waves (shown as black arrows in Fig. 3.2). The polarization of the waves is assumed with the electric field along the x axis and the magnetic field along the y axis. The propagation direction of the waves is along the z axis. The total electromagnetic field of the radiation inside the sample can be decomposed into two waves, traveling in the opposite directions. The wave with the positive propagation direction has the relation $E_x^+ = \zeta H_y^+$ between electric E_x^+ and magnetic H_y^+ fields at each point within the sample. Here,

$$\zeta = \sqrt{\frac{\mu}{\varepsilon}}$$

is the dimensionless impedance (Gaussian units are assumed). The electric field at the right boundary of the sample $E_{2,x}^+$ is connected to the field on the left boundary $E_{1,x}^+$ via the relation $E_{2,x}^+ = E_{1,x}^+ e^{ikd}$. The wave vector k can be calculated from the dispersion

relation

$$k = \sqrt{\varepsilon\mu} \frac{\omega}{c},$$

where ω is the angular frequency of the coherent radiation. Here, the form $e^{i(kz-\omega t)}$ of a plane wave is assumed. Similarly, for the wave with the negative propagation direction, the relations $E_x^- = -\zeta H_y^-$ and $E_{2,x}^- = E_{1,x}^- e^{-ikd}$ hold. Using these four equations, it is possible to connect the total electric $E_x = E_{1,x}^+ + E_{1,x}^-$ and magnetic $H_y = H_{1,y}^+ + H_{1,y}^-$ fields on the left boundary with the total fields $E'_x = E_{2,x}^+ + E_{2,x}^-$ and $H'_y = H_{2,y}^+ + H_{2,y}^-$ on the right boundary (see also the definition of the matrix \hat{W} below). This relation can be written in the matrix form $\mathbf{V}' = \hat{M}\mathbf{V}$, where

$$\mathbf{V} = \begin{pmatrix} E_x \\ H_y \end{pmatrix}; \quad \mathbf{V}' = \begin{pmatrix} E'_x \\ H'_y \end{pmatrix}; \quad \hat{M} = \begin{pmatrix} \cos(kd) & i\zeta \sin(kd) \\ i\zeta^{-1} \sin(kd) & \cos(kd) \end{pmatrix}.$$

The matrix \hat{M} is called transfer matrix.

The choice of the total electric and magnetic fields as intermediate variables has at least two advantages. Firstly, in the absence of conducting surfaces like two dimensional electron gases, the tangential components of both electric and magnetic fields are continuous across the boundaries. In the case of a single layer, as in Fig. 3.2, the fields just outside the sample are the same as just within the sample, that is, \mathbf{V} on the left boundary and \mathbf{V}' on the right boundary in Fig. 3.2. In the case, when the sample consists of m different layers, the relation between fields at two outermost surfaces has the same form $\mathbf{V}' = \hat{M}_{total}\mathbf{V}$. The total transfer matrix \hat{M}_{total} is easily calculated as a product of transfer matrices of single layers: $\hat{M}_{total} = \hat{M}_1\hat{M}_2 \dots \hat{M}_m$. Secondly, if the effects of polarization rotation within the sample have to be accounted for, more complex 4×4 -matrix formulation [54] is required. However, it is a generalization of the present method and it also uses the total fields as intermediate variables. Two dimensional conducting surfaces can also be easily described within the current formalism, see the supplementary material of Ref. [55], for example.

The total electric and magnetic fields on the left side of the sample are composed from the amplitudes of incident and reflected waves (see Fig. 3.2). Generally, such composition can also be written in the matrix form: $\mathbf{V} = \hat{W}\mathbf{A}$, where

$$\mathbf{A} = \begin{pmatrix} A^+ \\ A^- \end{pmatrix}; \quad \hat{W} = \begin{pmatrix} 1 & 1 \\ 1 & -1 \end{pmatrix};$$

A^+ is the amplitude of the wave traveling in the positive direction of the z axis, and A^- – of the wave in the negative direction. Either electric or magnetic field can be chosen as an amplitude of the wave. Both choices lead to the same result up to the sign of the reflection coefficient. The matrix \hat{W} above is written for the case when electric field is the amplitude of the wave: $A^+ = E_x^+$ and $A^- = E_x^-$. The system of equations to find the reflected and transmitted waves is then:

$$\begin{pmatrix} A_t \\ 0 \end{pmatrix} = \hat{W}^{-1}\hat{M}\hat{W} \begin{pmatrix} A_{in} \\ A_r \end{pmatrix}; \quad \begin{pmatrix} t \\ 0 \end{pmatrix} = \hat{W}^{-1}\hat{M}\hat{W} \begin{pmatrix} 1 \\ r \end{pmatrix}.$$

Here, the fact that there is no wave coming from the detector is used. The complex transmission t and reflection r coefficients are defined as $t = A_t/A_{in}$ and $r = A_r/A_{in}$. Solving the last system of two equations in two variables t and r , the following expression of the transmission coefficient through a single layer slab can be obtained:

$$t = \left(\cos(kd) - i \frac{\zeta + \zeta^{-1}}{2} \sin(kd) \right)^{-1}. \quad (3.2)$$

If the sample is anisotropic, the values of permittivity and permeability should be taken along appropriate principal axes. For example, in the case shown in Fig. 3.2, $\varepsilon = \varepsilon_x$ and $\mu = \mu_y$ are to be taken. The values of ε_y and μ_x can be obtained on the same sample by rotating the incident polarization by 90° . In order to obtain the z -components of permittivity and permeability, at least one other sample with the x or y axis along the beam is required. If the excitations of both electric and magnetic nature are intermixed in the material, the full set of six measurements on three different samples is necessary in general to unambiguously determine selection rules of the observed modes. Examples of such polarization comparison for terbium manganite are given in Figs. 1.5 and 7.3.

The complex transmission coefficient $t = |t|e^{i\varphi}$ can be constructed from two real values of transmission coefficient $|t|$ and phase shift φ . Expression (3.2) contains two complex parameters $\varepsilon = \varepsilon_1 + i\varepsilon_2$ and $\mu = \mu_1 + i\mu_2$, which are equivalent to four real variables. Therefore, the complex transmission is generally not enough to determine optical parameters of the sample. However, magnetic response is limited to the narrow absorption modes of ferromagnetic or antiferromagnetic resonances at THz frequencies. Outside these resonances magnetic susceptibility is negligible, and $\mu = 1$ with a good accuracy. In this case the formula (3.2) can be either used to fit experimental spectra, or can be viewed as a system of two equations in two variables ε_1 and ε_2 in order to obtain the permittivity of the sample directly. If a magnetic response is present in the sample, it can be well described in most cases by a Lorentz-shaped absorption mode in μ :

$$\mu(\omega) = 1 + \frac{\Delta\mu\omega_0^2}{\omega_0^2 - \omega^2 - 2i\omega\gamma}$$

Here, $\Delta\mu$ is the strength of the resonance, ω_0 is the resonance frequency and γ is a half-width of the resonance. A direct fit of transmission and phase spectra is used then to obtain both magnetic and dielectric properties of the material.

An example of the transmission spectrum together with the fit is shown in Fig. 3.3. The frequency in this and all other figures in the thesis is represented in the reciprocal wavelength $\lambda^{-1} = \omega/(2\pi c)$. Such units are directly proportional to the frequency ω and are common in the infrared spectroscopy. Comparing with other common frequency and energy units, $10 \text{ cm}^{-1} = 300 \text{ GHz} = 1.24 \text{ meV} = 14.4 \text{ K}$. The oscillations in the spectrum are caused by multiple reflections on the sample surfaces. The sample can be viewed as a Fabry-Pérot resonator with a low quality factor. The condition of the transmission maximum is that an integer number of wavelengths should fit into the double optical thickness of the sample: $2nd = m\lambda$. The experimental oscillations are well fitted by formula (3.2) allowing to reliably determine the refractive index $n \approx \sqrt{\varepsilon_1} = 3.77$

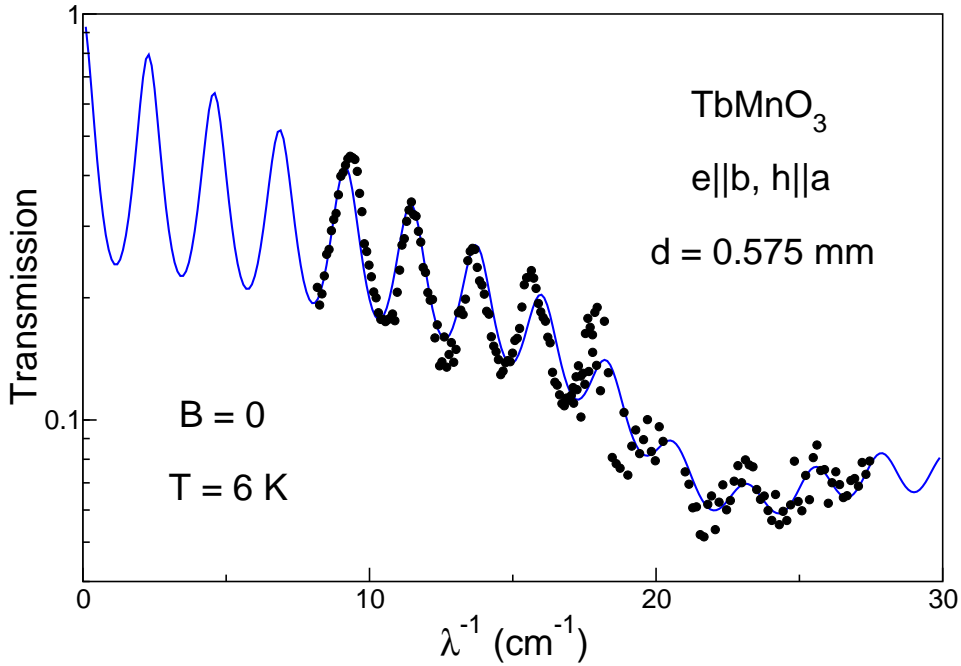


Figure 3.3: Example of a transmission spectrum of TbMnO_3 with electric field along the b axis and magnetic field along the a axis. Symbols represent experimental data, solid line is a fit with a constant $\varepsilon = 14.18 + i0.53$ and Lorentzian in μ . Parameters of the magnetic mode are $\Delta\mu = 0.01$, $\omega_0 = 22.36 \text{ cm}^{-1}$ and $\gamma = 4.61 \text{ cm}^{-1}$. The oscillations in the spectrum are due to Fabry-Pérot interferences, caused by multiple reflections on the sample surfaces.

from the transmission spectrum. The phase spectrum is not needed in this case. The slow decrease of the transmission with the frequency is well described by the constant imaginary part of permittivity $\varepsilon_2 = 0.53$. The broad minimum of the transmission at 23 cm^{-1} is caused by the phason, which is excited magnetically ($h||a$) in this polarization (see Fig. 2.17 and explanations in the text for the details). The parameters of the resonance obtained from the fit are $\Delta\mu = 0.01$, $\omega_0 = 22.4 \text{ cm}^{-1}$ and $\gamma = 4.6 \text{ cm}^{-1}$.

3.3 Sample characterization

The samples of rare earth manganites RMnO_3 were synthesized by a floating zone method at the Moscow Power Engineering Institute [56]. The powders of Mn_2O_3 and R_2O_3 were milled, mixed and preliminary annealed at temperatures around 1300°C . The obtained substances were then milled again and pressed into the bars. The density of the bars after the subsequent heat treatment at 1400°C was about 80% of the theoretical value. The floating zone growth was performed in an apparatus with a radiation heating in Ar flow. The grown crystal rod was kept in the in-process annealing furnace at 1400°C during the growth and was cooled down at a rate of $200^\circ\text{C}/\text{h}$ afterwards.

The samples for the spectroscopic measurements were cut in the form of thin plates. Two crystallographic axes always lie in the plane of the plate and the third is normal

to the plate. The samples are often designated by this third crystallographic axis. For example, “*a*-cut” sample has *a* axis normal to the largest surface, and *b* and *c* axes lie in the plane of the sample. Three different “cuts” are enough to obtain all six possible experimental geometries required for the polarization analysis of the excitation conditions.

X-ray diffraction experiments were performed on the powder of the crushed single crystals at room temperature. No impurity phases were detected for all compositions concerned in the present work. The Rietveld refinement of the diffraction data was performed for GdMnO_3 [57] and $\text{Eu}_{1-x}\text{Y}_x\text{MnO}_3$ [24] manganites. The obtained lattice parameters and Mn-O-Mn bond angle ϕ were in a good agreement with the literature data [23]. The single crystal X-ray diffraction measurements were performed on DyMnO_3 samples at the X-ray center of the Vienna University of Technology. The orientations of all three crystallographic axes were easily determined and the samples have shown good crystalline quality. Extensive magnetic susceptibility and specific heat measurements performed on GdMnO_3 and $\text{Eu}_{1-x}\text{Y}_x\text{MnO}_3$ compounds have allowed to construct detailed magnetic phase diagrams [24, 57]. The transition temperatures from these diagrams agree well with the data from the low frequency [24] and high frequency (see below) dielectric measurements.

The optical data, described in the next chapters, also provide a characterization of the samples at THz frequencies. The observation of three distinct values of dielectric permittivity ε_a , ε_b and ε_c along the principal axes is an indication of the overall good quality of single crystals. The transitions between different magnetically ordered phases are often seen in the temperature scans of the permittivity and provide the high frequency data for the construction of the phase diagrams. A well-defined separation of the excitation conditions in different polarizations is another evidence that the crystals are not twinned and maintain the long range order across the whole size of the samples.

4 GdMnO₃: introducing an electromagnon

Electromagnons, strong electric-dipole active excitations with a typical energy of a few meV, were originally detected in GdMnO₃ [16]. Such features like very strong and broad absorption peak of THz radiation already distinguished them from the magnons, or spin waves. Magnons are spectroscopically observed at $q = 0$ and also called antiferromagnetic resonances (AFMR). The polarization analysis has confirmed this assumption unambiguously showing the excitation condition $e \parallel a$, i.e. the mode is seen for the electric field of incident radiation parallel to the crystallographic a axis only. Additional experiments [58] have identified the source of the spectral weight of electromagnons. These novel excitations mostly couple to the lowest lying phonon, although the coupling to other phonons probably also exists. Finally, “high frequency electromagnon”, the excitation at 75 cm^{-1} which is outside of the range of THz spectrometer was investigated in Ref. [59] using far-infrared transmission technique. The whole set of these experimental findings makes GdMnO₃ one of the best candidates to introduce the general properties of electromagnons and will be presented in this chapter.

4.1 Zero field THz and FIR spectra

The high-temperature paramagnetic phase in GdMnO₃ is followed by an incommensurate antiferromagnetic phase below $T_N = 42 \text{ K}$ ($B = 0$ path in the phase diagram in Fig. 4.3). This phase is characterized by a sinusoidally modulated spin structure of the manganese spins, with the Gd spins still remaining paramagnetic [57]. In low fields ($B < 0.1 \text{ T}$) and under zero-field cooling conditions the incommensurate structure remains the stable phase down to 8 K and is followed by a complex canted ferrimagnetic structure of Gd and Mn spins. In finite magnetic fields along the c axis ($B > 0.1 \text{ T}$) the incommensurate phase is transformed to a canted antiferromagnetic state with the ferromagnetic c axis components of the manganese and gadolinium spins oriented antiparallel. Details of this structure are unknown, but it is clear that in this phase the Gd spins participate in the magnetic order. Between $8 < T < 17 \text{ K}$ this spin arrangement strongly competes with the incommensurate ordering and depending on the magnetic history the canted antiferromagnet can be stabilized even in zero external magnetic fields.

Ferroelectric polarization along the a axis with the strength comparable to other rare earth manganites arises only in magnetic fields $B \parallel b$ [20]. However, small spontaneous polarization $P \parallel a$ still exists in zero magnetic fields above Gd ordering temperature. As

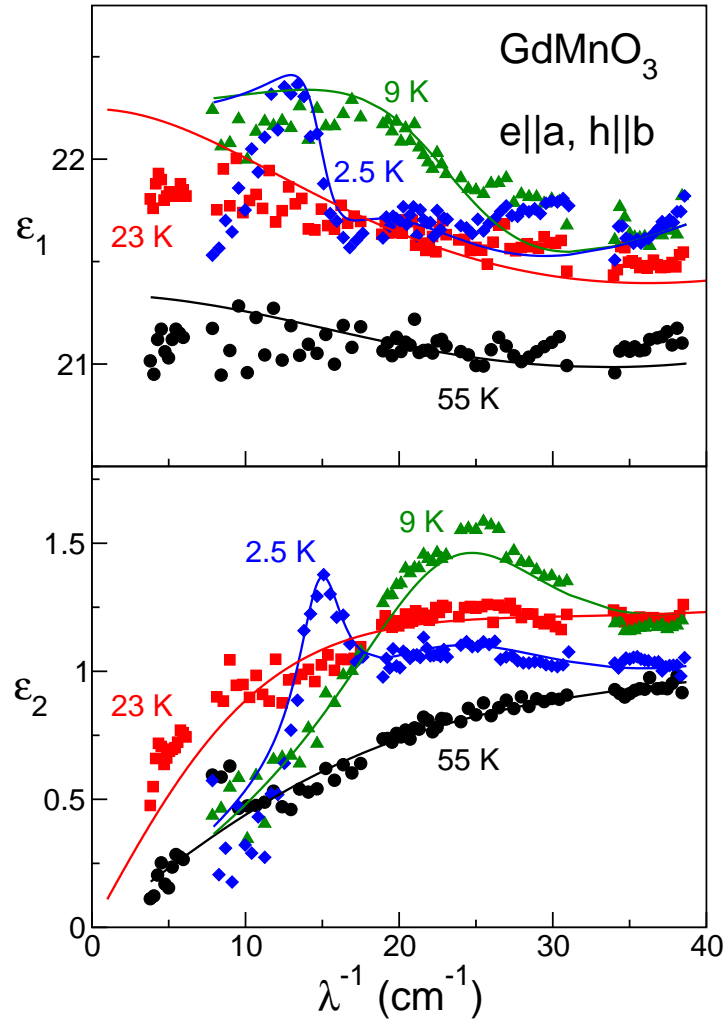


Figure 4.1: Terahertz dielectric spectra of GdMnO_3 along the a axis. Upper panel - real part, lower panel - imaginary part. Symbols - experiments, lines - fits using the sum of Lorentzians. The spectra are representative for the paramagnetic phase (55 K), incommensurate sinusoidal phase (23 and 9 K) and for the phase with Gd ordering (2.5 K).

the ferroelectricity disappears in the Gd-ordered phase the care must be taken not to cross the transition temperature during the polling of the sample in the external electric field [20]. The weakness of the polarization in GdMnO_3 is easy to understand taking into account that this compound is located at the boundary between A -type and cycloidal spin ordering in the Mn-O-Mn bond angle phase diagram in the Fig. 1.11. Cycloidal structure is heavily suppressed by the competing A -type ordering and needs assistance in the form of external magnetic fields $B \parallel b$ to become stable ground state.

Figure 4.1 shows terahertz spectra of GdMnO_3 for the electric field parallel to the a axis and at different temperatures. The data have been obtained with the ac magnetic field parallel to the b axis. This geometry has no contribution from the antiferromagnetic resonance seen at 21 cm^{-1} for $h \parallel c$ and the pure dielectric response can be presented. A

broad relaxation-like contribution can be observed already in the paramagnetic phase at $T = 55$ K (black circles and lines in the lower panel of Fig. 4.1). Although the sample is not magnetically ordered, this absorption plateau can be probably due to magnetoelectric fluctuations in the vicinity of transition temperature at $T_N = 42$ K. This over-damped excitation grows in the sinusoidal phase and increases the low frequency dielectric constant (red squares and lines in lower and upper panels of Fig. 4.1). It is this broad excitation that has been called *electromagnon* [16]. Its over-damped character in sinusoidal incommensurate phase is typical for other orthorhombic rare earth manganites like $\text{Eu}_{1-x}\text{Y}_x\text{MnO}_3$, DyMnO_3 and TbMnO_3 . Substantial narrowing of the electromagnon is observed below 20 K allowing to determine its characteristic frequency of 25 cm^{-1} (green triangles and lines in Fig. 4.1). This narrowing is associated with the transition to the cycloidal spin structure and the onset of ferroelectric polarization in other manganites. The same mechanism is applicable to GdMnO_3 , according to the refined data in Ref. [20]. The polarization analysis similar to TbMnO_3 was also done for GdMnO_3 and has confirmed the $e\parallel a$ excitation condition. Thus, the electromagnon is an excitation of magnetic origin stemming from the particular spin order and it gains its electroactivity through the magnetoelectric interaction.

The dielectric strength of the electromagnon decreases below the temperature of the Gd ordering. The intensity of the electromagnon at 25 cm^{-1} decreases and instead an additional narrow peak appears at 15 cm^{-1} . This peak is most clearly seen in $T = 2.5$ K spectra (blue diamonds and lines in Fig. 4.1) but can be detected at $T = 5$ K as well. This splitting reflects the fine structure of the electromagnon and is observed in TbMnO_3 as well (see Chapter 7).

Apart from the “low frequency electromagnon” described above there is another excitation in GdMnO_3 at 75 cm^{-1} , the so called “high frequency electromagnon”. As its frequency is outside the range of THz spectrometer, the far infrared Fourier-Transform spectroscopy was used to obtain data in this frequency range. In order to obtain the complex permittivity both reflectance and transmittance had to be measured. The reflectivity was obtained on an optically thick sample with negligible contribution from the second surface [58]. The crystal was then polished down to $220 \mu\text{m}$ for the transmittance measurements [59]. The obtained spectra have been transformed to the dielectric permittivity by inverting the Fresnel optical equations for transmittance and reflectivity which neglect the interferences within the sample. These interferences are seen as a Fabry-Pérot type modulation and are the reason for the apparent data scattering at room temperature and between 20 cm^{-1} and 60 cm^{-1} . An attempt to take into account the interferences did not improve the quality of the solution probably because of imperfections of the sample surface. Figure 4.2 represent the far-infrared spectra of the dielectric permittivity of GdMnO_3 in the frequency range relevant for electromagnons. The results by the infrared transmittance rapidly loose the accuracy below 40 cm^{-1} . Therefore, in this frequency range the data by BWO spectroscopy from Figure 4.1 are plotted as closed symbols.

The strong and narrow mode at 120 cm^{-1} in Fig. 4.2 is the lowest phonon. Its hardening at low temperatures is a well known manifestation of anharmonicity. Another important parameter of the phonon mode, its dielectric strength is not readily seen in

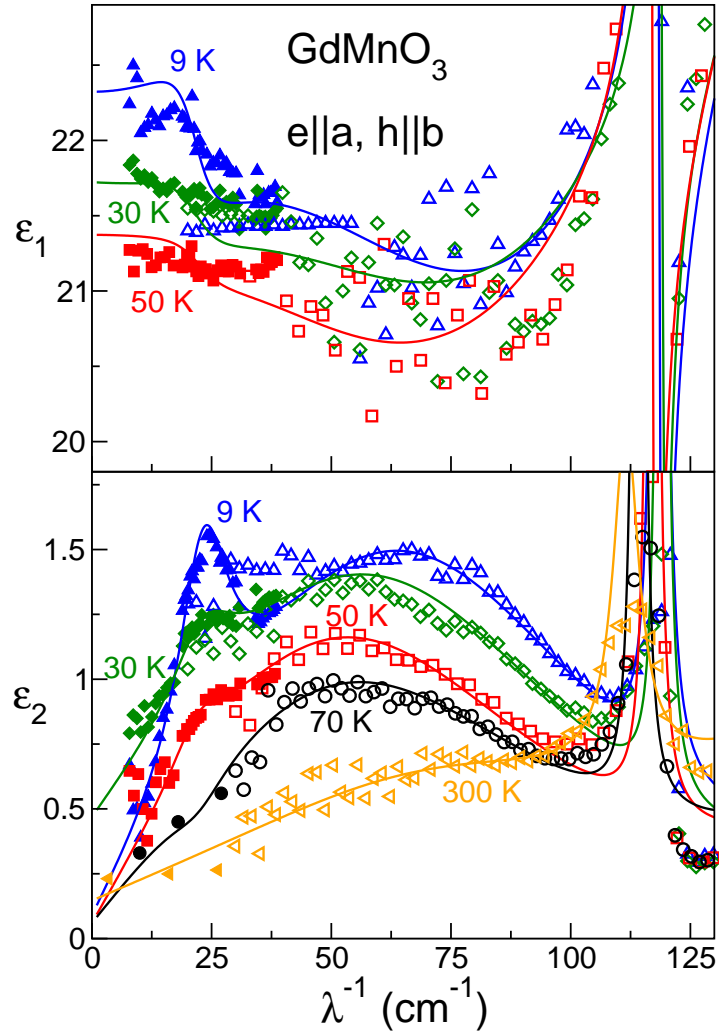


Figure 4.2: Complex dielectric permittivity of GdMnO_3 in the far-infrared frequency range. Open symbols - experimental data obtained from transmittance and reflectance spectra [59], closed symbols - data obtained from the complex transmission coefficient [16, 60], solid lines - model based on a sum of Lorentzians.

the current representation and will be discussed later in the context of interplay with electromagnons. The low frequency electromagnon located at 25 cm^{-1} is most easily detected at the lowest presented temperature $T = 9 \text{ K}$ in the imaginary part of the dielectric permittivity (blue upper triangles and lines in the lower panel of Fig. 4.2). A very broad absorption in the frequency range between lower electromagnon and up to the phonon is the high frequency electromagnon. This excitation, like the low frequency electromagnon, increases its strength upon cooling from $T = 50 \text{ K}$ (red squares) into the sinusoidally modulated antiferromagnetic phase (green diamonds) and further down to the cycloidal phase (blue triangles in Fig. 4.2). One of the still puzzling features of the high frequency electromagnon is the nonvanishing contribution deep in the paramagnetic state ($T = 70 \text{ K}$, black circles and lines). The residual absorption plateau survives even

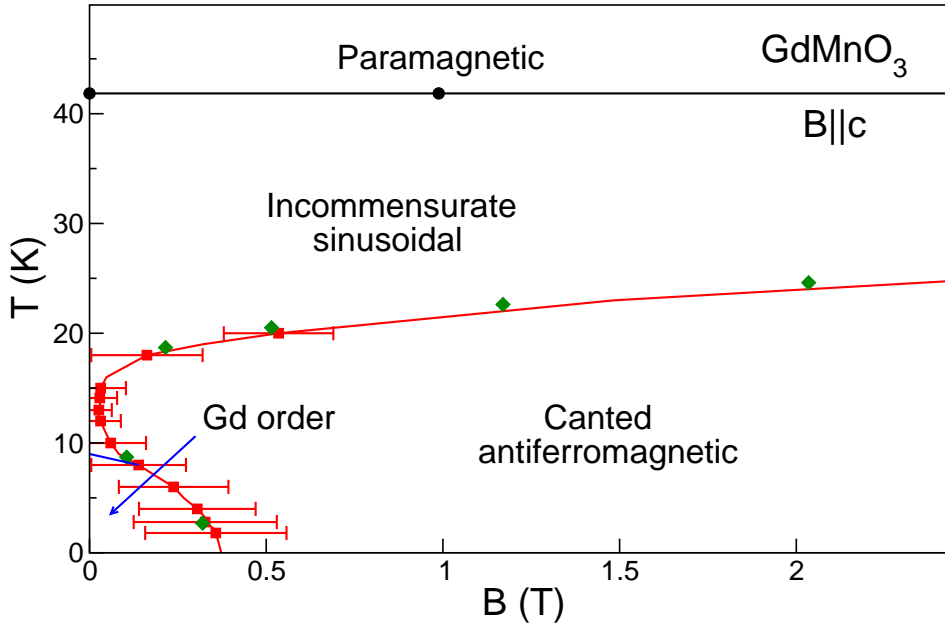


Figure 4.3: Magnetic phases in GdMnO_3 and external magnetic fields $B \parallel c$ [20, 58]. Black circles and red squares were obtained from the magnetization measurements, green diamonds are from dielectric experiments. The region of weak ferroelectricity in zero magnetic fields between $T = 23$ K and down to the Gd ordering temperature observed in Ref. [20] is not shown, and is probably sample dependent.

at room temperatures (orange left triangles and lines in Fig. 4.2). Such temperature evolution of the high frequency electromagnon is hard to explain by thermal fluctuations only and remains an open question.

Although the trace of the phonon at 120 cm^{-1} is clearly seen in the spectra of the ε_1 (upper panel), only the low frequency electromagnon can be detected there. The reason of this effect is small dielectric contribution ($\Delta\varepsilon \sim 0.5$) of the electromagnons compared to the contributions of the phonons ($\sum \Delta\varepsilon_i \sim 10$). A very broad nature of the high frequency electromagnon with a damping $\gamma = 125 \text{ cm}^{-1}$ smears out effects in the real part of dielectric constant. It is also the reason for the shift of the maximum of ε_2 towards lower frequencies in the lower panel of Fig. 4.2. The dielectric spectra in the far-infrared frequency range were fitted using the sum of several Lorentzians and represented in Fig. 4.2 by the solid lines. The parameters of electromagnons obtained from these fits can be found in Ref. [59]. However an external factor different from temperature appeared to be more convenient to control the emergence of electromagnons – an external magnetic field along the crystallographic c axis. The main findings of these experiments will be presented in the next section.

4.2 Coupling of phonons and electromagnons

A detailed H - T phase diagram of GdMnO_3 for magnetic fields $B \parallel c$, obtained using dielectric [16] and magnetic [20] data, is shown in Fig. 4.3. An external magnetic field

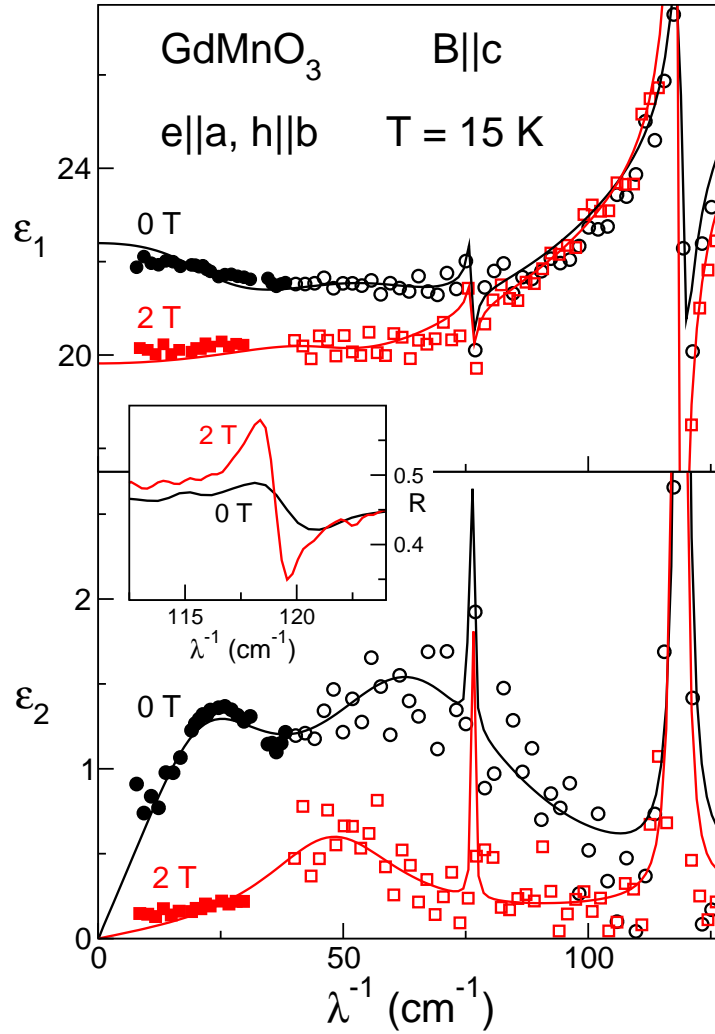


Figure 4.4: Spectra of the a axis dielectric permittivity of $GdMnO_3$ at $B = 0$ T (incommensurate sinusoidal state) and $B = 2$ T (canted antiferromagnetic state). Upper panel: real part of the dielectric permittivity, lower panel: imaginary part. Closed symbols - terahertz experiments, open symbols - infrared spectroscopy. Solid lines are fits accounting for electromagnons and phonons. The narrow line at 76 cm^{-1} is probably due to impurity. The inset shows reflectance spectra around the phonon at 120 cm^{-1} .

favours the canted antiferromagnetic phase where no electromagnons can be observed. This phase competes with the incommensurate sinusoidal ordering and simple removal of external field does not bring the sample back to the original state. The heating up to $T = 17$ K is needed to restore the sinusoidal spin structure. Very low critical fields $B \sim 0.2$ T of this magnetic phase transition at temperatures around 15 K provide very convenient method to suppress electromagnons. It is easy then to detect spectroscopical changes associated with this transition without interference from other effects which may arise in high magnetic fields.

Basic result of experiments [58] performed in magnetic fields $B||c$ is shown in Fig. 4.4. The complex dielectric permittivity above 40 cm^{-1} was obtained via Kramers-Kronig

relation. Augmenting Fourier-Transform reflectivity with the THz data has increased the accuracy of the procedure. Closed symbols in Fig. 4.4 are direct measurements at THz frequencies while open symbols are based on the far-infrared reflectance. The temperature of $T = 15$ K is chosen as having the lowest critical magnetic field. Therefore the data at $B = 0$ T (black symbols and lines) represents sinusoidal phase and the measurements done at $B = 2$ T (red symbols and lines) are deep in the canted antiferromagnetic phase (see Fig. 4.3). The most prominent effect seen both in ε_2 (lower panel in Fig. 4.4) and ε_1 (upper panel) is the suppression of electromagnon in the canted phase. This is a strong evidence that although the electromagnon is seen as an *electric* excitation, it has *magnetic* origin. The numerous experiments and attempts to describe electromagnons theoretically have shown that low and high frequency electromagnons can have different microscopical origins. Some evidence can be seen in Fig. 4.4 too. The low frequency electromagnon at 25 cm^{-1} is suppressed completely, but some absorption maximum at 50 cm^{-1} , closer to the high frequency electromagnon still exists in the canted phase.

The second effect of the magnetic phase transition is better seen not in the dielectric permittivity but instead directly in the reflectance spectra. A small frequency range around a phonon at 120 cm^{-1} is represented in the inset in Fig. 4.4. The phonon feature in the reflectance spectra is considerably increased in the canted antiferromagnetic phase. As this feature is directly related to the strength of the phonon it is clear that the phonon gains in intensity upon suppression of the electromagnon. The above findings have allowed to draw another important conclusion concerning spectroscopical origin of electromagnons: they gain their spectral weights mostly from the lowest phonons. The quantitative investigations [58, 59, 60] have shown that other phonons are involved too, although to the lesser extent.

Although the microscopic origin of the high frequency electromagnon has settled on the symmetric Heisenberg exchange model [40], the prediction of the earlier model [38] based on the antisymmetric Dzyaloshinskii-Moriya interaction is still quite informative. For the dynamic properties the main result of these calculations is the occurrence of two modes, one of which is derived from the phonon mode with a frequency close to the eigenfrequency of the uncoupled phonon, and one originating from the spin wave. The theory predicts the enhancement of the phonon eigenfrequency ω_0 by $\omega_p^2/(2\omega_0)$, where ω_p is the frequency of the electromagnon. Taking $\omega_p \sim 20 \text{ cm}^{-1}$, based on the low frequency electromagnon, the phonon shift observed across magnetic phase transition [58] can be well explained.

4.3 Summary

GdMnO₃ together with TbMnO₃ were pioneering systems to reveal electromagnons [16]. The key experiments to confirm the electric excitation of electromagnons and their coupling with the phonons were done on GdMnO₃ samples. However gadolinium manganite also has its drawbacks. The first is its position in the Mn-O-Mn bond angle phase diagram Fig. 1.11. It is located at the boundary between *A*-type antiferromagnetic and cycloidal orderings at low temperatures. This makes the most interesting cycloidal

phase metastable at best and reliably available in the external magnetic fields $B\parallel b$ only. Another feature of GdMnO_3 is the existence of strong and anisotropic magnetism of Gd^{3+} ions. This not only leads to the complicated magnetic phase diagram at low temperatures (Fig. 4.3), but also poses a question about the role of rare earth ion in the formation of the cycloidal spin order. Natural mixture of Gd isotopes has very large absorption coefficient for thermal neutrons, over 1000 cm^{-1} in the case of GdMnO_3 for neutron wavelength in the range of $2 - 5\text{ \AA}$ [61]. This makes neutron scattering experiments impossible, at least on the natural isotopic mixture, and closes this experimental possibility to determine the magnetic structure and the magnon dispersions. In fact all magnetic phase assignments in the present chapter are made on the basis of magnetization data and in analogy to another rare earth manganite with known magnetic structure - TbMnO_3 . The aspects of this multiferroic material are postponed for later while the next chapter concerns with the series of $\text{Eu}_{1-x}\text{Y}_x\text{MnO}_3$ - manganite without rare earth magnetism.

5 $\text{Eu}_{1-x}\text{Y}_x\text{MnO}_3$: manganese *vs.* rare earth

A common property of Gd, Dy and Tb-manganites, which are concerned in the present work is the existence of two competing magnetic sublattices, of Mn and of the rare earth. It was not quite clear what is the role of the rare earth subsystem in the magnetoelectric interaction. In order to separate the role of the rare earth from the magnetoelectric effects in manganites it was expedient to repeat the experiments on manganites without rare earth magnetism. Such a system is provided by $\text{Eu}_{1-x}\text{Y}_x\text{MnO}_3$. The electronic configuration of the trivalent *A*-sites in this compound are either nonmagnetic ($[\text{Kr}]$) for Y^{3+} ions, or possess only Van Vleck paramagnetism ($4f^6$) with $J = 0$ for Eu^{3+} ions. Doping by yttrium is here a tuning parameter which allows to gradually change the Mn-O-Mn bonding angle. From the point of view of multiferroic properties, it makes $\text{Eu}_{0.2}\text{Y}_{0.8}\text{MnO}_3$ equivalent to GdMnO_3 and $\text{Eu}_{0.5}\text{Y}_{0.5}\text{MnO}_3$ to TbMnO_3 . Most of the results presented in this chapter were obtained previously in [24, 30] and further refined in [62]. These findings however are quite important for the understanding of the underlying mechanisms which lead to the formation of electromagnons. Experimental data for $\text{Eu}_{1-x}\text{Y}_x\text{MnO}_3$ with the main focus on THz excitations are briefly summarized below.

5.1 Multiferroic phases of $\text{Eu}_{1-x}\text{Y}_x\text{MnO}_3$

Detailed investigation of magnetic and dielectric properties of $\text{Eu}_{1-x}\text{Y}_x\text{MnO}_3$ have been published in [24]. From these data a magnetic and electric phase diagram has been constructed which is reproduced in Fig. 5.1. In the doping range $0 \leq x \leq 0.5$ $\text{Eu}_{1-x}\text{Y}_x\text{MnO}_3$ orders antiferromagnetically between 45 K and 50 K only slightly depending upon the yttrium content. The antiferromagnetic order is incommensurate and probably sinusoidally modulated similar to other rare earth multiferroics. On further cooling another magnetic transition takes place. Depending on the doping range, this low-temperature phase is either canted antiferromagnetic (*A*-type) for $x < 0.2$ or spiral and ferroelectric for $x \geq 0.2$. For $x \approx 0.2$ the spatial phase separation of both phases was observed [62], with the possibility to tune their fractions by applying a static magnetic field during cooling. Compounds with high yttrium content $x > 0.5$ are hard to grow in the orthorhombic phase and they often include impurities of hexagonal phase of YMnO_3 . For this reason they are difficult to investigate in detail [63].

Terahertz properties of $\text{Eu}_{1-x}\text{Y}_x\text{MnO}_3$ have been published in [30]. From the point of view of the magnetoelectric effect and the observation of electromagnons, the phase

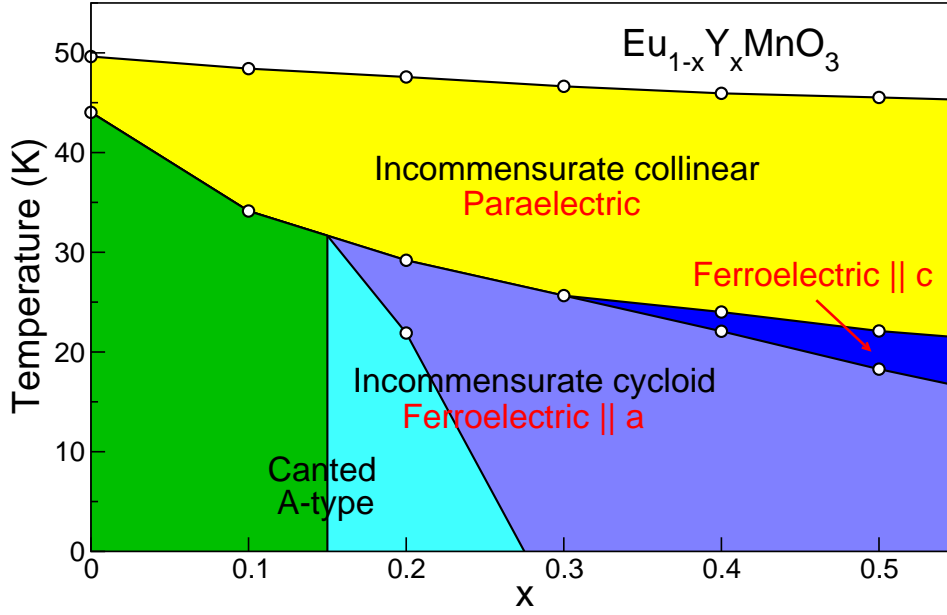


Figure 5.1: (T,x) phase diagram of $\text{Eu}_{1-x}\text{Y}_x\text{MnO}_3$ reproduced from [30]. The notation of magnetic phases is given on the basis of magnetization data. Incommensurate collinear and cycloidal phases are antiferromagnetic while canted A-type is weakly ferromagnetic. Two ferroelectric phases differ by the orientation of the spontaneous electric polarization. The exact magnetic structure of different phases is still unknown and is indicated in analogy to other perovskite multiferroics.

diagram in Fig. 5.1 can be divided into five regions:

1. In the whole doping range $0 \leq x \leq 0.5$ the paramagnetic and paraelectric phase above $T \sim 50$ K is followed by the incommensurate antiferromagnetic phase with possibly collinear sinusoidally modulated ordering of Mn spins. This phase does not show any electric ordering and only weak magnetoelectric effects are observed. The electromagnons are over-damped and not well defined.
2. In the low-doping range $0 \leq x \leq 0.1$ the collinear phase is followed by the canted antiferromagnetic phase which is weakly ferromagnetic and shows no magnetoelectric effect and no electromagnons are observed.
3. At low temperatures the phase around $x = 0.2$ is characterized by a spatially separated coexistence of both canted and cycloidal antiferromagnetic structures. The cycloidal phase is characterized by spontaneous electric polarization along a axis and the electromagnons are clearly observed in the spectra. External magnetic fields suppress the cycloidal phase in favour of canted weakly ferromagnetic ground state, which leads to strong magnetic field dependence of the dielectric permittivity.
4. For $0.3 \leq x \leq 0.5$ and at low temperatures the ferroelectric phase is not sensitive to external magnetic fields $B \parallel c$ up to 7 T. The electromagnons are strong and well defined in this region of the phase diagram.

5. In the region $0.4 \leq x \leq 0.5$ and within a narrow temperature range just below collinear phase there are two ferroelectric phases with electric polarization parallel to the a and c axes which compete with each other. This leads to the weak dependence of dielectric permittivity upon external magnetic fields.

In the next sections two examples of lower frequencies (below 40 cm^{-1}) magnetoelectric excitations in these compounds with their temperature and magnetic field dependencies for representative doping levels will be presented. As is the case for other rare earth manganites like GdMnO_3 , DyMnO_3 and TbMnO_3 , high frequency electromagnon also exists in the doping range $0.2 \leq x \leq 0.5$. Its frequency drops from 80 cm^{-1} for $x = 0.2$ [64] to 55 cm^{-1} for $x = 0.45$ [65].

5.2 Canted antiferromagnetic phase: $x = 0.1$

As an example of magnetoelectric excitations at low doping, Fig. 5.2 shows the terahertz spectra of $\text{Eu}_{0.9}\text{Y}_{0.1}\text{MnO}_3$ in geometry with $e \parallel a$. Here the data at 40 K and at 20 K are representative for the properties in the incommensurate collinear and canted antiferromagnetic phases, respectively. In a collinear phase at $T = 40 \text{ K}$ a broad absorption with a weak frequency dependence can be observed (red symbols in a lower panel of Fig. 5.2). This dissipative plateau corresponds to a weakly dispersive refractive index represented as red symbols in the upper panel of Fig. 5.2. Consistent with other manganites with frustrated magnetic order at low temperatures, this typical feature of the sinusoidal phase is the electromagnon seen as a broad Debye-like relaxation. The experimental spectra in the collinear phase can be well fitted by a Debye relaxator. Typical relaxation frequency of this excitation estimated from the fit (red lines in Fig. 5.2) is 10 cm^{-1} which corresponds to the inverse lifetime rather than to eigenfrequency in this case. Contrary to other manganites however, the electromagnon does not evolve into a well defined excitation in $\text{Eu}_{0.9}\text{Y}_{0.1}\text{MnO}_3$ at low temperatures. Instead the system orders antiferromagnetically with slight canting below 34 K and shows no electromagnons. This can be well seen as a substantial reduction in both absorption coefficient and refractive index (black symbols in Fig. 5.2). The narrow mode observed in the spectra is the antiferromagnetic resonance of the canted spin structure with $h \parallel c$ excitation condition [66]. Due to the magnetic nature of this mode the spectra are represented in terms of complex index of refraction $n + i\kappa = \sqrt{\varepsilon\mu}$. This antiferromagnetic resonance can be well fitted by a magnetic Lorentzian with an eigenfrequency of 19 cm^{-1} (black lines in Fig. 5.2).

The magnetoelectric contribution to the dielectric permittivity in $\text{Eu}_{0.9}\text{Y}_{0.1}\text{MnO}_3$ can be suppressed in external magnetic fields which favours the canted magnetic phase. An example of such behaviour is well seen in the magnetic field dependencies of permittivity in the temperature range of the phase transition and is shown in Fig. 5.3. Following the evolution of curves at $B = 0$ the phase transition from the higher absorptive collinear state at higher temperatures to the lower absorptive canted phase at lower temperatures is evident at $T = 34 \text{ K}$. As external magnetic fields stabilize the canted phase, no changes in the permittivity are expected below the transition temperature (black and red curves

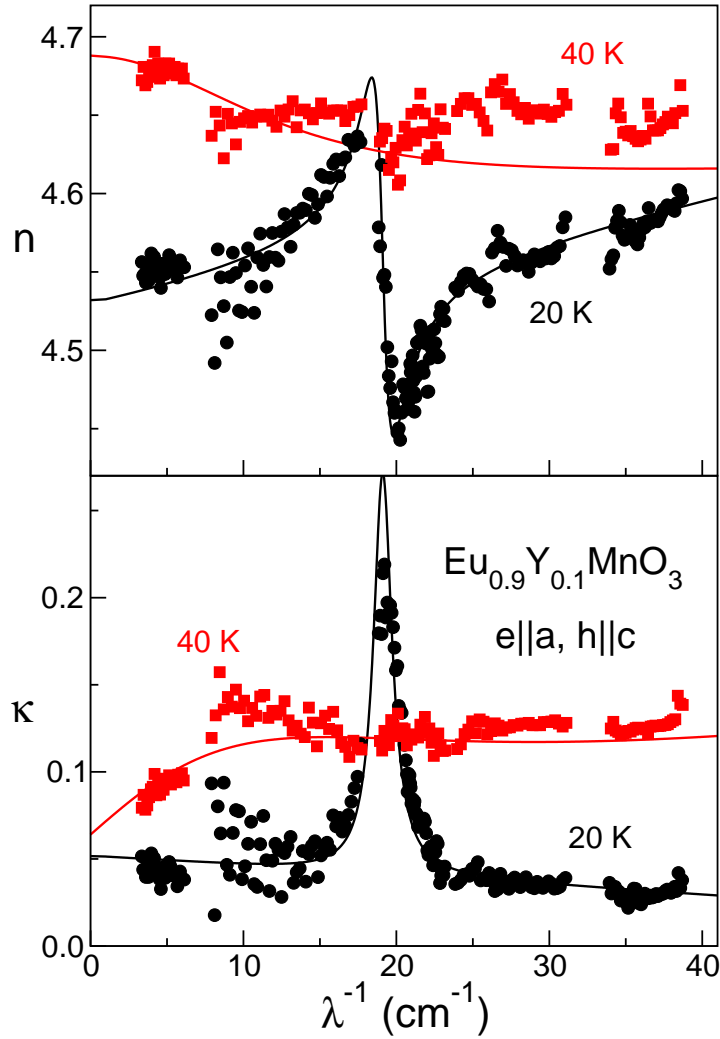


Figure 5.2: Terahertz spectra of $\text{Eu}_{0.9}\text{Y}_{0.1}\text{MnO}_3$ in the collinear (40 K) and canted (20 K) antiferromagnetic phases [30]. Upper panel - refractive index, lower panel - absorption coefficient. The narrow mode at $\lambda^{-1} \simeq 19 \text{ cm}^{-1}$ represents the antiferromagnetic resonance ($h||c$). The broad additional absorption for $T = 40 \text{ K}$ is of magnetoelectric origin. Symbols represent the experimental data, lines show the fits using the sum of Lorentzians and a Debye relaxator.

in the Fig. 5.3). On the other hand, initially in the collinear phase, the sample undergoes a transition into the canted phase at gradually increasing magnetic fields depending on temperature (green, blue and orange curves in the Fig. 5.3). According to the data, the transition temperature increases up to $T = 40 \text{ K}$ at $B = 5 \text{ T}$.

In the view of the Mn-O-Mn bond angle phase diagram Fig. 1.11 $\text{Eu}_{0.9}\text{Y}_{0.1}\text{MnO}_3$ lies to left of GdMnO_3 outside of the boundary to cycloidal antiferromagnetic orderings and in accordance with its ground state. It is noticeable however, that the electromagnon contributions in the form of the overdamped relaxations are already present in the intermediate temperature range. Their existence points to the onset of the spin frustration in the system and is possibly explained by a short range cycloidal order due to thermal

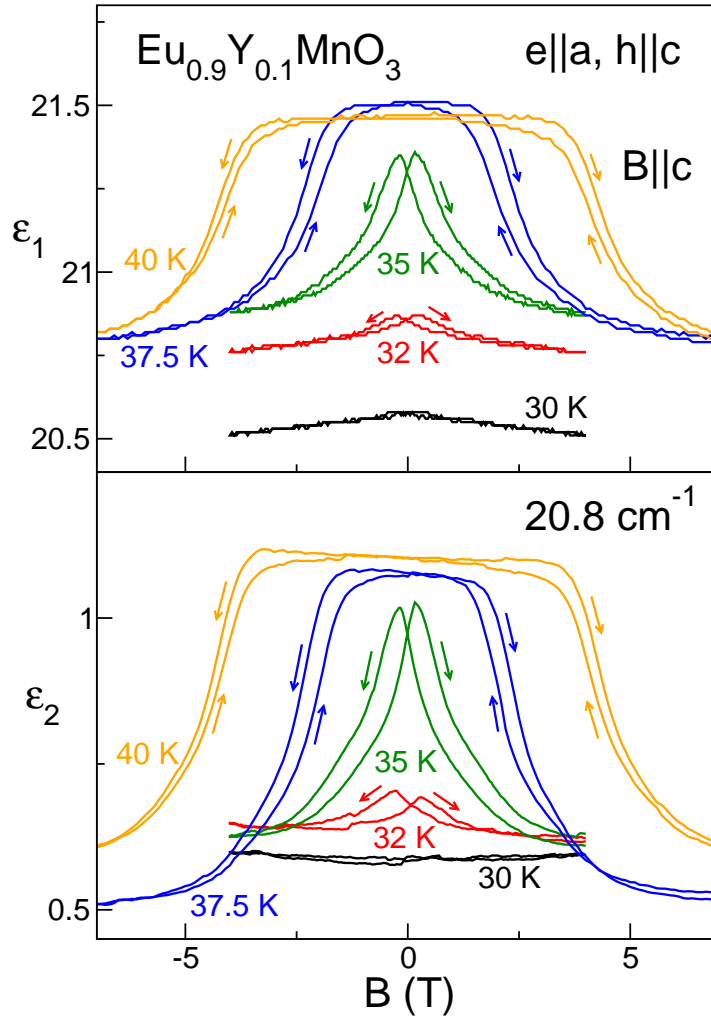


Figure 5.3: Magnetic field dependence of the complex dielectric constant $\varepsilon = \varepsilon_1 + i\varepsilon_2$ on the border between collinear and canted antiferromagnetic phases. Zero field transition takes place at $T = 34$ K and is shifted up to $T = 40$ K at $B = 5$ T.

fluctuations.

5.3 Cycloidal antiferromagnetic phase: $x = 0.5$

In the high yttrium doping regime of $\text{Eu}_{1-x}\text{Y}_x\text{MnO}_3$, the electromagnons at low temperatures are seen as narrow well defined excitations with substantial spectral weight. Consistent with other spin frustrated orthorhombic manganites the electromagnons are observed for polarizations of THz radiation with $e||a$ only. Typical terahertz spectra in heavily doped composition $\text{Eu}_{0.5}\text{Y}_{0.5}\text{MnO}_3$ are represented in Fig. 5.4. The imaginary part of permittivity responsible for the absorption is shown in the lower panel while the real part of permittivity corresponding to the refractive index is in the upper panel. A flat background absorption plateau seen in paramagnetic phase (black circles

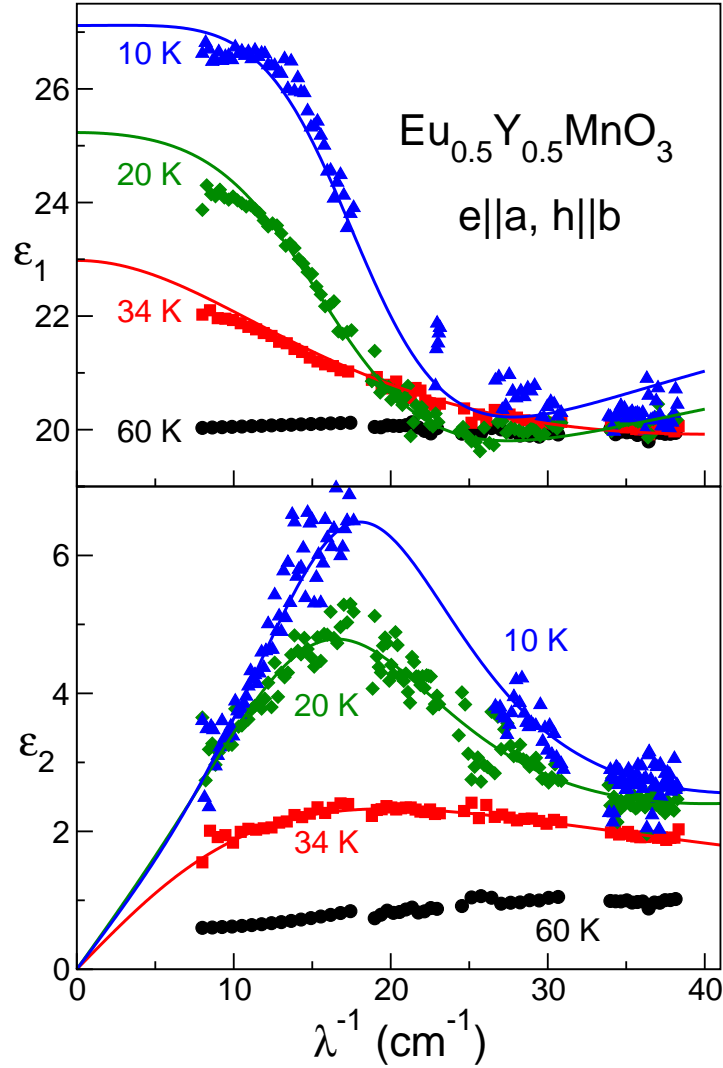


Figure 5.4: Spectra of the dielectric permittivity of $\text{Eu}_{0.5}\text{Y}_{0.5}\text{MnO}_3$ for $e||a$. Upper panel - real part, lower panel - imaginary part. Symbols - experiment, lines - Lorentzian fits. The temperatures shown are representative for paramagnetic phase (black colour, 60 K), collinear phase (red colour, 34 K) and ferroelectric phases with $P||c$ (green colour, 20 K) and $P||a$ (blue colour, 10 K).

in Fig. 5.4) transforms into a broad Debye-like contribution in the collinear phase (red squares). From the fits of this overdamped electromagnon (red lines) its damping frequency can be estimated as $\Gamma \sim 20 \text{ cm}^{-1}$. Upon further cooling of the sample into the ferroelectric phases the electromagnon narrows down and gains in intensity and spectral weight (green diamonds and blue triangles in Fig. 5.4). It can be well fitted by a Lorentzian mode with eigenfrequency of $\omega \sim 18 \text{ cm}^{-1}$. Such temperature evolution is typical for all other orthorhombic manganites concerned in the present work with two differences. The first one is the absence of magnetic ordering of the rare earth A -site ion at low temperatures. It is therefore obvious that the ferroelectricity and the emergence of electromagnons are due to the magnetism of Mn atoms and magnetic properties of

rare earth ions are not vital here. The second difference is another ferroelectric ground state $P\parallel a$ compared with GdMnO_3 , DyMnO_3 and TbMnO_3 which all exhibit $P\parallel c$ axis in zero magnetic field. The phase with $P\parallel c$ also exists in $\text{Eu}_{1-x}\text{Y}_x\text{MnO}_3$ in the narrow temperature range just below collinear phase (see phase diagram in Fig. 5.1). It can be completely suppressed by the external magnetic field $B\parallel c$ of around 5 T. According to the present theories the ferroelectricity in these compounds is caused by the particular inversion symmetry breaking cycloidal ordering of Mn spins. As such the direction of spontaneous electric polarization is bound to the orientation of spin cycloid. The later is dependent upon many factors as magnetic anisotropy and external magnetic fields. It is quite possible that the absence of the second magnetic subsystem in the form of strong magnetic rare earth ions in $\text{Eu}_{1-x}\text{Y}_x\text{MnO}_3$ is enough to favour another ground state of Mn spin cycloid.

Concerning the properties of $\text{Eu}_{1-x}\text{Y}_x\text{MnO}_3$ in the high doping range in external magnetic fields, no suppression of the electromagnons at low temperatures for magnetic fields up to 7 T along c axis can be observed. According to the Mn-O-Mn bond angle phase diagram (Fig. 1.11), the highly doped samples lie within the region of low temperature spin frustration. According to the structural analysis [24], the composition $\text{Eu}_{0.5}\text{Y}_{0.5}\text{MnO}_3$ should be located between GdMnO_3 and TbMnO_3 and the suppression of cycloidal ordering in moderate magnetic fields could be expected. The possible reason for the increased critical field along c axis might be the pinning on the disorder introduced by the yttrium doping.

The temperature range where the ferroelectric phase $P\parallel c$ exists can also be increased in external magnetic fields along the a axis. The magnetic phase transition occurs at $B = 4.5$ T and the phase with $P\parallel c$ is stabilized down to the lowest temperatures [67]. No change in structural, magnetic or electric properties was found for magnetic fields along the b axis. Such behaviour can be well explained assuming cycloidal ordering of Mn spins at low temperatures for $\text{Eu}_{1-x}\text{Y}_x\text{MnO}_3$ with high yttrium content. In the absence of external magnetic fields, the spins are located in the ab crystallographic plane and cause electric polarization $P\parallel a$ via inverse Dzyaloshinskii-Moriya interaction. Application of magnetic field $B\parallel c$ only stabilizes this structure as it can obtain some conical component along c axis and gain Zeeman energy. Consistently, the phase with the spin cycloid in the bc plane and electric polarization $P\parallel c$ is suppressed. On the other hand, an external magnetic field $B\parallel a$ favours bc orientation of the spin cycloid and results in a flop of electric polarization from $P\parallel a$ to $P\parallel c$ axis. The opposite picture in other orthorhombic manganites can be probably attributed to the complex interaction between Mn spins and rare earth $4f$ -moments.

5.4 Summary

Such favourable properties of $\text{Eu}_{1-x}\text{Y}_x\text{MnO}_3$ compounds as the absence of rare earth magnetism and the possibility to tune Mn-O-Mn bond angle via yttrium doping with weak, if any, effects of disorder have made these materials attractive for the research in many areas. Comparison of the electromagnons in the Eu:Y and Y:Lu systems was

performed in [63]. Ferroelectric phases in Eu:Y manganites were further investigated in the intermediate [68] and even strong pulsed [69] magnetic fields. The details of shifting of both infrared and Raman active phonons with the yttrium doping can be found in [70]. The effects of the spin-phonon coupling resulting in the shifts of some phonons below magnetic transition temperature were observed in [25, 71] and the comparison of these spin-phonon coupling effects in $\text{Eu}_{1-x}\text{Y}_x\text{MnO}_3$ and in pure manganites as Gd, Dy and TbMnO_3 is published in the work [72]. The spectral weight transfer from the lower lying phonon mode to the electromagnons, similar to that observed in GdMnO_3 and discussed in the previous chapter is reported in [65]. The quantitative analysis of the spectral weight including electromagnons and 8 lowest phonons was carried out in Ref. [64]. It was shown that the electromagnons are gaining their spectral weight not only from the lowest lying phonon, but from other phonons as well. Within experimental accuracy the total spectral weight is conserved. The comprehensive overview of spin-phonon and electromagnon-phonon couplings can be found in the thesis [73].

In the scope of this work the most important result in $\text{Eu}_{1-x}\text{Y}_x\text{MnO}_3$ is that magnetoelectric effects and electromagnons are observed in the full doping range $0 \leq x \leq 0.5$. This excludes the influence of the rare earth magnetism as a basic mechanism for the magnetoelectric effects in rare earth multiferroic manganites. Rare earth ions still determine such details like the orientation of Mn spin cycloid at low temperatures and magnetic field induced phase transitions.

Although there are many experimental evidences that the magnetic structure in $\text{Eu}_{1-x}\text{Y}_x\text{MnO}_3$ is a spin cycloid at low temperature, no direct confirmation from the neutron scattering experiments is known to date. The reason for this is strong absorption of neutrons by Europium, with the absorption coefficient over 50 cm^{-1} for $\text{Eu}_{0.5}\text{Y}_{0.5}\text{MnO}_3$ in the range of wavelengths $2 - 5 \text{ \AA}$ [61]. Such experimental data are available for TbMnO_3 . Another pure manganite, DyMnO_3 has shown enhanced ferroelectric properties and also is interesting to investigate in the scope of the possible influence of rare earth magnetism. These two compounds are discussed in the next two chapters of the present work.

6 DyMnO₃: electromagnon as a soft mode

Dysprosium manganite is one of the few rare earth manganites which exhibits incommensurate spin ordering at low temperatures. According to the phase diagram in Fig. 1.11 the Mn-O-Mn angle for DyMnO₃ lies on the lower side of incommensurate compounds, but well within its bounds. This makes the sinusoidal and cycloidal magnetic phases much more robust against external magnetic fields and favourably distinguishes DyMnO₃ from GdMnO₃ where the magnetic history can play a role at low temperatures. Being a pure compound results in a better reproducibility among different samples but Dy brings some drawbacks too. It has quite large magnetic moment and Dy ordering at low temperatures (around 5 K) may interfere with magnetic structure of Mn ions. However, interesting sinusoidal and cycloidal orderings arise well above this temperature which, together with the results on Eu_{1-x}Y_xMnO₃, indicates that the magnetoelectric phenomena are primarily driven by Mn spins. The large neutron absorption cross section of Dy (over 20 cm⁻¹ for $\lambda_{neutron} = 2 - 5 \text{ \AA}$ [61]) makes it difficult to investigate the spin structure of DyMnO₃ by neutron diffraction but there are other techniques [21, 74] that can indirectly probe magnetic structure of the material.

6.1 THz excitations in zero magnetic field

This compound belongs to the most studied multiferroic manganites with orthorhombic structure. Below the Néel phase transition at $T = 39 \text{ K}$ DyMnO₃ first possesses an incommensurate magnetic order with the modulation wave vector $k = 0.36$ along the b axis [20, 21, 74]. Due to the big absorption cross section of Dy there is no neutron scattering data available for this material. However, analogously to TbMnO₃, one can assume that Mn spins form a collinear sinusoidally modulated structure in this temperature range. Below $T = 19 \text{ K}$ the spontaneous static electric polarization arises parallel to the c axis [20, 75, 76]. As has been proven both theoretically and experimentally, cycloidal spin structure breaks the spatial and time inversion symmetry thus assisting the occurrence of ferroelectricity. Therefore, it is naturally to assume that the magnetic order turns into the spin cycloid with the manganese spins rotating in the crystallographic bc plane. The wave vector at these temperatures slightly increases up to the value of $k = 0.385$ remaining incommensurate [21, 74]. Finally, at $T = 5 \text{ K}$ another magnetic transition is observed which is characterized by the commensurate ordering of the Dy sublattice with the wave vector $k = 0.5$ along the b axis [77].

Figure 6.1 shows temperature dependence of the dielectric permittivity of DyMnO₃

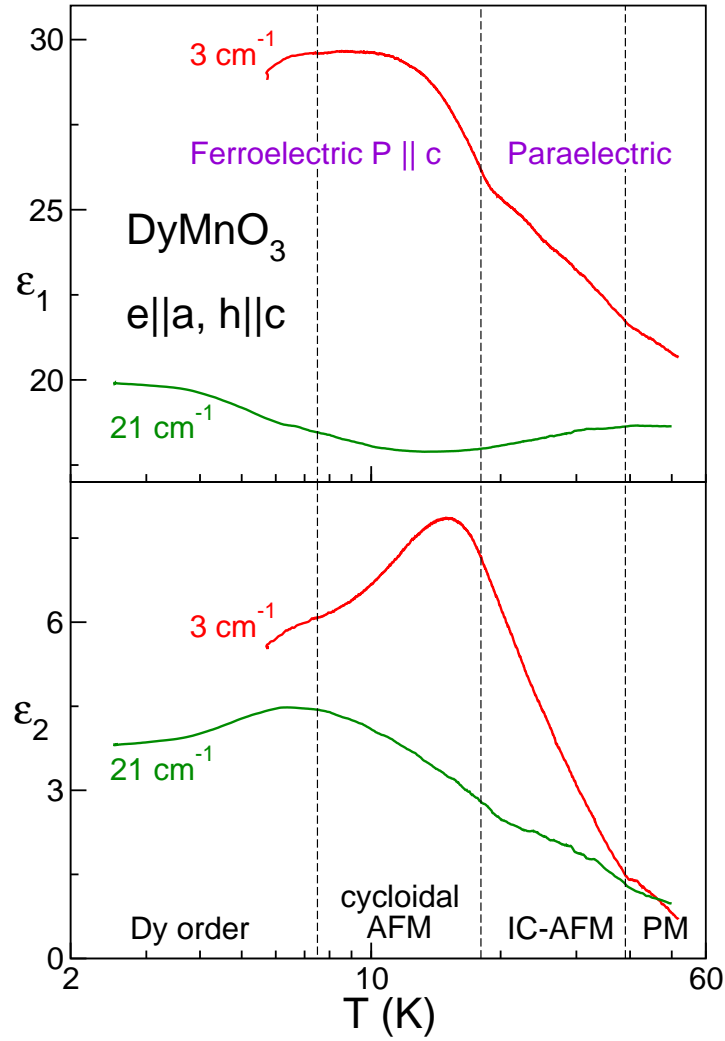


Figure 6.1: Temperature dependence of the terahertz dielectric permittivity of DyMnO_3 along the a axis and in zero external magnetic field. Upper panel - real part, lower panel - imaginary part. Dashed lines indicate the temperatures of the magnetic phase transitions. PM - paramagnetic, IC-AFM - incommensurate antiferromagnetic (sinusoidal), cycloidal AFM - incommensurate antiferromagnetic with Mn spins ordered in a cycloid, Dy-order - magnetic phase with ordered Dy-sublattice.

at two different frequencies. All above mentioned magnetic phase transitions, which are indicated by dashed lines, can be detected in the dielectric constant. This immediately suggests rather strong magneto-electric interaction in this material. It is noticeable that the phase transition anomalies are much more pronounced at low (3 cm^{-1}) rather than at high (21 cm^{-1}) frequency. Assuming that the reason for these peculiarities in the dielectric constant is some quasi-particle excitation at some frequency, it can be concluded that the stronger mode should be between 3 cm^{-1} and 21 cm^{-1} . Indeed, as is seen in Fig. 6.2 one of such excitations, termed electromagnon [16] exist around 16 cm^{-1} .

Similar to such multiferroics like GdMnO_3 or TbMnO_3 , DyMnO_3 shows a series of

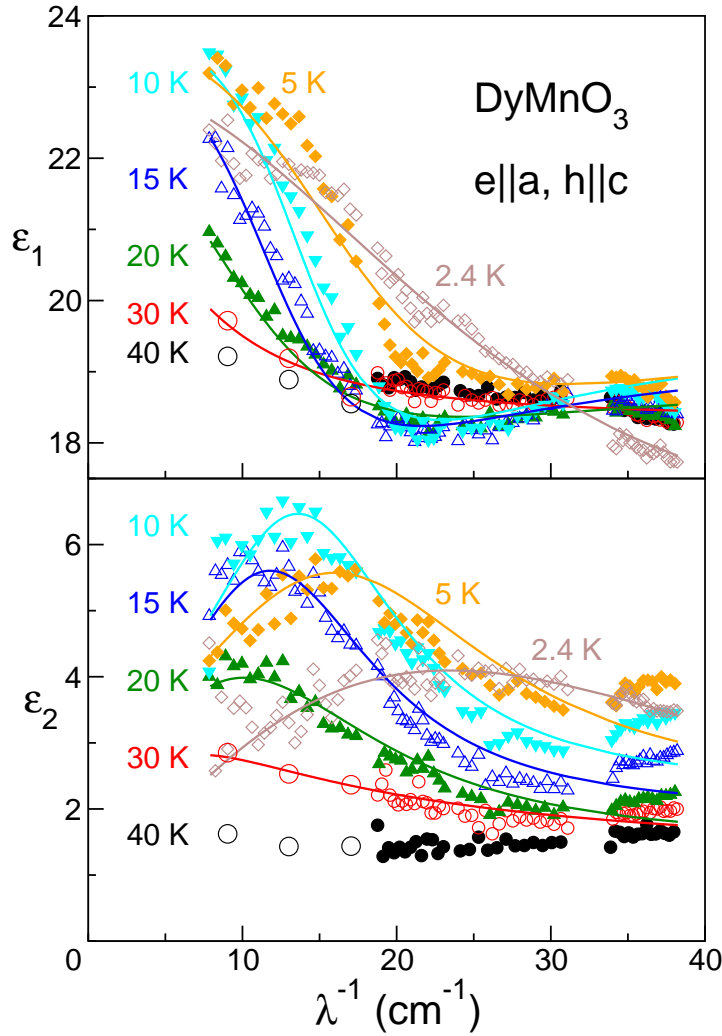


Figure 6.2: Terahertz dielectric spectra of DyMnO_3 along the a axis. Upper panel - real part, lower panel - imaginary part. Symbols - experiments, lines - Lorentzian fits. Large symbols have been obtained from the analysis of the transmittance only.

electro-active excitations at finite frequencies, which basically consists of two modes at 2 and 5.5 meV (16 and 48 cm^{-1}), respectively [60, 78]. This is demonstrated in Fig. 6.2 which shows terahertz spectra of DyMnO_3 at different temperatures for $e||a$ axis. In the paramagnetic phase ($T > 39$ K) only a broad relaxator-like absorption plateau is seen in the spectra. It is most likely due to short-range spin fluctuations which are precursor of the transition to the spin-ordered state. A significant magnetoelectric contribution (electromagnon) appears in DyMnO_3 below $T_N = 39$ K and at low frequencies. Below the transition to the spiral phase this contribution narrows showing an eigenfrequency around 16 cm^{-1} . The dielectric strength of the electromagnon in DyMnO_3 decreases below the Dy-ordering at $T = 5$ K and the mode at 16 cm^{-1} becomes again broad. The spontaneous electric polarization also decreases upon ordering of Dy spins [20]. The explanation of these effects was found in Ref. [79]. Above the ordering temperature

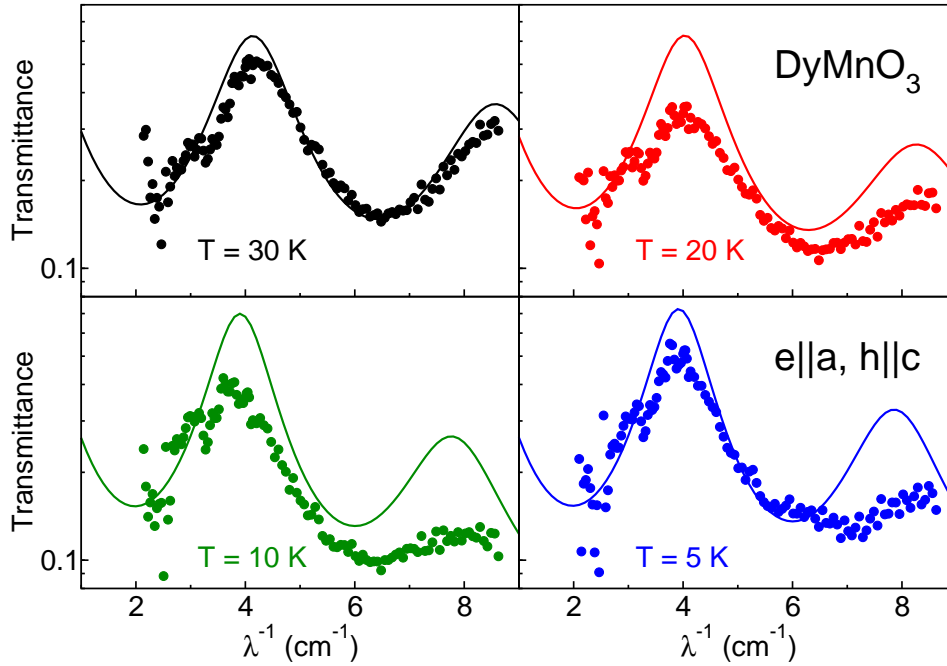


Figure 6.3: Terahertz transmittance spectra of DyMnO_3 along the a axis at different temperatures in the low frequency range. Upper left panel - incommensurate sinusoidal phase, upper right panel - the onset of cycloidal phase, lower left panel - cycloidal phase and lower right panel - the phase with separate Dy ordering. Symbols - experiments, lines - Lorentzian fits with the same parameters as in Fig. 6.2.

Dy magnetic moments follow Mn spins and form cycloid with the same wave vector as Mn spins. One can say that the spin cycloid is substantially “enhanced” due to additional Dy moments. This leads to enlarged static electric polarization and more pronounced electromagnon in THz spectra. Below $T = 5$ K the modulation wave vector of Mn spins stays incommensurate at $k = 0.385$ but Dy spins order commensurate with $k = 0.5$. The average contribution of Dy moments to Mn spin cycloid is zero now and these enhancement effects disappear. It is also possible to destroy the commensurate Dy order by applying external magnetic field. These aspects will be discussed in the next section.

The electromagnon at 16 cm^{-1} explains anomalies in the dielectric constant measured at 3 cm^{-1} . The changes of dielectric constant at 21 cm^{-1} are partially due to electromagnon at 16 cm^{-1} which is still close enough to the frequency of this experiment and partially due to the higher electromagnon at 48 cm^{-1} . One can see the onset of this high frequency electromagnon at the highest possible frequencies of our experimental setup. The data for a broader frequency range were published by Kida *et al* [78] using time domain spectroscopy. Their results basically agree with the data presented above showing both a strong excitation around 16 cm^{-1} and a second weaker mode around 48 cm^{-1} . Both excitations have been demonstrated to interact with the electric component of the radiation.

In contrast to TbMnO_3 and GdMnO_3 no additional excitations at low frequencies can

be observed. The spectra in Fig. 6.2 start at 8 cm^{-1} and there is a possibility that some excitation still exists below this frequency. In attempt to detect this mode experiments in the frequency range below 8 cm^{-1} have been performed. The transmittance spectra are shown in Fig. 6.3. Symbols represent experimental data and lines are fits with Lorentzian oscillators using the same parameters as in Fig. 6.2 (e.g. the same parameters as used to fit data at higher frequencies). The agreement between experimental data and fits is good at higher temperature $T = 30 \text{ K}$ (upper left panel in Fig. 6.3), in the sinusoidal phase. At lower temperatures $T = 20$ (upper right) and 10 K (lower left panel), just above and in the cycloidal phase, respectively, the fits predict too high transmittance evidencing some additional absorption in the sample at these frequencies. At $T = 5 \text{ K}$ (lower right panel), below Dy ordering temperature, there is again a rather good agreement between experiment and fits in the lower part of the spectrum, but experiment shows increased absorption at the higher frequencies. These results suggest that there could be a low frequency electromagnon between 2 cm^{-1} and 8 cm^{-1} . It should be noted, however, that the sample used in these experiments was quite thin for this frequency range: the thickness $d = 0.26 \text{ mm}$ was smaller than the typical wavelength of the radiation inside the sample $\lambda \simeq 0.4 \text{ mm}$. The parameters extracted from the fits of experimental transmittance are prone to a larger error under such conditions. Measurements on thicker samples are needed to draw a more definitive conclusion.

To summarize, Dy manganite shows a behaviour typical for other frustrated manganites with cycloidal spin structure at low temperatures. THz spectra reveal a broad relaxator absorption in the sinusoidal phase which transforms in the cycloidal phase into a strong well-defined quasi-particle modes at 16 and 48 cm^{-1} , termed electromagnons. These excitations are only seen for polarizations with the electric field of THz radiation along the crystallographic a axis, $e \parallel a$. There is an indication that a satellite of the lower frequency electromagnon exists between 2 and 8 cm^{-1} .

6.2 Electromagnons in external magnetic fields

In dysprosium manganite, the ferroelectricity is driven by magnetic ordering of the Mn sublattice, therefore it is important to investigate its properties in external magnetic fields. As with other manganites with incommensurate magnetic order, the direction of field plays an important role in case of DyMnO_3 . Application of magnetic field up to 14 T along c axis does not result in any significant changes in dielectric or magnetic properties [20]. This is contrast to other multiferroics like GdMnO_3 or TbMnO_3 which show magnetic phase transition to the canted antiferromagnetic order. The difference can be easily explained considering the position of these manganites on the phase diagram Fig. 1.11. GdMnO_3 lies on the boundary between A -type antiferromagnetic and incommensurate cycloidal orderings. A magnetic field along the c axis favours canting of spins in this direction and stabilizes canted A -type ordering. It is thus naturally that Gd manganite has the smallest critical field in the c direction and the canted phase can be stabilized even in zero magnetic field. TbMnO_3 is in the middle of incommensurate region and requires magnetic fields of the order of 10 T to switch into antiferromagnetic

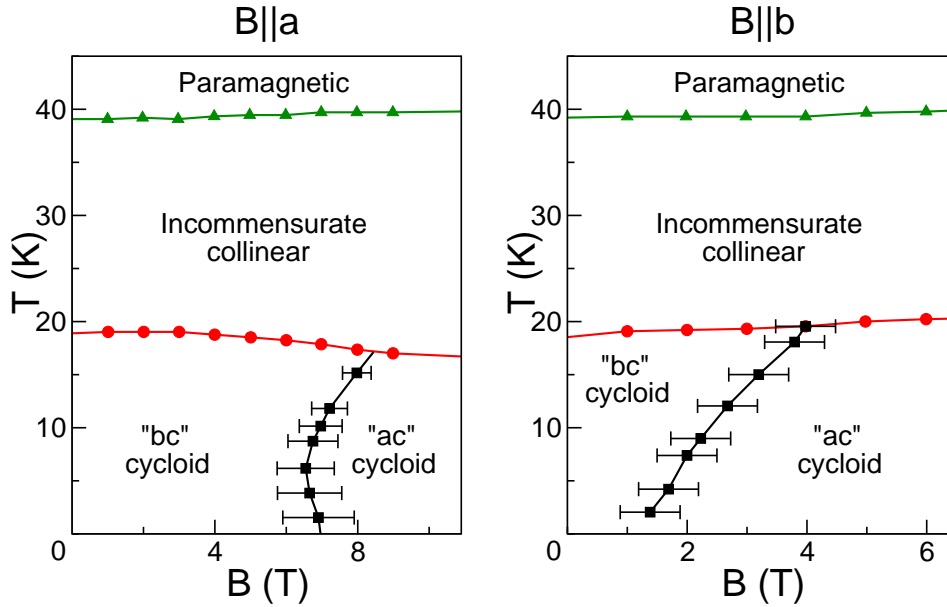


Figure 6.4: Magnetic phase diagram of DyMnO₃ for fields along the a (left panel) and b (right panel) axes. “ bc ” cycloid and “ ac ” cycloid denote the phases with Mn spin cycloid in the bc and ac crystallographic planes, respectively. Error bars for the bc - ac transition reflect the hysteresis and history dependence in different experiments. The phase with separate ordering of Dy spins is not shown. The data are taken from Ref. [20].

phase. DyMnO₃ is situated on the other side of the region with cycloidal ordering, close to “up-up-down-down” antiferromagnetic ordering. One can expect that in order to reach magnetic phase transition fields even larger than in TbMnO₃ are required.

Due to this stability of magnetic structure the magnetoelectric contribution in this compound cannot be suppressed by external magnetic fields along the c axis. Electric and magnetic properties of DyMnO₃ in magnetic fields along a and b axes have some interesting trends and will be discussed in the next two subsections.

6.2.1 Magnetic field along the a axis

In this part the changes of dielectric properties both in THz and low-frequency parts of the spectra in external magnetic fields along the a axis will be discussed. Figure 6.5 shows magnetic field dependencies of the complex dielectric constant at 3 cm^{-1} and various temperatures. The low temperature data sets clearly show a magnetic phase transition around $B = 5\text{ T}$. This transition is accompanied by the flop of spontaneous electric polarization from c to the a axis [20]. The cause of this flop seems to be the change of Mn spin cycloid orientation [20, 74]. Manganese spins flip from the bc to the ab plane. As the ferroelectricity is caused by this particular center-inversion breaking magnetic ordering, the electric polarization follows the spin cycloid across this transition. The higher temperature magnetic field scans do not show the aforementioned phase transition. This is in accordance with the phase diagram in the left panel of Fig. 6.4,

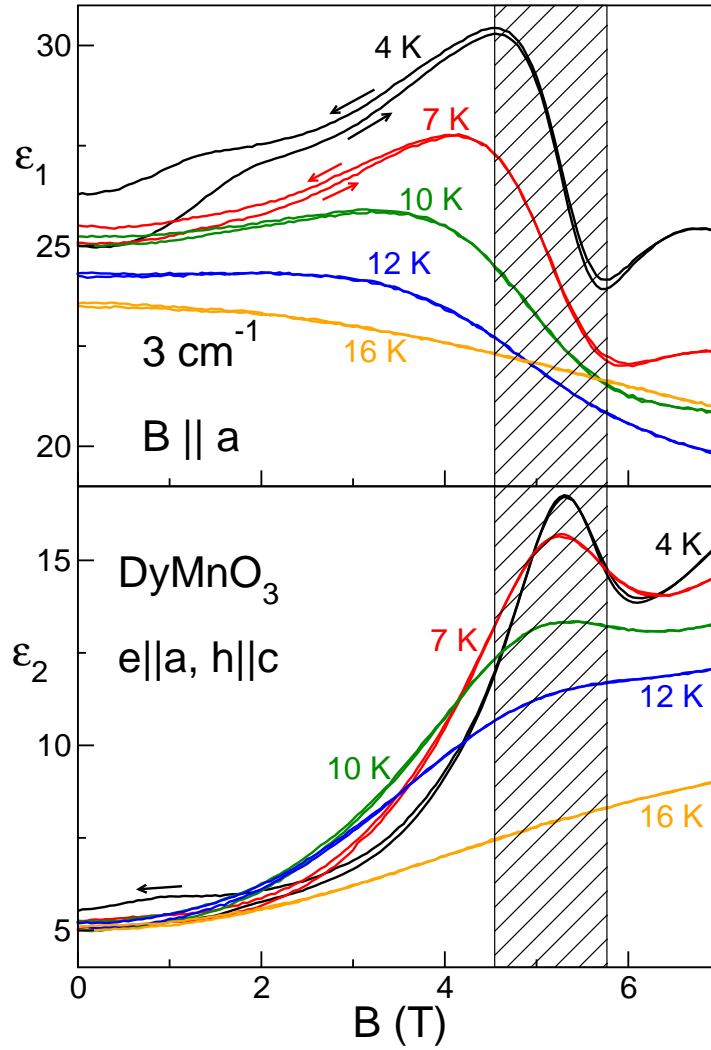


Figure 6.5: Magnetic field dependence of the real (upper panel) and imaginary (lower panel) parts of the dielectric permittivity $\epsilon^* = \epsilon_1 + i\epsilon_2$ of DyMnO_3 along the a axis for different temperatures. At magnetic fields around 5 T along a axes the transition to the ac -cycloid state can be observed.

due to limited magnetic fields available in our experimental setup.

More insight in what happens with the dielectric properties of DyMnO_3 in external magnetic field is provided by the spectra. Figure 6.6 shows the THz spectra of the low frequency electromagnon in DyMnO_3 at $T = 10$ K. At this temperature the Mn spins are magnetically ordered into the spin cycloid with Dy moments following them [74]. This phase is indicated as bc cycloid in the phase diagram shown in the left panel of Fig. 6.4. The spectra in Fig. 6.6 clearly demonstrate that in external magnetic fields $B \parallel a$ the electromagnon shifts to lower frequencies and gains an intensity. This behaviour reveals already at this point a close similarity to classical soft modes. The same suggestion was also made in Ref. [74]. The authors of this paper support this idea by the fact that both bc and ab Mn spin cycloids have the same modulation wave vector across this phase transition. Thus, both spin configurations are “similar” in some sense and have

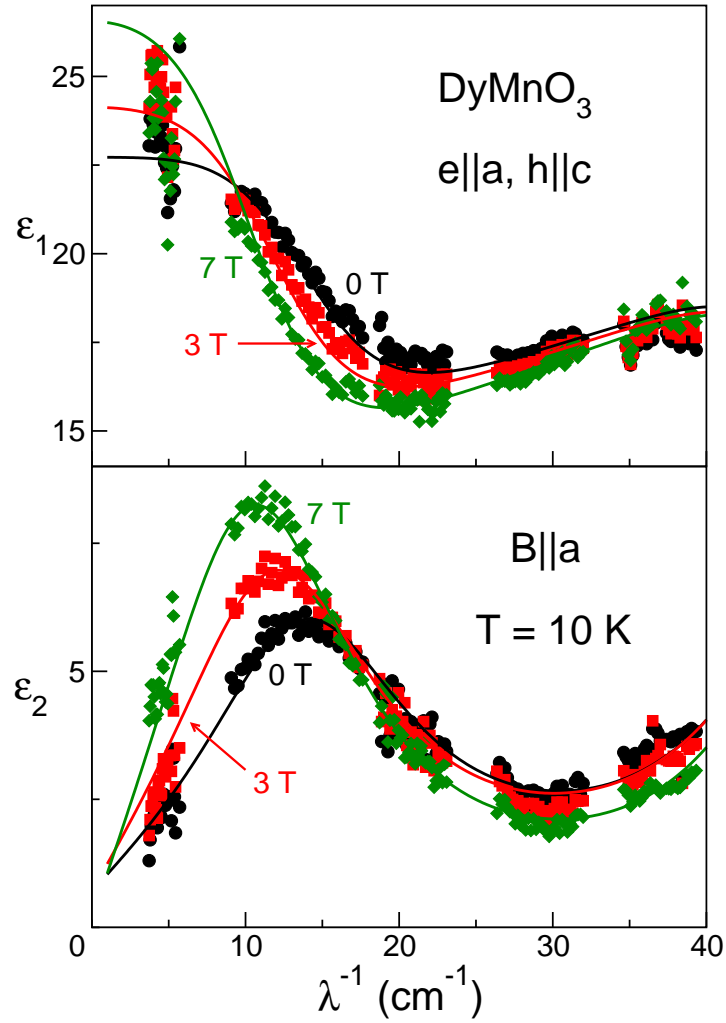


Figure 6.6: Softening of the electromagnon in DyMnO_3 . Frequency dependence of the real (upper panel) and imaginary (lower panel) parts of the dielectric permittivity $\varepsilon^* = \varepsilon_1 + i\varepsilon_2$ of DyMnO_3 along the a axis for different external magnetic fields $B||a$ at $T = 10$ K. For increasing magnetic fields a softening and a growth of intensity of the electromagnon is clearly observed.

almost identical energy. In this case the spin cycloid is almost free to rotate around b axis in the vicinity of the phase transition and acquires the soft mode. In order to investigate this scenario in more details, the quantitative analysis of the electromagnon using the Lorentz oscillator model and dielectric measurements at kHz frequencies were performed.

The spectra in Fig. 6.6 were fitted with one Lorentz oscillator corresponding to the low frequency electromagnon seen around 16 cm^{-1} and the second oscillator to account for the second high frequency electromagnon seen as an increase of dielectric absorption at the highest frequencies in the lower panel of Fig. 6.6. The parameters obtained are dielectric contribution $\Delta\varepsilon$, resonance frequency ω and damping γ . It is clear that the parameters of the high frequency electromagnon can not be reliably obtained from our

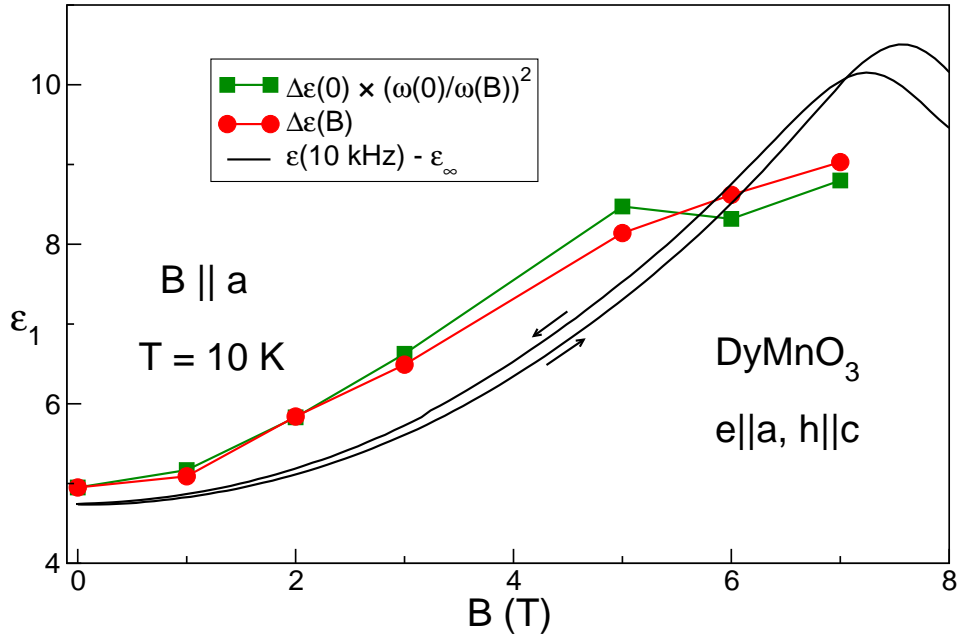


Figure 6.7: Comparison of the static and dynamic properties of DyMnO_3 along the a axis in magnetic fields $B \parallel a$. Red circles represent the measured dielectric contribution of the electromagnon. Green squares - dielectric contribution of the electromagnon as predicted by LST relation. Solid black line - static dielectric permittivity with a high-frequency value $\varepsilon_\infty = 25$ subtracted.

experimental data and it was included in the fit to better describe the high frequency region of the spectra. Figure 6.7 shows the obtained magnetic field dependence of the dielectric parameters. Red circles represent the field dependence of the dielectric contribution $\Delta\varepsilon$ of the low-frequency electromagnon showing an increase by more than a factor of two as approaching the phase transition to the ab -oriented spiral. The dielectric contribution closely correlates with the decrease of the resonance frequency, which is demonstrated by plotting $\Delta\varepsilon \cdot \frac{\omega(0)^2}{\omega(B)^2}$ (green squares). This plot corresponds directly to the Lyddane-Sachs-Teller (LST) relation and reflects the conservation of the spectral weight of the electromagnon in external fields parallel to the a axis.

Another manifestation of a soft mode is an increase of the static electric susceptibility at low frequencies. In our case it is the dielectric constant along the same a axis where the electromagnon is seen. In order to investigate this aspect, dielectric measurements in a parallel plate capacitor geometry at kHz frequencies were performed. As the THz setup requires the a axis laying in the plane of the sample and dielectric measurements need the a axis perpendicular to the plane of the sample, the experiments had to be done on different samples. Solid black lines in Fig. 6.7 show the field dependence of the static dielectric constant in DyMnO_3 as measured at 10 kHz. Here the contribution from the higher frequency processes ($\varepsilon_\infty = 25$) which is given by electronic transition, phonons, and a second electromagnon [78] was subtracted. We observe a close correlation between static and dynamic properties in spite of more than seven orders of magnitude difference in frequency. According to the sum rules this result demonstrates that for the geometry

$B\parallel a$ the changes in static properties are nearly completely governed by the softening of the electromagnon and no other contributions exist between kHz and THz frequencies.

As is already mentioned above, the softening of the electromagnon in external fields can be qualitatively understood taking into account the switching of the orientation of the spin cycloid. Similar to many other structural transitions the effective stiffness of the cycloid probably tends to zero on the phase border between the bc and ab cycloids, and as the result the electromagnon becomes the soft mode for this magnetic phase transition. The unresolved question is: why the spectral weight of the electromagnon is conserved during the softening of the eigenfrequency? In case of classical softening of the lattice vibration one normally argues that the spectral weight of the soft mode is directly connected to the total number of electrons in the material. In agreement with the charge conservation a constant spectral weight may be expected for soft phonons. In case of a magnetic cycloid the electromagnon gains the spectral weight as a result of a complex interplay of various mechanisms. Therefore, we cannot use the conservation of the magnetic moment as an argument. However, the measurements at lower temperatures, where Dy moments gain their own propagation vector could provide another point of view of the problem.

Figure 6.8 shows THz spectra of Dysprosium manganite at $T = 3$ K and magnetic fields along the a axis. The shift of the electromagnon eigenfrequency to lower frequencies and increase of its strength are much more pronounced at this temperature in comparison to $T = 10$ K (Fig. 6.6). Moreover there is a change of the electromagnon from a broad overdamped mode at $B = 0$ T to the strong well-defined oscillator at $B = 7$ T. Such an essential change can be however well understood by considering the behaviour of Dy magnetic moments. As was already mentioned, Dy spins follow Mn cycloid at intermediate temperatures $5 < T < 19$ K. At lower temperatures they are arranged with their own commensurate propagation vector $k = 0.5$. Due to this decoupling of Dy moments from the Mn spin cycloid the enhancement effects coming from Dy spins vanish and the electromagnon is only seen as a suppressed overdamped mode. However, this antiferromagnetic ordering of Dy subsystem can be suppressed in magnetic fields along a axis [74]. It is noticeable that this suppression takes place at much lower magnetic fields of about 1.5 T than the flop of Mn spin cycloid from bc to ab plane at 5 T. Therefore already in the magnetic field of 3 T (red symbols and line in Fig. 6.8) electromagnon is seen as a well-defined oscillator and closely resembles the spectra at 10 K without magnetic field (cyan symbols and line in Fig. 6.2). In other words, it is possible to destroy antiferromagnetic ordering of Dy spins either by temperature or by external magnetic field along the a axis with the same manifestations in the dielectric properties of DyMnO_3 . Such a universal behaviour supports the proposed scenario of the influence of Dy spins on the electromagnon in THz region and static spontaneous polarization. While rare earth atoms are not the cause of the peculiar magnetic structure and associated dielectric properties of DyMnO_3 at low temperatures, they seem to play a significant role in this compound.

In higher magnetic fields, up to 7 T in our experimental setup which roughly corresponds to the critical field of transition from the bc spin cycloid to the ab cycloid, electromagnon shifts further towards lower frequencies and gains in intensity. This is

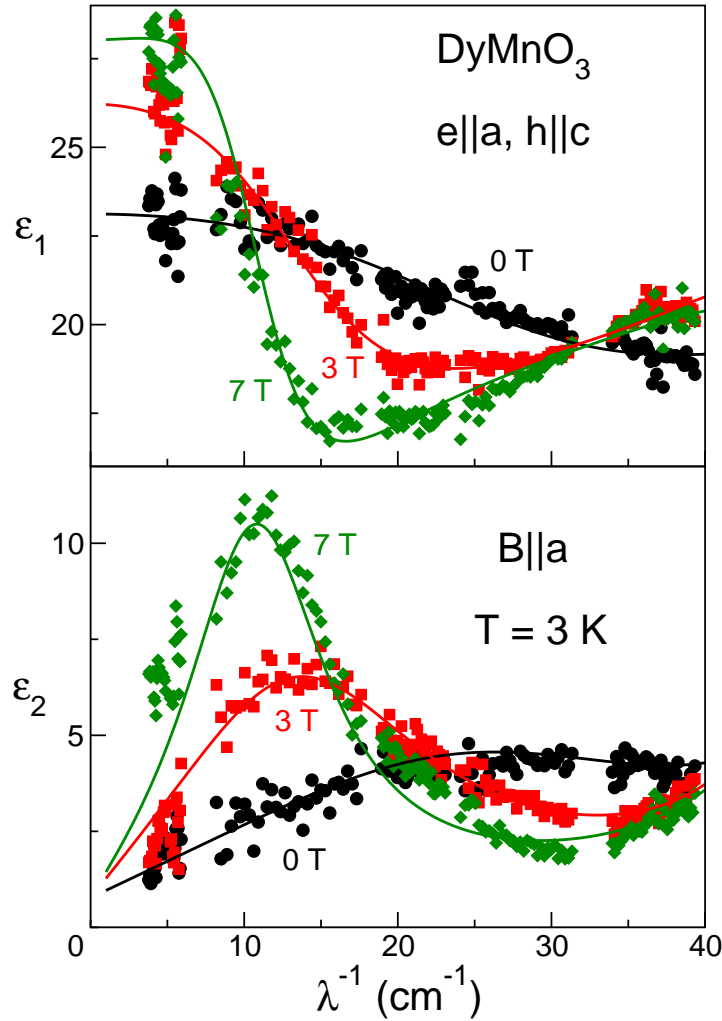


Figure 6.8: Evolution of the electromagnon in DyMnO_3 at low temperatures. Frequency dependence of the real (upper panel) and imaginary (lower panel) parts of the dielectric permittivity $\epsilon^* = \epsilon_1 + i\epsilon_2$ of DyMnO_3 along the a axis for different external magnetic fields $B||a$ at $T = 3$ K. There is a qualitative change of electromagnon from the broad overdamped mode at $B = 0$ T to a well-defined oscillator for $B \geq 3$ T.

similar to a behaviour of electromagnon at higher temperatures and still supports the assumption that electromagnon is a soft mode of the magnetic phase transition from the bc to the ab phase. This phase transition can be initiated not only by magnetic field along the a axis but along the b axis also. Measurements in the last geometry can provide more data to understand the problem and will be discussed in the next subsection.

6.2.2 Magnetic field along the b axis

We turn now to the experimental geometry in which the transition from the bc to the ab cycloid is achieved by magnetic fields along the b axis. Figure 6.9 shows dependencies

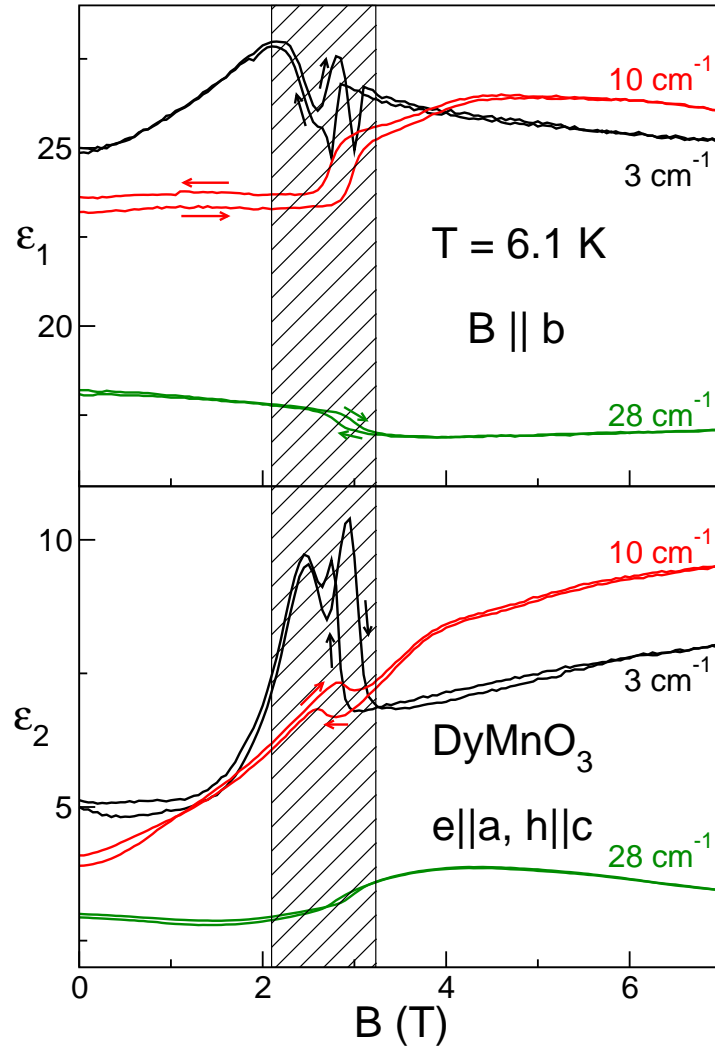


Figure 6.9: Magnetic field dependence of the real (upper panel) and imaginary (lower panel) parts of the dielectric permittivity $\varepsilon = \varepsilon_1 + i\varepsilon_2$ of DyMnO_3 along the a axis for different temperatures. In magnetic fields around 3 T along the b axis the transition to the ac -cycloid state can be observed.

of dielectric constant along the a axis on magnetic fields along b axis at $T = 6$ K and different frequencies in the THz range. Transition from the phase with spin cycloid in the bc plane to the phase with cycloid in the ab plane is clearly visible and takes place at substantially lower fields of around 3 T, compared to data for magnetic fields along the a direction (Fig. 6.5). The temperature of the experiment at $T = 6.1$ K is just above the ordering of Dy subsystem at $T = 5$ K so no or only negligible effects due to Dy moments are expected.

Figure 6.10 reveals the terahertz spectra of the electromagnon in this geometry. Similar to the data in Fig. 6.6, these results show an increase of the electromagnon intensity in external magnetic fields. However, already the comparison of the spectra at 6 T (green diamonds and line) and at 2 T (red squares and line) suggests that the increase of the mode intensity is not directly correlated with the decrease of the resonance frequency.

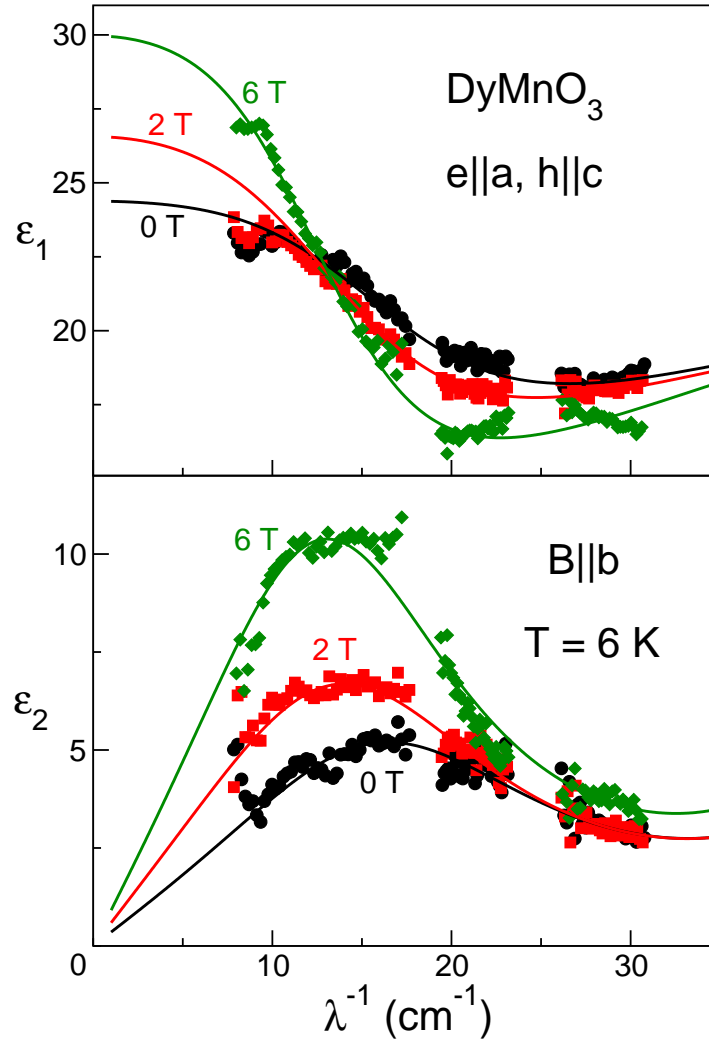


Figure 6.10: Behavior of electromagnon for external magnetic fields along the b axis. Frequency dependence of the real (upper panel) and imaginary (lower panel) parts of the dielectric permittivity of DyMnO_3 for $e||a$ for different external magnetic fields at $T = 6$ K.

Even without exact analysis of the fits one can see that the maxima in ε_2 for 2 T and 6 T roughly coincide in spite of different intensities. In order to draw more quantitative conclusions, the same fit procedure as for data for $B||a$ was used.

Figure 6.11 presents the results of mode parameters extraction. Red circles represent here the strength of the electromagnon which increases continuously in the whole range of the magnetic fields investigated. Contrary to the results for the $B||a$ (Fig. 6.7), above the transition to the ab cycloid at 2 T the mode contribution $\Delta\varepsilon$ deviates from the LST prediction $\Delta\varepsilon \cdot \frac{\omega(0)^2}{\omega(B)^2}$ (green squares in Fig. 6.11). This reflects that the spectral weight of the electromagnon is not conserved in external fields $B||b$.

The dielectric permittivity of DyMnO_3 along the a direction at 10 kHz was also measured and is shown as a black line in Fig. 6.11. The most prominent is the peak

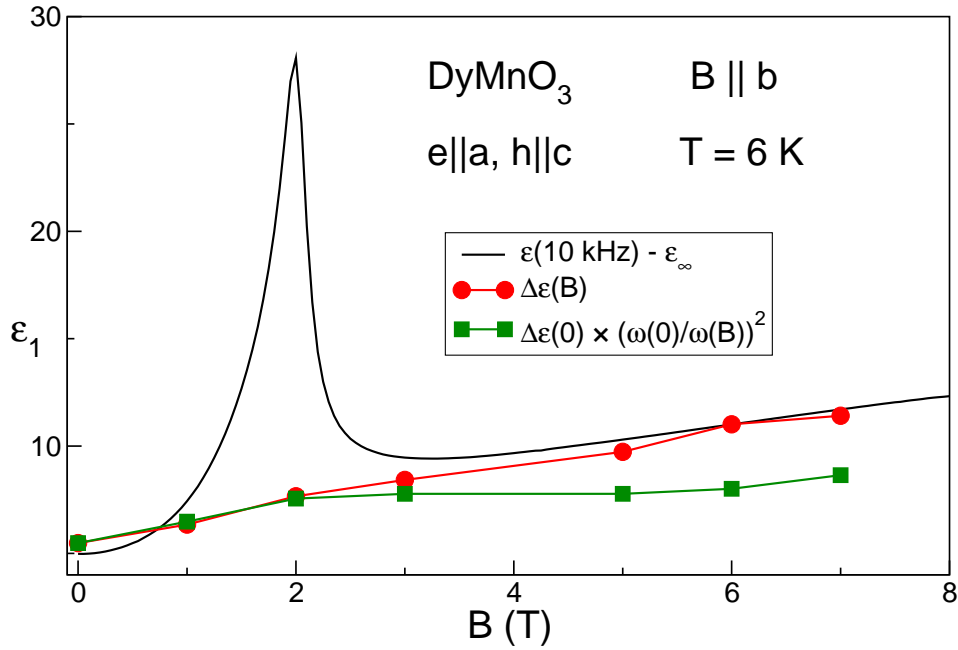


Figure 6.11: Comparison of the static and dynamic properties of DyMnO₃ along the *a* axis in magnetic fields $B||b$. Red circles represent the measured dielectric contribution of the electromagnon. Green squares - dielectric contribution of the electromagnon as predicted by LST relation. Solid black line - static dielectric permittivity with a high-frequency value $\epsilon_\infty = 25$ subtracted.

at the phase transition from *bc* to *ac* cycloid at $B = 2$ T. Dielectric properties at THz frequencies show no such peak which suggests that basic contribution to ϵ_{static} around the phase transition comes from other processes. Further investigations of the origin of this peak were made in Ref. [80] by Kagawa *et al* in which the dielectric contribution of the domain walls in DyMnO₃ have been studied. It has been shown that the peak in the dielectric constant around *bc*-to-*ab* phase transition is due to domain wall relaxation with characteristic frequency situated at radiowaves. Therefore close to $B = 2$ T the main changes in the static permittivity are due to the motion of the domain walls. Outside this region however, the overall increase of the static permittivity corresponds well to the dielectric contribution of the electromagnon. Although the electromagnon softens much weaker than in the $B||a$ geometry, its spectral weight still governs the high field behaviour of the static permittivity. The spectral weight of the low frequency electromagnon is not conserved in external magnetic fields $B||b$ and its conservation in magnetic fields along *a* direction at temperatures $T > 5$ K seems at this point to be more a coincidence rather than the manifestation of some underlying basic laws like conservation of magnetic moments.

6.3 Summary

The terahertz spectra of Dysprosium manganite for $e||a$ polarization reveal two strong excitations, called electromagnons, which appear together with the emergence of spon-

taneous electric polarization along the crystallographic c axis. Although the neutron scattering data are not available for this material, these two effects seem to be a manifestation of a peculiar magnetic ordering of the system. All experimental evidences and results on similar rare earth manganites point towards cycloidal structure of manganese spins at temperatures below 19 K. Magnetic fields along the c direction were not high enough in experiments up to now to suppress the ferroelectricity in DyMnO_3 . On the other hand, the magnetic fields along a or b crystallographic axes lead to a rotation of the electric polarization from a to c axis. This can be well explained by the rotation of the spin cycloid from bc to ab plane. However both electromagnons at 16 cm^{-1} and 48 cm^{-1} do not change their excitation condition and stay visible for THz electric field $e\parallel a$ upon this magnetic phase transition. This may suggest that the mechanisms responsible for the spontaneous polarization and for the electromagnons are different. There are some experimental evidences for additional absorption mode between 2 and 8 cm^{-1} which could be interpreted as a vibration mode of magnetic cycloid. But the accuracy of present experiments is not enough to draw a definitive conclusion here.

As had been shown in Chapter 5 it is Mn spins which drive the ferroelectricity in this class of manganites. In particular case of DyMnO_3 , the Dy moments play a role and substantially enhance the spin cycloid until they order separately into antiferromagnetic arrangement below $T = 5\text{ K}$. This transition is well seen in dielectric properties as a decrease of the static electric polarization or overdamping of the low frequency electromagnon. The antiferromagnetic ordering of Dy moments can be suppressed in moderate magnetic fields $B\parallel a$ that still below the transition to another orientation of Mn spin cycloid. This results in an increase of electric polarization and it also brings back the well-defined character of the low frequency electromagnon.

The behaviour of the electromagnon at 16 cm^{-1} in a broader range of magnetic fields along a and b axes is similar to classical soft modes. The spectral weight of this electromagnon governs the static dielectric permittivity for the whole range of magnetic fields $B\parallel a$ and for magnetic fields $B\parallel b$ except the vicinity of the phase transition at 2 T. This analogy lacks however the underlying conservation law like the conservation of charge in the case of soft phonons, and the spectral weight of electromagnon is generally not conserved.

The lack of detailed knowledge of magnetic structure of DyMnO_3 does not allow the construction of reliable theoretic models. The overall experimental results, on the other side, closely resemble another rare earth manganite, TbMnO_3 . This last compound was intensively studied including neutron scattering experiments and its magnetic structure is well known. Therefore theoretical models suggested for TbMnO_3 can also be applied to Dysprosium manganite and the properties of TbMnO_3 will be discussed in the next chapter.

7 TbMnO₃: electromagnon internals

Among magnetoelectric manganites TbMnO₃ is probably one of the most intensively studied by spectroscopic methods. In addition to results by dielectric [2, 20] and optical [16] spectroscopies, the magnetic structure of this material is well known from neutron scattering experiments [35, 81, 82]. Due to low absorption coefficient (less than 2 cm⁻¹ for the neutron wavelength in the range of 2–5 Å [61]), inelastic neutron scattering data are available for TbMnO₃ [43] which allow to compare characteristic frequencies of spin excitations and of electromagnons.

7.1 Temperature dependence of excitations in zero magnetic field

TbMnO₃ orders antiferromagnetically at $T_N = 42$ K with the magnetic moments of Mn aligned along the b axis with an incommensurate sinusoidal modulation also along the b axis [35, 81, 82]. Upon cooling a second transition into a spiral phase occurs at $T_C = 28$ K with a slightly different modulation vector [35]. The cycloidal spin structure is oriented within the bc plane in this phase. This low temperature phase is ferroelectric with the spontaneous polarization parallel to the c axis [2]. The symmetry analysis [75, 83] confirms that static electric polarization along the c axis is allowed for this spin arrangement. Finally, a phase transition at about 9 K is attributed to the magnetic ordering of the Tb sublattice.

Figure 7.1 shows the temperature dependence of the dielectric permittivity of TbMnO₃ for the ac electric field parallel to the a axis ($e||a$). All magnetic transitions can be well observed in the dielectric data. This demonstrates already in this stage the coupling between magnetic and electric properties in TbMnO₃. The real part of the dielectric permittivity strongly increases with decreasing temperature which reflects the growth of the magnetoelectric contribution. The initial increase of the imaginary part on cooling is reversed below $T_C = 28$ K. As can be seen in the spectra below, this reflects the narrowing of the electromagnon. Below $T = 10$ K distinct structure is observed both in ϵ_1 and in ϵ_2 . This points towards an additional excitation with the energy around 10 cm⁻¹ and with a temperature-dependent characteristic frequency.

The strong magnetoelectric modes are well seen in Figure 7.2, which shows the terahertz spectra of TbMnO₃ for ac-electric field parallel to a axis ($e||a$). This is the axis with substantial absorption at terahertz frequencies. Both other directions are nearly

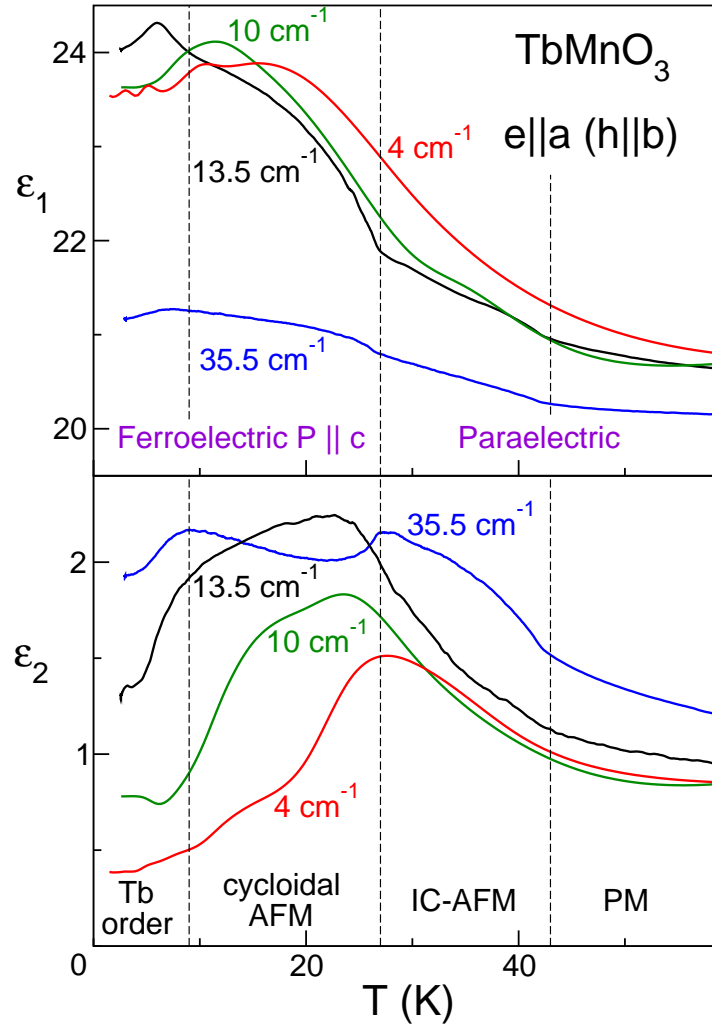


Figure 7.1: Temperature dependence of the terahertz dielectric constant of TbMnO_3 along the a axis in zero external magnetic field. Upper panel - real part, lower panel - imaginary part. Dashed lines indicate the temperatures of magnetic phase transitions. PM - paramagnetic, IC-AFM - incommensurate antiferromagnetic (sinusoidal), spiral - spiral (cycloidal) phase, Tb-order - magnetic phase with ordered Tb-sublattice.

transparent for terahertz radiation. For decreasing temperatures an over-damped excitation starts to grow in the spectra for $e||a$. In the real part of the dielectric permittivity this excitation is seen as a broad step-like increase towards low frequencies which corresponds to a maximum in the imaginary part. This broad feature can be identified as electromagnon. Especially in the spiral phase below 28 K the electromagnon narrows and becomes a well-defined excitation close to 23 cm^{-1} . The spectral weight of the electromagnon continues to increase upon cooling. In the spiral phase the electromagnon splits into two modes at 18 cm^{-1} and at 23 cm^{-1} . This splitting is well documented at $T = 2.5 \text{ K}$ because both components of the electromagnon are narrow at low temperatures.

Figure 7.3 shows the experimental transmittance of TbMnO_3 for all possible geome-

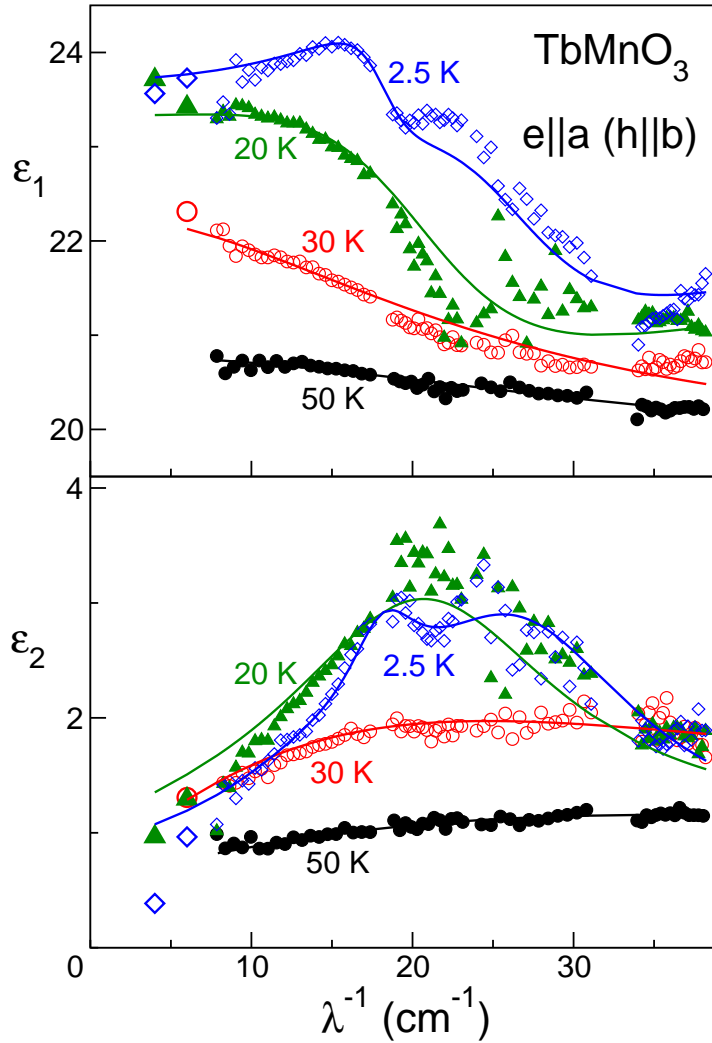


Figure 7.2: Terahertz spectra of TbMnO_3 for $e||a$ at different temperatures. Upper panel - real part, lower panel - imaginary part. Symbols - experiments, lines - fits using the sum of Lorentzians. Large symbols have been obtained from the analysis of the transmittance only. (e) and (h) indicate the ac electric and magnetic fields of the electromagnetic wave, respectively.

tries. All right and upper left panels of Fig. 7.3 have been obtained in geometries where magnetically excited modes are observed. We assign these modes to antiferromagnetic resonances in TbMnO_3 . Due to the comparative weakness of these modes, the transmittance is not far from unity even close to the resonance and the Fabry-Pérot oscillations on the sample surfaces are clearly seen. On the contrary, the excitation observed in the middle and lower left panels of Fig. 7.3 reveals much stronger absorption, which is partly close to the sensitivity limit of our spectrometer. As has been discussed previously [16, 60], these modes are excited by the electric field and are termed electromagnons.

As demonstrated in the middle and lower left panels of Fig. 7.3 and in the Fig. 7.2 the electromagnon mode splits into two excitations, which is most clearly seen in the spectra

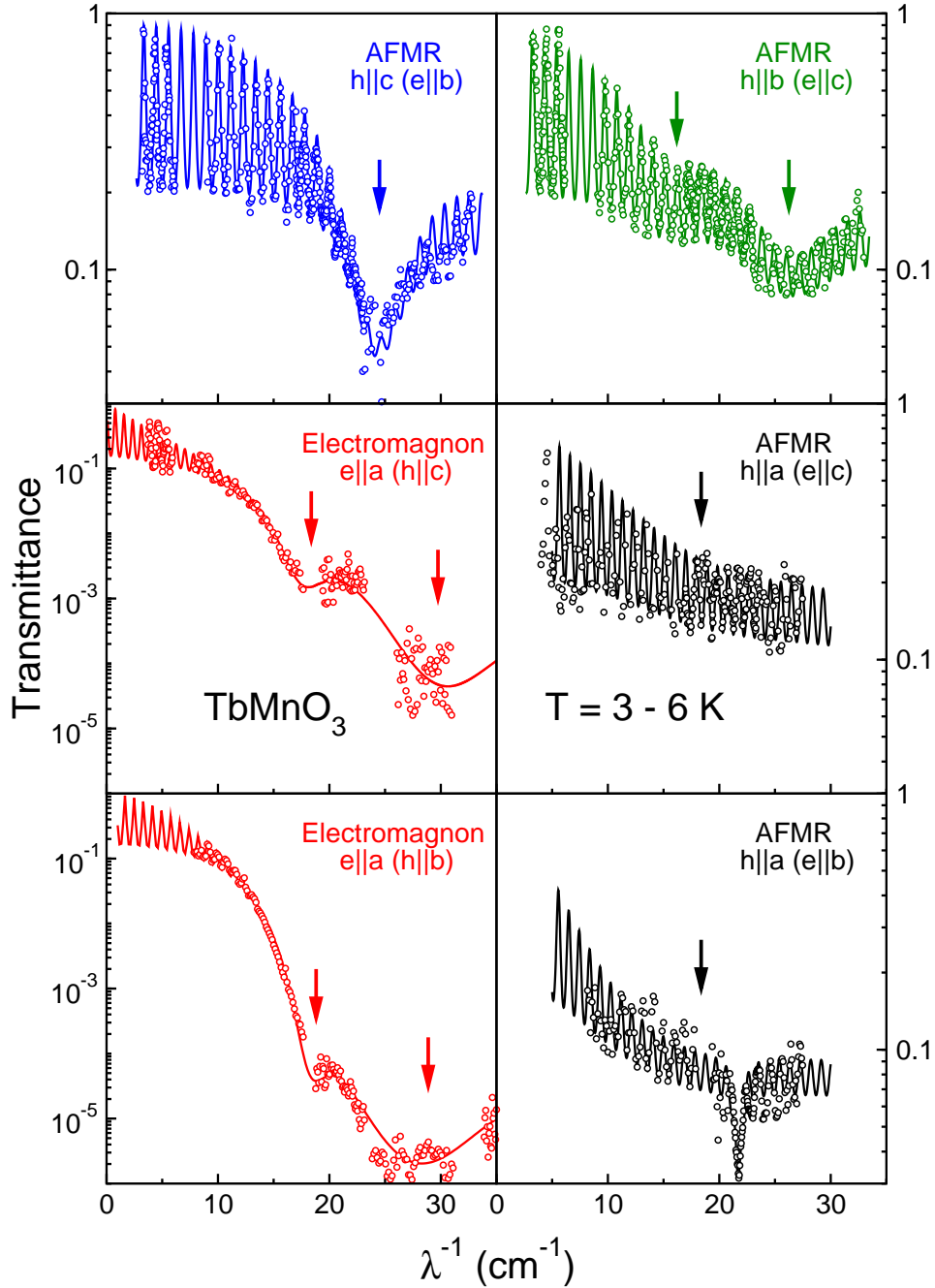


Figure 7.3: Examples of terahertz transmittance spectra of $TbMnO_3$ for different experimental geometries. Upper panel: the sample with a axis normal to the cut plane (“ a -cut”, the excitations along b and c axes are possible), middle panel: “ b -cut” sample and lower panel - “ c -cut” sample. Much lower transmittance in case of electromagnons is due to their stronger intensity compared to AFMR. Symbols - experiment, lines - fits using Lorentzian line shape. The oscillations in the spectra are due to Fabry-Pérot interferences on the sample surfaces. Specific geometry of each transmittance experiment is given in parentheses.

at the temperatures below 4 K. Using direct analysis of the transmittance spectra in combination with the temperature scans, the second weaker electromagnon at 18 cm^{-1} can be followed up to $T = 20 \text{ K}$, i.e. deep into the cycloidal phase. We conclude that this mode originally appears at zero frequencies and is probably the same as the low-frequency mode observed close to 9 cm^{-1} in inelastic neutron scattering (INS) [43, 44]. These experiments revealed two basic magnetic excitations in TbMnO_3 in the spiral AFM phase at $T = 17 \text{ K}$, at 9 cm^{-1} and at 20 cm^{-1} . The latter excitation corresponds well to the electromagnon seen in the terahertz spectra at 23 cm^{-1} .

In inelastic neutron scattering experiments the magnetic excitations can be directly addressed using polarized neutrons. An experimental difficulty that has to be overcome in this case is the separation of the signals from the magnetic and nuclear channels. The polarization analysis of the spectra allows to classify the observed magnetic excitation depending on their polarization state. Although the excitation geometries in the neutron scattering and in the terahertz absorption spectroscopy cannot be compared directly, they both provide information about the motion of the magnetic moments of each mode. Finally, the comparison of the eigenfrequencies from the INS and from terahertz experiments allows to draw conclusions about electric and magnetic character of the excitations.

Full dispersion relations of the magnetic excitations can be obtained in inelastic neutron scattering experiments. On the contrary, the optical experiments are in most cases sensitive to the center of the Brillouin zone only. The reason for this fact is the momentum conservation in absorption processes and the negligibly small momentum of the photon ($\hbar q_{ph} \approx 0$). Therefore, comparing the optical and INS results only the data at the zone center should be taken into account. The situation becomes far more complicated if the dynamic properties of the spiral magnets are considered. Firstly, the calculations of the excitation conditions for the eigenmodes of the spin cycloid reveal that the center of the crystallographic Brillouin zone is not excited in the optical experiments. Instead, a magnon with a specific wavevector $q = q_0$ can absorb the photon. Here $q_0 = 2\pi/\lambda_0$ is the propagation vector of the spin cycloid and λ_0 is the periodicity of the cycloid. The apparent violation of the momentum conservation during the absorption of the photon is recovered due to the correction equal to the reciprocal lattice vector of the cycloid. In the presence of a periodic modulation $Q = 2\pi/\lambda_0$ the *umklapp* processes with $k_0 = Q$ become allowed and the momentum conservation during the absorption of a photon with $q_{ph} \approx 0$ can be fulfilled: $q_{ph} \approx Q - k_0 = 0$. Therefore, in the following the frequency positions taken at the wavevector $q = Q$ will be plotted to represent the INS data. The coincidence of the frequencies from both experimental techniques supports this mode assignment and is one of the main arguments in favour of the eigenmode scenario.

The systematics of the magnetic and magnetoelectric excitations in perovskite multiferroic manganites can be well illustrated using TbMnO_3 as a typical example. The map of these excitations is shown in Fig. 7.4 which summarizes the results of both the inelastic neutron scattering (stars) and of the terahertz spectroscopy (circles, triangles, squares). Because magnetic and electric activity cannot be separated in the INS experiments, the same frequencies are plotted both in the upper and lower panel. In the lower panel two observed electromagnons are indicated by solid circles and squares. In

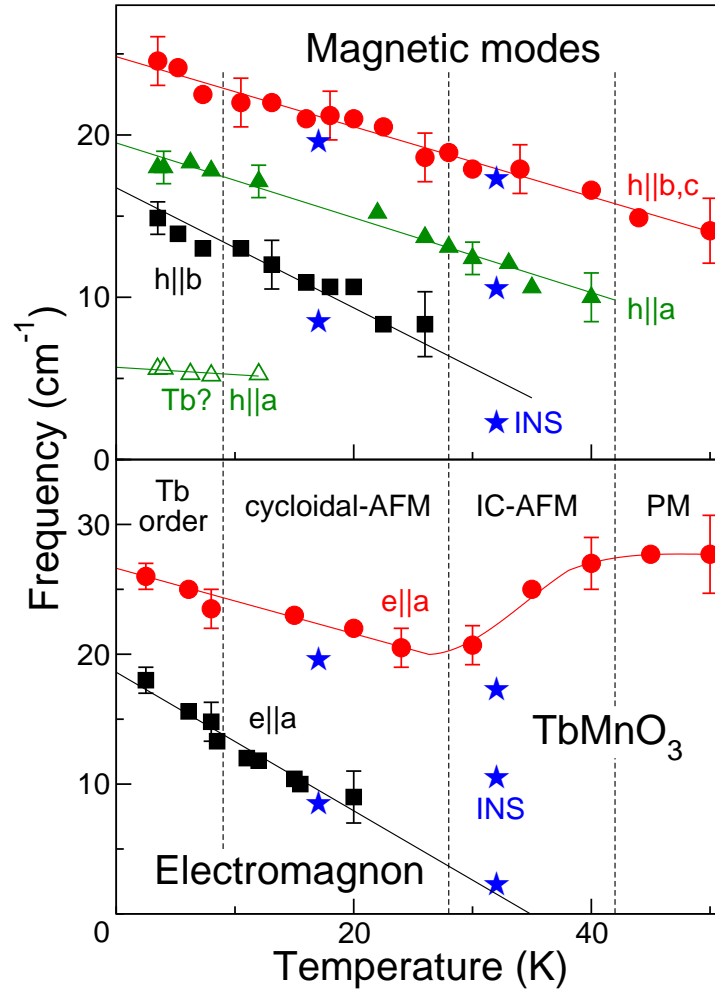


Figure 7.4: Frequencies of the magneto-active and electro-active excitations in $TbMnO_3$ as compared with the results by inelastic neutron scattering (INS) [43, 44]. The INS data are shown as stars. Upper panel: magnetic modes. Lower panel: electric modes (electromagnons). Symbols represent the experimental data, solid lines are drawn to guide the eye. The excitation conditions of the magnetic excitations are indicated at the curves. The electromagnons are excited in the geometry $e||a$ only. Dashed lines represent the boundaries between different magnetic phases. PM - paramagnetic, IC-AFM - incommensurate (sinusoidal) antiferromagnetic, cycloidal-AFM - cycloidal antiferromagnetic, Tb order - phase with ordered Tb sublattice.

the spin spiral phase the electromagnon energies correspond to the excitation energies of well defined quasi particles. In the collinear sinusoidal phase the electromagnons are seen as broad over damped modes [60]. The energies as plotted for $T > 27$ K correspond to the line width of these modes indicating that the damping strongly increases towards the transitions into the paramagnetic phase. The frequencies of the observed antiferromagnetic resonances in $TbMnO_3$ are plotted in the upper panel of Fig. 7.4 as closed symbols. In total, four such magnetic modes have been observed in the frequency range of our experiment. Remarkably, both AFMR and electromagnons can still be observed in the paramagnetic phase. This effect has been previously observed for other

multiferroics [60] and should be probably attributed to magnetic fluctuations. The two AFMR modes have frequencies very close to those of two electromagnons. In analogy to electromagnons, these two modes are indicated by closed circles (high frequency mode, excited by $h\parallel b$ and $h\parallel c$) and closed squares (low frequency mode, excited by $h\parallel b$). Another AFMR mode at intermediate frequencies which is given by closed triangles can be attributed to the phason mode of the magnetic bc -cycloid. This agrees with the excitations conditions $h\parallel a$ for this mode. The remaining magnetic mode around 5 cm^{-1} can be excited for $h\parallel a$. Based on the fact that this mode is observed mainly in the Tb-ordered phase, it can be attributed to the excitation of the ordered Tb moments.

The most important conclusion that can be drawn from the analysis of the data presented in Fig. 7.4 is that for each electromagnon (lower panel) there exists an excitation in the magnetic channel (upper panel) and this excitation is also seen in the INS data corresponding to the magnetic zone center. Strictly speaking, the last conclusion can be applied to the high-frequency electromagnon with some corrections only. The high-frequency electromagnon also reveals a magnetic counterpart. However, the magnetic excitation channel of this mode is seen as a zone boundary magnon in INS experiments and was not observed in the optical spectra.

Classical modes of magnetically ordered structures are excited via the interaction with the magnetic component of the electromagnetic field. In case of simple antiferromagnetic structures these are well known antiferromagnetic resonances which reveal two eigenmodes [66, 84]. As the magnetic ordering in perovskite magnetoelectric manganites is much more complex, additional complexity of the magnetic excitations in the ordered state of the spiral magnets may be expected. Within calculations performed in Refs. [38, 40, 50] two spin wave branches of the magnetic cycloid are obtained. One branch represents the out-of-plane oscillations of antiferromagnetic moment and it corresponds to a minimum in the dispersion relations $\omega(k)$ at the cycloid wavevector k_0 . This branch is doubly degenerate in the isotropic model. The other branch represents a so called phason mode corresponding to a rotation of the spins within the plane of the spiral and having a zero gap at $k = 0$ in the isotropic case.

With the presence of an anisotropy all three eigenfrequencies of the cycloidal spin structure generally become different. The frequency of the phason mode becomes nonzero and should be observed in the spectra of the magnetic excitations. Indeed, the third mode of a magnetic origin has been detected in TbMnO_3 both by terahertz spectroscopy [85] and by inelastic neutron scattering [43, 44]. Unfortunately, the mode assignment for the third mode and the eigenfrequencies in both experiments did not agree. In the INS spectra a shoulder slightly above zero energy has been observed and interpreted as a missing phason mode around $\nu \sim 0.1\text{ meV}$ (0.8 cm^{-1}). In the optical experiments such low frequencies can not be investigated up to now and, therefore, direct comparison of two experimental techniques is not available. On the contrary, in the optical experiments a third magnetic mode has been observed in the frequency range between both electromagnons (i.e. around 16 cm^{-1} (2 meV) at 17 K), shown as closed triangles in the upper panel of Fig. 7.4. This mode revealed pure magnetic excitation conditions which agreed with the predicted conditions ($h\parallel a$) for the phason mode of the bc spin spiral [85]. Therefore, the mode close to 16 cm^{-1} has been suggested as a phason

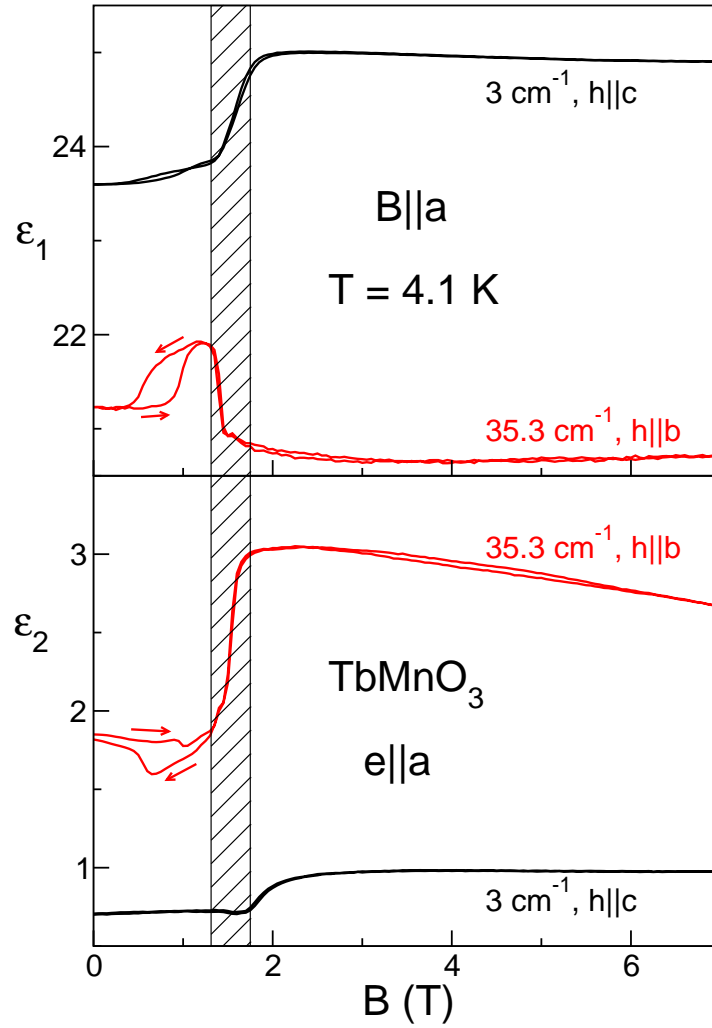


Figure 7.5: Dependence of dielectric properties of $TbMnO_3$ upon magnetic field along a axis.

of the cycloidal structure. We note that the analysis of the INS spectra in the collinear magnetic state [44] does reveal some additional feature close to 1.3 meV (2 cm^{-1}) at 32 K. Extrapolated to the lower temperatures, this mode would correspond to 2 meV (16 cm^{-1}) at 17 K and to the magnetic mode of the terahertz spectroscopy. However, this mode has been interpreted not as a phason but rather as further transverse magnon branch of the collinear state. Therefore, the question of the observation and assignment of the phason mode of the cycloidal structure still remains open.

7.2 Electric and magnetic excitations in external magnetic field

We discuss now the behaviour of the electromagnons in $TbMnO_3$ in external magnetic fields parallel to the crystallographic a and b axes. We recall that the external fields

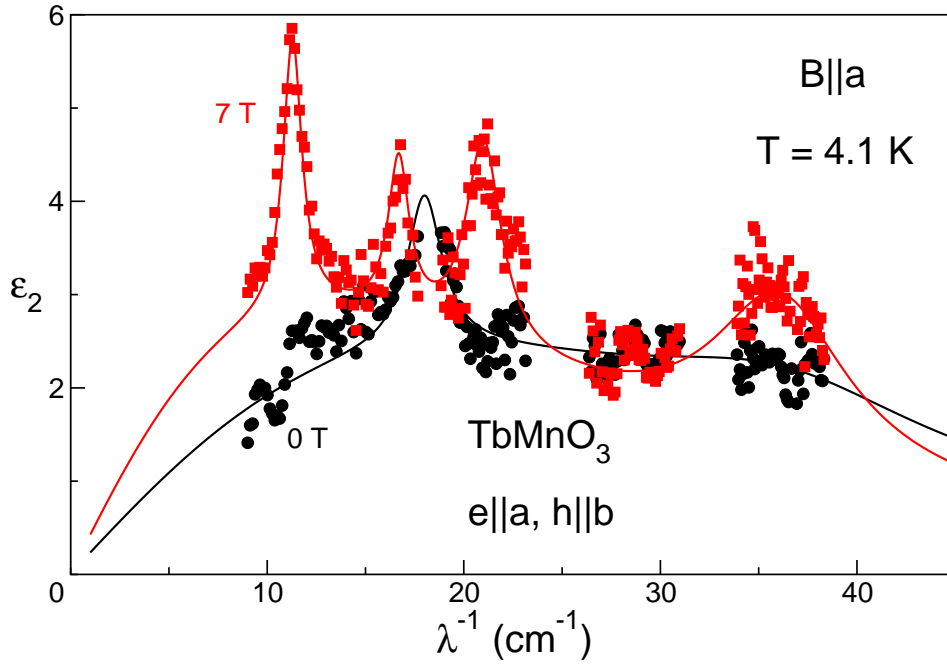


Figure 7.6: Dielectric permittivity spectra of TbMnO_3 in external magnetic field along a axis. Lines are fits using Lorentzian line shape.

along the c axis suppress the electromagnons [16] and induce a canted antiferromagnetic structure [20, 86]. In external magnetic fields along the a and b axes the magnetic cycloid rotates from the bc plane towards the ac plane [87, 88]. Correspondingly, the electric polarization rotates from $P||c$ axis to the $P||a$ axis [2, 20, 88]. Applying magnetic fields $\mu_0 H > 5$ T along the b axis allows for complete rotation of the cycloid plane. Along the a axis fields of more than 10 T are necessary and only a tilting of the cycloid can be achieved using our magnet (maximal field 8 T). In both cases and already for fields above ≈ 2 T substantial changes in the spectral structure of the electromagnons can be observed. For $B||a$ this is demonstrated in the magnetic field dependencies of dielectric properties in Fig. 7.5. The feature at 1.5 T in the real part of dielectric constant in the upper panel and step-like increase of the absorption in the lower panel for the high frequency (35.3 cm^{-1}) suggests the appearance of some additional mode in this range. The field scan at low frequency (3 cm^{-1}) shows a prominent increase of the dielectric constant around 2 T. Together with the sum rule this also supports the emergence of new absorption modes at higher frequencies.

The above assumptions are confirmed by the terahertz spectra shown in Fig. 7.6. Instead of initially two electromagnons four new modes in high magnetic fields are observed. The highest of these modes appears at the frequency around 35 cm^{-1} and explains the high frequency field dependence in Fig. 7.5. The solid lines in Fig. 7.6 are fits using the sum of four Lorentzians.

The magnetic field dependence of modes' parameters is represented in the Fig. 7.7. We attribute the appearance of these modes to the change of the excitation conditions

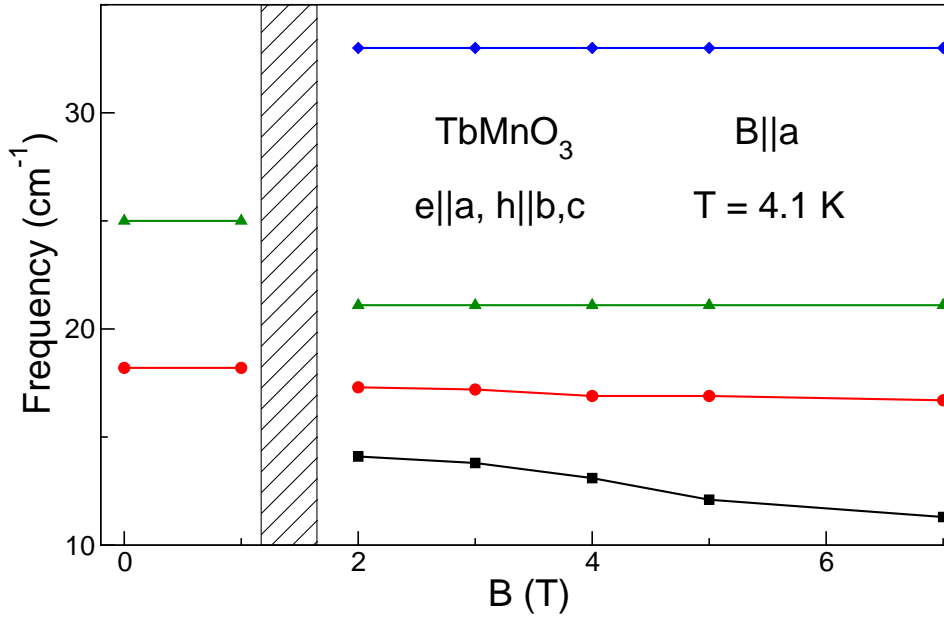


Figure 7.7: Dependence of mode frequencies in *TbMnO₃* upon magnetic field along *a* axis.

of the magnetic cycloid due to tilting. From the simple arguments the rotation of the magnetic cycloid from *bc* plane to the *ac* plane should simultaneously switch the excitation conditions for the electromagnons from $e||a$ to $e||c$. On the other hand, as the magnetic fields along the *a* axis are not enough to fully rotate the cycloid to the *ac* plane in our experiments, the cycloid stays at some intermediate tilted position. One can expect that such a tilted cycloid possesses additional degrees of freedom compared to pure *bc* or *ac* plane orientations. The new modes observed in high magnetic fields are possibly the manifestations of these degrees of freedom.

The behaviour of *TbMnO₃* in external magnetic fields along the *b* axis is of a greater interest. The most intriguing question here is whether the electromagnon follows the magnetic cycloid and would be observed in the $e||c$ geometry or whether it would be still excited for electric field along the *a* axis. The first case would support IDM model of the electromagnon while the second case - Heisenberg model. In the IDM model, the excitations of the spin cycloid must be coupled to its orientation. Most specifically, one should expect the electric activity along the *c* axis if the spin cycloid is oriented in the *ab* plane. However, such excitation conditions were not observed up to now [40, 85]. A possible reason for this fact is the weakness of the dielectric contribution of the spin modes within the IDM mechanism. In order to resolve this experimental difficulty, *TbMnO₃* seems to be an ideal candidate, because the magnetic cycloid can be fully rotated between *ab* plane and *bc* plane in magnetic fields available in our cryostat. This allows to investigate terahertz excitations in *TbMnO₃* with the fully tilted spin cycloid. The experiment in this case should include investigations for different polarization of radiation and possibly for samples cut along various crystallographic directions at the magnetically induced rotation of the cycloid.

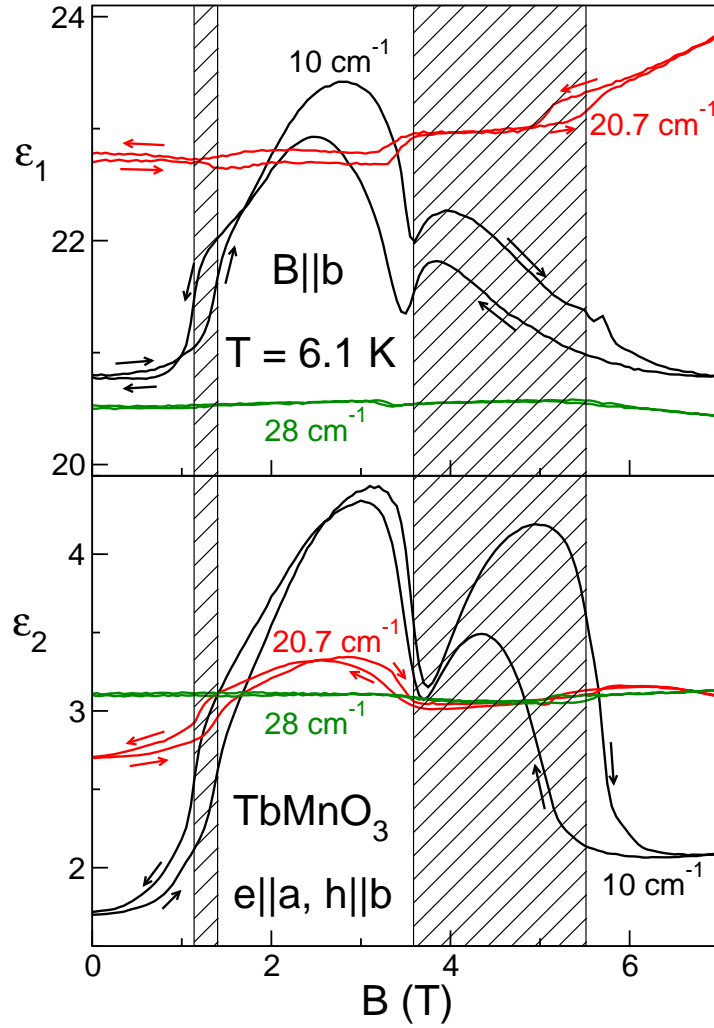


Figure 7.8: Dependence of dielectric properties of TbMnO_3 upon magnetic field along b axis.

We start with the geometry $e||a$ where the electromagnon is already present in zero magnetic fields. The magnetic field dependencies of dielectric constant are shown in the Fig. 7.8. The left dashed area represents the onset of spin cycloid rotation away from the bc plane. The broad dashed area in the right side marks the region where the magnetic cycloid locks to the ac plane. As is seen in the figure, the strongest changes occur in the low frequency range (the black curve obtained at 10 cm^{-1}). The frequencies around 20 cm^{-1} are affected substantially less, whereas in the high frequency range (30 cm^{-1}) almost no changes can be observed at all. The increased dielectric constant and absorption in the intermediate magnetic field range between two dashed regions supports the above hypothesis that the tilted spin cycloid has some additional degrees of freedom contributing to dielectric properties at low frequencies. Note that almost all curves except the red one go back to the values in zero magnetic fields when the cycloid is fully rotated to the ac plane.

The more detailed picture of the changes in the terahertz spectra in the high field

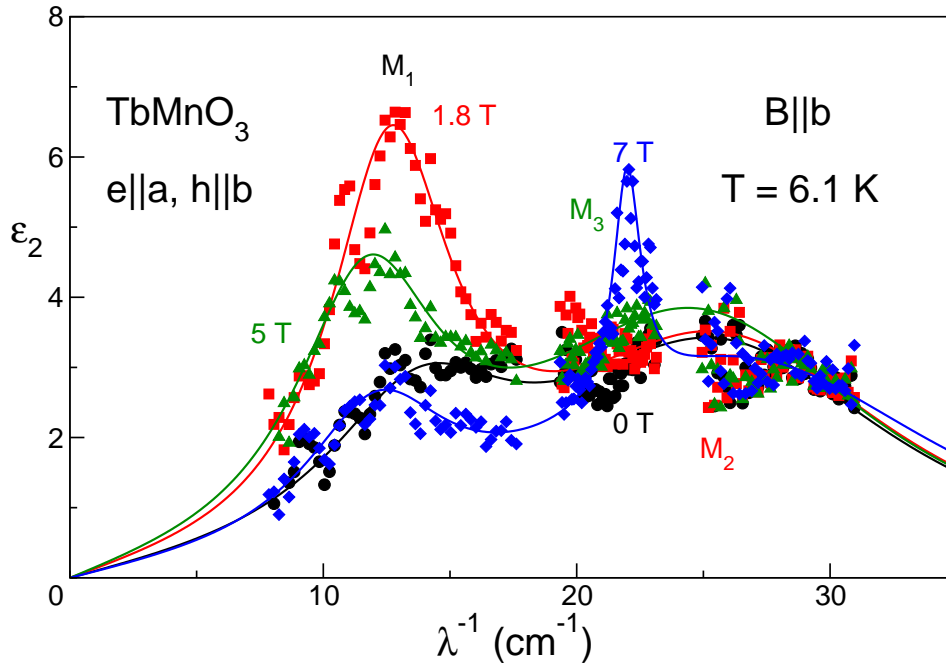


Figure 7.9: Dielectric permittivity spectra of $TbMnO_3$ in external magnetic field along b axis. Lines are fits using Lorentzian line shape. The modes M_1 and M_2 are seen in the whole range of magnetic fields, while the mode M_3 can only be observed in the high-field phase.

phase provides Fig. 7.9. The lines in this figure are model fits using only two Lorentz oscillators up to the fields of 5 T. Only the state with completely switched cycloid to the ac plane requires one additional oscillator around 22 cm^{-1} . The emergence of this mode is the reason for the increase of the real part of dielectric constant at 20.7 cm^{-1} in the Fig. 7.8. We note here the huge growth of lower frequency satellite of the electromagnon in the intermediate field range. This is also seen in Fig. 7.10 which shows the field dependencies of the resonance frequencies (lower panel) and strengths (upper panel) of the fitted modes. The black curve in the upper panel closely resembles the field dependence of dielectric constant at 10 cm^{-1} in the Fig. 7.8. This means that the contribution to the dielectric constant from the lower frequency satellite dominates in the lower part of terahertz spectra. The behaviour of $TbMnO_3$ in the external magnetic fields along b axis was also investigated by other experimental techniques. The inelastic neutron scattering experiments [87] reveal complex changes in the magnetic modes and complicated excitation conditions.

One quite important conclusion can be made already based on the experimental data in the geometry $e||a$. The strong overall dielectric absorption in this geometry stays present even when the spin cycloid is completely rotated to the ac plane. This challenges the IDM model of the electromagnon which directly relates the excitation condition to the orientation of the magnetic cycloid. Within this model the rotation of the magnetic cycloid from bc plane to the ac plane should simultaneously switch the excitation conditions for the electromagnons from $e||a$ to $e||c$. In order to check this prediction, a series

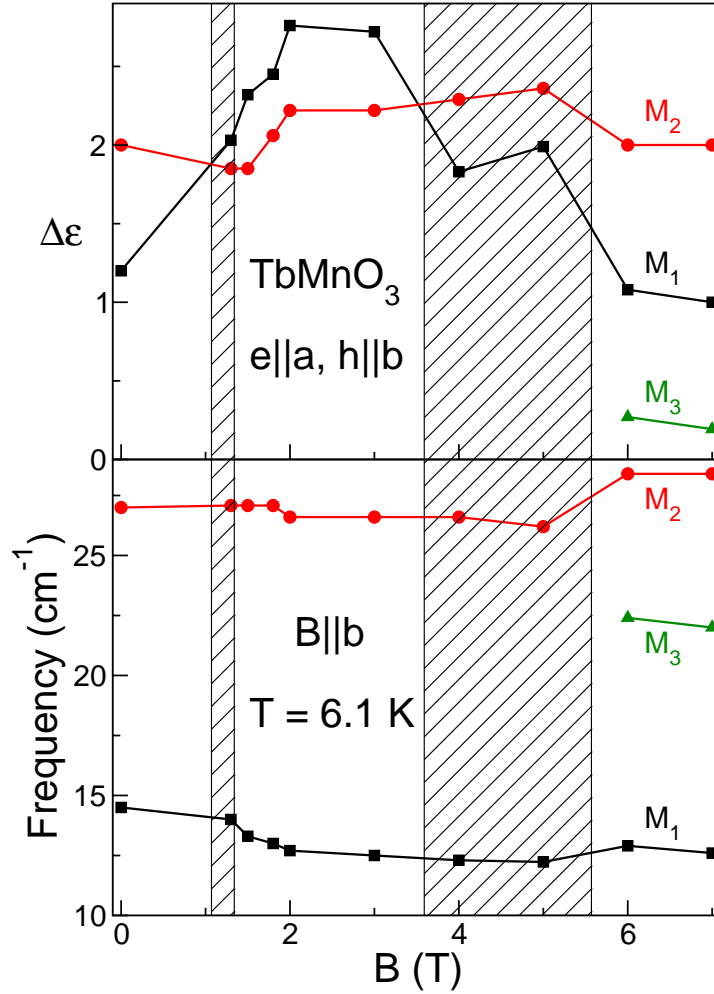


Figure 7.10: Dependence of mode parameters in TbMnO_3 upon magnetic field along b axis. Upper panel: mode strength, lower panel: resonance frequency. The modes designation is the same as in Fig. 7.9.

of transmittance experiments for ac-electric fields along the c and b axes was carried out [89].

Fig. 7.11 shows magnetic field dependencies of refractive index n and absorption coefficient κ for geometry with $e||b$ and $h||a$. The data are given in the representation $n + i\kappa = \sqrt{\epsilon\mu}$ because both electric and magnetic contributions are mixed in this experimental geometry. Although no electromagnon is expected for the present polarization ($e||b$), the changes of the optical properties upon transition into the ac -cycloid phase at 7 T are clearly seen. The changes in the Fig. 7.11 can be easily explained by the emergence of a new Lorentz-shaped mode around 20 cm^{-1} . This assumption is confirmed by the terahertz spectra shown below.

Similar magnetic field dependencies of optical constants for geometry $e||c$ and $h||a$ are shown in Fig. 7.12. The data are represented as refractive index $n + i\kappa = \sqrt{\epsilon\mu}$ again. The transition from bc plane to ab plane cycloid in the high magnetic fields is

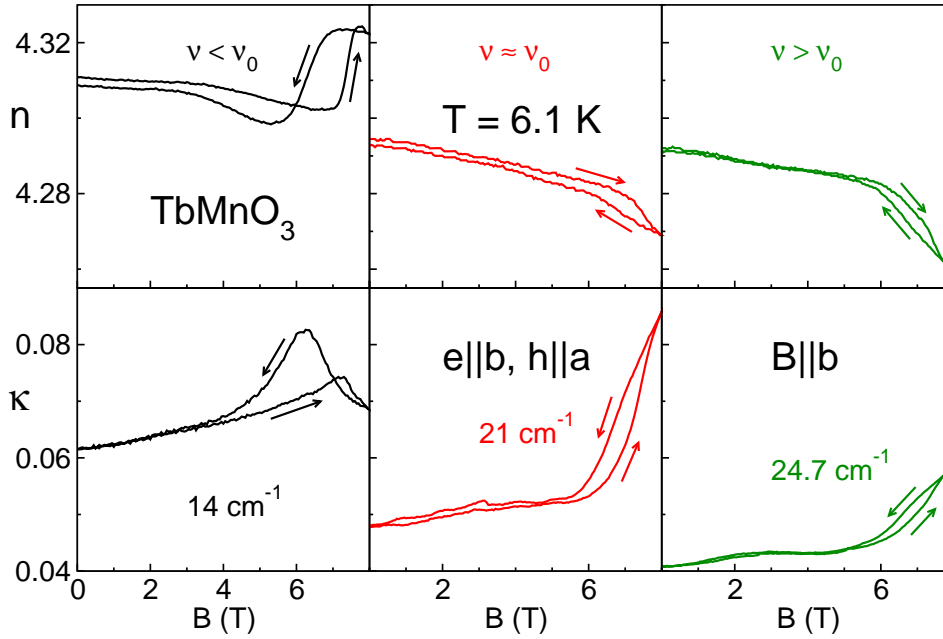


Figure 7.11: Magnetic field dependence of the refractive index n and absorption coefficient κ in *TbMnO*₃ along the b axis. Close to $B = 6$ T the magnetic bc cycloid is switched to the ab cycloid.

clearly seen. Already at this point it is clear that the observed changes are strongly frequency dependent. Here the data at 4.7 cm^{-1} is influenced by a Tb-mode around 5 cm^{-1} [85] which disappears in the high-field phase with the ab plane cycloid. This leads to a substantial decrease of the absorption ($\kappa(4.7\text{ cm}^{-1})$) and reveals a bit complicated structure in refractive index below 10 cm^{-1} . The changes observed at 4.7 cm^{-1} can be well understood assuming a suppression of a Lorentzian mode situated between 5 and 6 cm^{-1} . Three higher frequency scans in Fig. 7.11 show more systematics. Same as in the geometry $e||b, h||a$, it can be reduced to a growth of the absorption mode around 20 cm^{-1} . Indeed, strong additional absorption arises near the frequency $\simeq 20\text{ cm}^{-1}$ and is substantially reduced above and below this frequency (28 cm^{-1} and 16 cm^{-1} , respectively). At the same time there is an increase of refractive index n below this frequency and a decrease above 20 cm^{-1} . This is a typical behaviour for a Lorentz oscillator which appears close to 20 cm^{-1} simultaneously with the ab plane cycloid. In order to justify this description, the spectra of *TbMnO*₃ in the relevant frequency range are considered.

Figure 7.13 shows the field dependent spectra for two different geometries of the experiment. The thicknesses of the samples are similar for both orientations: 1.24 mm (upper panel) and 1.33 mm (lower panel), respectively. The spectra in the lower panel with $e||c$ and $h||a$ correspond well to the known results [40, 85] and show a mode at about 21 cm^{-1} . Based on the weakness of this mode, both in Ref. [40] and in Ref. [85] it has been concluded that the mode around 21 cm^{-1} is of purely magnetic origin and represent an antiferromagnetic resonance of the magnetic cycloid. Indeed, the strength of this mode ($\Delta\varepsilon \sim 0.05$, assuming electric origin) is extremely weak compared to elec-

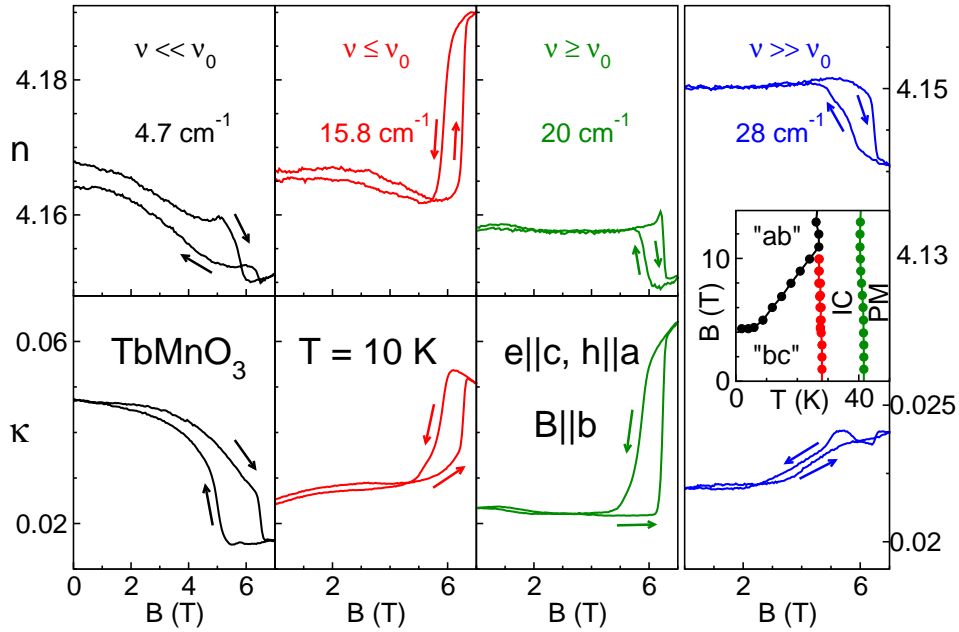


Figure 7.12: Dependence of refractive index (upper panels) and absorption coefficient (lower panels) in TbMnO_3 on magnetic field $B||b$ at various frequencies. Polarization of incident wave is $e||c, h||a$. The inset shows B - T phase diagram of TbMnO_3 for $B||b$ [20]. “ ab ” and “ bc ” denote ab plane and bc plane oriented cycloids, respectively, PM - paramagnetic and IC - sinusoidal phases.

tromagnon observed for $e||a$ ($\Delta\varepsilon \sim 2$) [16, 60]. The mode in Fig. 7.13 is observed for the ab plane cycloid and within $h||a$ excitation conditions. Tracing this mode back into the bc -oriented cycloid, it can be expected to originate from the excitation conditions $h||c$. (This corresponds simply to the interchanging of the a axis and c axis). Indeed, an AFMR mode excited for $h||c$ of the similar strength has been observed around 21 cm^{-1} [85]. As all changes detected along the c axis as function of magnetic field are extremely weak the obvious conclusion is that the mode at 20 cm^{-1} is of pure magnetic origin with excitation condition $h||a$.

A careful comparison of both panels in Fig. 7.13 reveals interesting difference between the two excitation conditions. The strength of the mode in the geometry where $e||b$ is roughly the half of that where $e||c$. This strongly suggests that for the geometry in which $e||c$ the electric dipole contribution is indeed measurable and represent the previously unobserved $e||c$ counterpart of the electromagnon. These results agree well with the original explanation of the electromagnons as electrically active eigenmodes of the cycloidal structure [38, 60].

In order to make the discussion quantitative, the experimental spectra in the upper panel of Fig. 7.13 were fitted with magnetic Lorentz oscillator. If now the parameters of the mode from the geometry with $e||b$ are taken and the expected transmittance spectra for the geometry $e||c$ is plotted the absorption value which is too weak compared to the experiment is obtained (the “ μ only” curve in the lower panel of Fig. 7.13). The only possible explanation is that this mode has distinct non-zero electric contribution along the c axis. The actual fit for this geometry was obtained by taking parameters

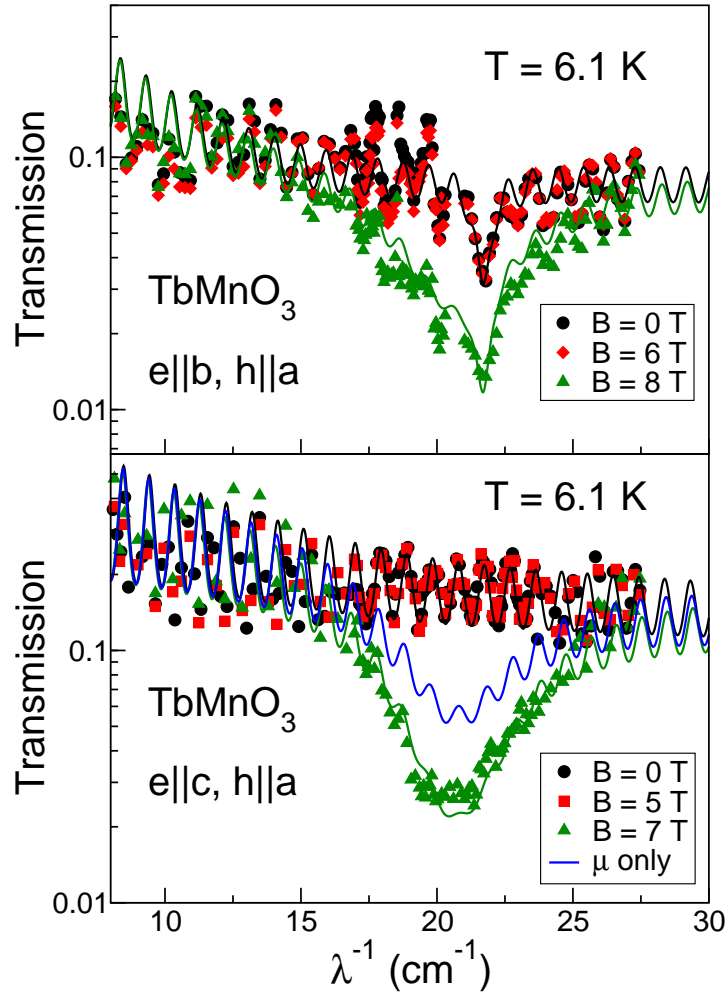


Figure 7.13: Transmittance spectra of $TbMnO_3$ in external magnetic fields $B||b$ for different experimental geometries. Symbols are experimental data and solid lines are fits with Lorentz oscillators as discussed in the text.

of the magnetic oscillator from $e||b$ geometry and adding an electric oscillator with the same resonance frequency $\nu_0 = 20.7 \text{ cm}^{-1}$ and line width $\gamma = 4.9 \text{ cm}^{-1}$ as the magnetic one. The reasoning behind this assumption is that both contributions are electric and magnetic parts of the same oscillating mode of the spin cycloid. The strengths of both components is given by $\Delta\mu = 0.0038$ and $\Delta\varepsilon = 0.05$, respectively. A weak narrow mode seen close to 22 cm^{-1} for $e||b, h||a$ geometry is possibly due to impurities in the sample. The strength of this mode is at least an order of magnitude smaller than the strength of the broad mode and doesn't change the overall picture.

The mode intensity for the “main” $e||a$ electromagnon ($\Delta\varepsilon_a \simeq 2$ [16]) is about 40 times stronger than electric contribution along the c axis ($\Delta\varepsilon_c \simeq 0.05$) observed in the present experiment. The large electromagnon absorption along a axis was a challenging question in explaining its origin. The relatively weak static electric polarization doesn't fit well with the large dielectric absorption of electromagnon if both are caused

by Dzyaloshinskii-Moriya interaction [40]. On the contrary, the Heisenberg exchange mechanism [40, 50, 90] seems to explain well the intensities of at least the high-frequency electromagnons. In this model the edge-zone magnon couples to alternating orthorhombic distortions at oxygen sites via symmetric Heisenberg exchange interaction. This leads to the coupling of the zone edge magnon to homogeneous electric fields along the a axis. As the symmetric interaction is much stronger than the relativistic DM coupling the hybridized electromagnon has enough strength to explain the experimental intensities for $e\parallel a$. Much weaker [40] DM component cannot be seen in this experimental geometry because of the dominance of the intensity induced by the Heisenberg exchange coupling. On the contrary, rotating the magnetic cycloid towards the ab plane, both contributions can be well separated experimentally. The Heisenberg exchange part remains oriented along the a axis, as confirmed by different experimental groups [40, 65, 78, 85]. The weak DM electromagnon rotates with the cycloid and can be clearly observed in the present experiment as electric contribution along the c axis.

Finally, we recall that at $T = 10$ K four magnetic modes have been identified in our experiments (Fig. 7.3). Three of them are probably the eigenmodes of the spin cycloid and correspond to distinct features in inelastic neutron scattering data [43, 44, 85]. Accepting this picture, the magnetic modes can be described as: i) phason mode of the cycloid for $h\parallel a$ and at 18 cm^{-1} [85]; this mode is seen as a weak contribution for $B = 0$ curve in the upper panel of Fig. 7.13, and ii)+iii) two transverse eigenmodes of the cycloid with $h\parallel bc$ excitation conditions and at 13 cm^{-1} and 22 cm^{-1} , respectively. After the rotation of the spin cycloid by the external field, the two latter modes are expected to switch their excitation condition from $h\parallel c$ axis to the $h\parallel a$ axis in full agreement with the present results. One remaining question is: why only one mode in the high-field phase is observed? The probable reason is that one of two modes is too weak and is not seen in the spectra. This argument is supported by recent inelastic neutron scattering experiments [87]. In these experiments the modes of the ab plane spin cycloid have been investigated. Although this ab plane orientation has been achieved using an external magnetic field along the a -axis, the comparison to the present results is still very instructive. It has been observed that the excitations of the ab cycloid are dominated by a strong mode at 2.25 meV [87]. This frequency corresponds well to the excitation at 21 cm^{-1} , seen in Fig. 7.13.

7.3 Summary

In TbMnO_3 , the closest agreement between the experimental data and theoretical models exists concerning the explanation of the high-frequency electromagnon. It is now widely accepted that this electromagnon represents a zone boundary magnon which becomes optically active within the Heisenberg exchange model of the magnetoelectric coupling. The possibility to excite the zone boundary magnon is due to the fact that the Mn-O-Mn bonds alternate within the crystallographic ab plane thus allowing for an additional modulation within the unit cell. Again, the details of this bonds arrangement allow the electric excitation of this magnon for ac electric fields parallel to the

crystallographic a axis.

In addition to the high-frequency electromagnon a second electromagnon of the comparable strength exists at frequencies between 10 cm^{-1} and 30 cm^{-1} . Within a Heisenberg exchange model a possible explanation for this electromagnon is the anisotropy and anharmonicity of the magnetic cycloid. The fine structure of the low-frequency electromagnon should most probably be attributed to the eigenmodes of the cycloidal spin structure. The basic argument in favour of this conclusion is the close coincidence of the resonance frequencies observed by the inelastic neutron scattering and in terahertz absorption experiments.

Performing a detailed polarization analysis of the electric and magnetic excitations in TbMnO_3 in the high-field phase where spin cycloid rotates from bc - to ab -plane, the eigenmodes of the magnetic cycloid can be also seen separately from the strong electromagnon. The observed excitation at 21 cm^{-1} can not be described by purely magnetic contribution as was suggested previously. We argue that this excitation is the missing electro-active mode of the spin cycloid. The weakness of this mode is in agreement with the inverse Dzyaloshinskii-Moriya model. The dielectric contribution of this mode is about 40 times weaker than of the electromagnon.

8 Conclusions and outlook

This work presents the results of the spectroscopic study of rare earth manganites RMnO_3 ($\text{R} = \text{Gd}, \text{Dy}, \text{Tb}, \text{Eu}_{1-x}\text{Y}_x$) in the frequency range $2\text{-}40\text{ cm}^{-1}$. The focus is on the multiferroic materials with coexisting ferroelectric and antiferromagnetic order parameters. The nonconductive materials with strong magnetoelectric coupling are interesting both for applications in memory cells or spin current polarizers and for the fundamental research of the mechanisms of the magnetoelectric interaction.

The existence of the improper ferroelectricity below 20 K in the multiferroic manganites is due to the cycloidal spin ordering, which breaks the spatial inversion symmetry. The magnetic origin of the ferroelectricity is responsible for the strong magnetoelectric coupling. Immediate consequence of this coupling is the possibility to control static electric polarization via external magnetic field. From the spectroscopic point of view the strong coupling is manifested by the existence of electromagnons – spin waves excited by an electric component of light. The electromagnons were first discovered in GdMnO_3 and TbMnO_3 around 20 cm^{-1} and they were observed in all materials, studied in this thesis.

An exact analytical solution of the Landau-Lifshitz equations, obtained for a cycloidal antiferromagnet, builds a theoretical ground for the analysis of the experimental results. Due to the complicated nature of the frustrated magnetic ground state, the inelastic neutron scattering data are hard or even impossible to directly compare with the results of the optical spectroscopy. The spin-waves solution is the bridge between these two experimental methods, and a semi-quantitative agreement is achieved, despite the known oversimplifications of the model Hamiltonian. Two most important mechanisms of the magnetoelectric coupling, the so-called inverse Dzyaloshinskii-Moriya (IDM) interaction and the model based on the symmetric Heisenberg exchange (HE) striction, are introduced in a perturbative manner. The qualitative conclusions regarding both static and dynamic electric properties are given, and they are in a good agreement with the experiment.

In GdMnO_3 , apart from the earlier found electromagnon at 20 cm^{-1} , the far infrared measurements have revealed another strong excitation at 75 cm^{-1} . This mode is excited by an electric component of the electromagnetic radiation and it is sensitive to the magnetic structure. Due to similarities to the low-frequency electromagnon, this mode is termed high-frequency electromagnon. Its observation in GdMnO_3 makes this material very similar to other multiferroic manganites, although only small static electric polarization is observed in the intermediate temperature range. It is possible that the strongly competitive *A*-type antiferromagnetic order prevents the development of the long range cycloidal ordering.

The spectroscopic study of $\text{Eu}_{1-x}\text{Y}_x\text{MnO}_3$ compounds has helped to establish the role

of the rare earth's moments in the multiferroic properties. The Y^{3+} ion is diamagnetic and Eu^{3+} possess only weak Van Vleck paramagnetism. The observation of the electromagnons in these materials has showed that it is the Mn subsystem that is primarily responsible for both magnetic and magnetoelectric properties in rare earth manganites.

The study of the electromagnons in $DyMnO_3$ in external magnetic fields has further clarified the interplay between manganese and rare earth spins. Depending on the Dy ordering, the electromagnons and static electric polarization can be either enhanced or suppressed. Even more importantly, the excitation conditions of electromagnons in external magnetic fields were shown to substantially differ from the behavior of static electric polarization. While the polarization flops in magnetic fields $B||a$ and $B||b$, the electromagnon always remains visible for the polarization with electric field along the crystallographic a axis ($Pbnm$ setting).

The Terbium manganite is the most studied material in the whole series. The extensive comparison of the magnetic and electric excitations, reported in the present thesis, with the inelastic neutron scattering data and theoretical model has left no doubt that the electromagnon is an electrically excited spin wave. Like in $DyMnO_3$, the low frequency electromagnon does not change its excitation conditions upon the flop of the static electric polarization in external magnetic fields. This observation together with the large experimental spectral weight still need a consistent theoretical explanation. On the other hand, the detailed measurements on samples with different orientations have allowed to detect a weak electric contribution along the c axis at 21 cm^{-1} , in a state with the ab spin cycloid. This is a first direct observation of a dynamic counterpart of the IDM interaction which is responsible for the static electric polarization.

In summary, the inverse Dzyaloshinskii-Moriya interaction is capable to describe both the emergence and the flop of the static electric polarization. The weak electro-active excitation in the high-field phase of $TbMnO_3$ at 21 cm^{-1} also stems from this type of relativistic coupling. The model based on the symmetric Heisenberg exchange striction is successful in explaining the high frequency electromagnon. The excitation conditions and the spectral weight are also well understood within this model. In order to provide an explanation for the low frequency electromagnon, a magnetic anisotropy and higher harmonics of the spin cycloid within Heisenberg exchange model have been suggested. However, these attempts are still unable to describe the frequency and the spectral weight of the low-frequency electromagnon in the whole series of rare earth manganites. Further theoretical efforts are required in this direction. On the experimental side, the detection of the dynamic magnetoelectric susceptibility predicted for the IDM based electromagnon remains an interesting and challenging task.

Since the discovery of electromagnons in $GdMnO_3$ and $TbMnO_3$, these excitations were detected in many other multiferroics as well. For example, in the family of rare earth manganites RMn_2O_5 , both the static electric polarization and the electromagnons seem to emerge from the symmetric HE interaction. The systematic comparison of the amplitude of the static polarization with the spectral weight of the electromagnon will provide a good test of the theory. The iso-structural materials $RFeMnO_5$, where Mn^{3+} is substituted by Fe^{3+} , show much higher magnetic transition temperatures, paving the promising way to increase the number of room-temperature multiferroics. Spectroscopic

study of these materials will certainly help to better understand and improve their magnetoelectric properties. The preliminary results of the submillimeter spectroscopy of Samarium ferroborate $\text{SmFe}_3(\text{BO}_3)_4$ show the existence of an extremely low-lying ($< 1 \text{ cm}^{-1}$) excitation, which is both magnetically and electrically active. Further theoretical and experimental study will help to establish the underlying mechanism of magnetoelectric coupling in these iron based multiferroics.

In general, materials with magnetoelectric coupling do not only reveal a new intriguing physics but they also supply new ideas for applications especially in the field of microelectronics. Therefore, this field of research will continue its rapid development in a foreseeable future.

Bibliography

- [1] W. E. H. Lecky, *Democracy and liberty*, Vol. 1 (Longmans, New York, 1903).
- [2] T. Kimura, T. Goto, H. Shintani, K. Ishizaka, T. Arima, and Y. Tokura, *Nature*, **426**, 55 (2003).
- [3] P. Curie, *J. Phys. Theor. Appl.*, **3**, 393 (1894).
- [4] L. D. Landau and E. M. Lifshits, *Electrodynamics of continuous media* (Pergamon Press, Oxford, 1960).
- [5] I. E. Dzyaloshinskii, *Sov. Phys. JETP*, **10**, 628 (1960).
- [6] D. N. Astrov, *Sov. Phys. JETP*, **11**, 708 (1960).
- [7] D. N. Astrov, *Sov. Phys. JETP*, **13**, 729 (1961).
- [8] T. H. O'Dell, *The electrodynamics of magneto-electric media* (North-Holland Publishing, Amsterdam, 1970).
- [9] I. E. Chupis, “Ferroelectromagnets. fifty years after discovery,” <http://arxiv.org/abs/arXiv:1012.2024> arXiv:1012.2024 (2010).
- [10] Y. Tokunaga, N. Furukawa, H. Sakai, Y. Taguchi, T. Arima, and Y. Tokura, *Nat. Mater.*, **8**, 558 (2009).
- [11] M. Bibes and A. Barthélémy, *Nat. Mater.*, **7**, 425 (2008).
- [12] C. Ederer and N. A. Spaldin, *Phys. Rev. B*, **71**, 060401 (2005).
- [13] T. Zhao, A. Scholl, F. Zavaliche, K. Lee, M. Barry, A. Doran, M. P. Cruz, Y. H. Chu, C. Ederer, N. A. Spaldin, R. R. Das, D. M. Kim, S. H. Baek, C. B. Eom, and R. Ramesh, *Nat. Mater.*, **5**, 823 (2006).
- [14] Y.-H. Chu, L. W. Martin, M. B. Holcomb, M. Gajek, S.-J. Han, Q. He, N. Balke, C.-H. Yang, D. Lee, W. Hu, Q. Zhan, P.-L. Yang, A. Fraile-Rodriguez, A. Scholl, S. X. Wang, and R. Ramesh, *Nat. Mater.*, **7**, 478 (2008).
- [15] C. Binek and B. Doudin, *J. Phys.: Condens. Matter*, **17**, L39 (2005).
- [16] A. Pimenov, A. A. Mukhin, V. Y. Ivanov, V. D. Travkin, A. M. Balbashov, and A. Loidl, *Nat. Phys.*, **2**, 97 (2006).

- [17] V. G. Baryakhtar and I. E. Chupis, *Fiz. Tverd. Tela*, **10**, 2818 (1969).
- [18] V. G. Baryakhtar and I. E. Chupis, *Fiz. Tverd. Tela*, **11**, 2628 (1970).
- [19] E. Golovenchits and V. Sanina, *J. Phys.: Condens. Matter*, **16**, 4325 (2004).
- [20] T. Kimura, G. Lawes, T. Goto, Y. Tokura, and A. P. Ramirez, *Phys. Rev. B*, **71**, 224425 (2005).
- [21] T. Kimura, S. Ishihara, H. Shintani, T. Arima, K. T. Takahashi, K. Ishizaka, and Y. Tokura, *Phys. Rev. B*, **68**, 060403 (2003).
- [22] J. A. Alonso, M. J. Martínez-Lope, M. T. Casais, and M. T. Fernández-Díaz, *Inorg. Chem.*, **39**, 917 (2000).
- [23] T. Mori, N. Kamegashira, K. Aoki, T. Shishido, and T. Fukuda, *Mater. Lett.*, **54**, 238 (2002).
- [24] J. Hemberger, F. Schrettle, A. Pimenov, P. Lunkenheimer, V. Y. Ivanov, A. A. Mukhin, A. M. Balbashov, and A. Loidl, *Phys. Rev. B*, **75**, 035118 (2007).
- [25] J. A. Moreira, A. Almeida, W. S. Ferreira, J. E. Araújo, A. M. Pereira, M. R. Chaves, J. Kreisel, S. M. F. Vilela, and P. B. Tavares, *Phys. Rev. B*, **81**, 054447 (2010).
- [26] H. A. Jahn and E. Teller, *Proc. R. Soc. Lond. A*, **161**, 220 (1937).
- [27] J. Rodríguez-Carvajal, M. Hennion, F. Moussa, A. H. Moudden, L. Pinsard, and A. Revcolevschi, *Phys. Rev. B*, **57**, 3189 (1998).
- [28] J. Hubbard, *Proc. R. Soc. Lond. A*, **276**, 238 (1963).
- [29] J. B. Goodenough, *Magnetism and the Chemical Bond* (Interscience Publishers, New York, 1963).
- [30] A. Pimenov, A. Loidl, A. A. Mukhin, V. D. Travkin, V. Y. Ivanov, and A. M. Balbashov, *Phys. Rev. B*, **77**, 014438 (2008).
- [31] E. O. Wollan and W. C. Koehler, *Phys. Rev.*, **100**, 545 (1955).
- [32] L. Landau and E. Lifshits, *Phys. Z. Sowjetunion*, **8**, 153 (1935).
- [33] B. Lax and K. J. Button, *Microwave ferrites and ferrimagnetics*, Lincoln Laboratory publications (McGraw-Hill, New York, 1962).
- [34] C. Kittel, *Introduction to solid state physics*, 8th ed. (Wiley, New York, 2005).
- [35] M. Kenzelmann, A. B. Harris, S. Jonas, C. Broholm, J. Schefer, S. B. Kim, C. L. Zhang, S.-W. Cheong, O. P. Vajk, and J. W. Lynn, *Phys. Rev. Lett.*, **95**, 087206 (2005).

-
- [36] T. A. Kaplan, *Phys. Rev.*, **116**, 888 (1959).
- [37] K. Yosida and H. Miwa, *J. Appl. Phys.*, **32**, S8 (1961).
- [38] H. Katsura, A. V. Balatsky, and N. Nagaosa, *Phys. Rev. Lett.*, **98**, 027203 (2007).
- [39] N. Kida, Y. Takahashi, J. S. Lee, R. Shimano, Y. Yamasaki, Y. Kaneko, S. Miyahara, N. Furukawa, T. Arima, and Y. Tokura, *J. Opt. Soc. Am. B*, **26**, A35 (2009).
- [40] R. V. Aguilar, M. Mostovoy, A. B. Sushkov, C. L. Zhang, Y. J. Choi, S.-W. Cheong, and H. D. Drew, *Phys. Rev. Lett.*, **102**, 047203 (2009).
- [41] M. P. V. Stenberg and R. de Sousa, *Phys. Rev. B*, **80**, 094419 (2009).
- [42] K. Hradil, Private communications (2012).
- [43] D. Senff, P. Link, K. Hradil, A. Hiess, L. P. Regnault, Y. Sidis, N. Aliouane, D. N. Argyriou, and M. Braden, *Phys. Rev. Lett.*, **98**, 137206 (2007).
- [44] D. Senff, N. Aliouane, D. N. Argyriou, A. Hiess, L. P. Regnault, P. Link, K. Hradil, Y. Sidis, and M. Braden, *J. Phys.: Condens. Matter*, **20**, 434212 (2008).
- [45] M. Mostovoy, Private communications (2012).
- [46] H. Katsura, N. Nagaosa, and A. V. Balatsky, *Phys. Rev. Lett.*, **95**, 057205 (2005).
- [47] I. Dzyaloshinsky, *J. Phys. Chem. Solids*, **4**, 241 (1958).
- [48] T. Moriya, *Phys. Rev.*, **120**, 91 (1960).
- [49] I. A. Sergienko and E. Dagotto, *Phys. Rev. B*, **73**, 094434 (2006).
- [50] S. Miyahara and N. Furukawa, “Theory of electric field induced one-magnon resonance in cycloidal spin magnets,” <http://arxiv.org/abs/arXiv:0811.4082v1> arXiv:0811.4082v1 (2008).
- [51] M. Mochizuki, N. Furukawa, and N. Nagaosa, *Phys. Rev. Lett.*, **104**, 177206 (2010).
- [52] A. A. Volkov, Y. G. Goncharov, G. V. Kozlov, S. P. Lebedev, and A. M. Prokhorov, *Infrared Phys.*, **25**, 369 (1985).
- [53] G. V. Kozlov and A. A. Volkov, in *Millimeter and Submillimeter Wave Spectroscopy of Solids*, edited by G. Grüner (Springer, Berlin, 1998) p. 51.
- [54] D. W. Berreman, *J. Opt. Soc. Am.*, **62**, 502 (1972).
- [55] A. M. Shuvaev, G. V. Astakhov, A. Pimenov, C. Brüne, H. Buhmann, and L. W. Molenkamp, *Phys. Rev. Lett.*, **106**, 107404 (2011).
- [56] A. M. Balbashov, S. G. Karabashev, Y. M. Mukovskiy, and S. A. Zverkov, *J. Cryst. Growth*, **167**, 365 (1996).

- [57] J. Hemberger, S. Lobina, H.-A. Krug von Nidda, N. Tristan, V. Y. Ivanov, A. A. Mukhin, A. M. Balbashov, and A. Loidl, *Phys. Rev. B*, **70**, 024414 (2004).
- [58] A. Pimenov, T. Rudolf, F. Mayr, A. Loidl, A. A. Mukhin, and A. M. Balbashov, *Phys. Rev. B*, **74**, 100403 (2006).
- [59] A. M. Shuvaev, F. Mayr, A. Loidl, A. A. Mukhin, and A. Pimenov, *Eur. Phys. J. B*, **80**, 351 (2011).
- [60] A. Pimenov, A. M. Shuvaev, A. A. Mukhin, and A. Loidl, *J. Phys.: Condens. Matter*, **20**, 434209 (2008).
- [61] V. F. Sears, *Neutron News*, **3**, 26 (1992).
- [62] S. Danjoh, J.-S. Jung, H. Nakamura, Y. Wakabayashi, and T. Kimura, *Phys. Rev. B*, **80**, 180408 (2009).
- [63] Y. Takahashi, S. Ishiwata, S. Miyahara, Y. Kaneko, N. Furukawa, Y. Taguchi, R. Shimano, and Y. Tokura, *Phys. Rev. B*, **81**, 100413 (2010).
- [64] R. V. Aguilar, A. B. Sushkov, C. L. Zhang, Y. J. Choi, S.-W. Cheong, and H. D. Drew, *Phys. Rev. B*, **76**, 060404 (2007).
- [65] Y. Takahashi, Y. Yamasaki, N. Kida, Y. Kaneko, T. Arima, R. Shimano, and Y. Tokura, *Phys. Rev. B*, **79**, 214431 (2009).
- [66] A. A. Mukhin, M. Biberacher, A. Pimenov, and A. Loidl, *J. Magn. Reson.*, **170**, 8 (2004).
- [67] Y. Yamasaki, S. Miyasaka, T. Goto, H. Sagayama, T. Arima, and Y. Tokura, *Phys. Rev. B*, **76**, 184418 (2007).
- [68] H. Murakawa, Y. Onose, F. Kagawa, S. Ishiwata, Y. Kaneko, and Y. Tokura, *Phys. Rev. Lett.*, **101**, 197207 (2008).
- [69] M. Tokunaga, Y. Yamasaki, Y. Onose, M. Mochizuki, N. Furukawa, and Y. Tokura, *Phys. Rev. Lett.*, **103**, 187202 (2009).
- [70] S. Issing, F. Fuchs, C. Ziereis, E. Batke, A. Pimenov, Y. V. Ivanov, A. A. Mukhin, and J. Geurts, *Eur. Phys. J. B*, **73**, 353 (2010).
- [71] S. Issing, A. Pimenov, V. Y. Ivanov, A. A. Mukhin, and J. Geurts, *Phys. Rev. B*, **81**, 024304 (2010).
- [72] S. Issing, A. Pimenov, Y. V. Ivanov, A. A. Mukhin, and J. Geurts, *Eur. Phys. J. B*, **78**, 367 (2010).
- [73] S. Issing, *Correlation between Lattice Dynamics and Magnetism in Multiferroic Manganites*, Ph.D. thesis, University of Würzburg, Würzburg (2011).

-
- [74] J. Stremper, B. Bohnenbuck, M. Mostovoy, N. Aliouane, D. N. Argyriou, F. Schrettle, J. Hemberger, A. Krimmel, and M. v. Zimmermann, *Phys. Rev. B*, **75**, 212402 (2007).
- [75] S.-W. Cheong and M. Mostovoy, *Nat. Mater.*, **6**, 13 (2007).
- [76] T. Goto, T. Kimura, G. Lawes, A. P. Ramirez, and Y. Tokura, *Phys. Rev. Lett.*, **92**, 257201 (2004).
- [77] R. Feyerherm, E. Dudzik, N. Aliouane, and D. N. Argyriou, *Phys. Rev. B*, **73**, 180401 (2006).
- [78] N. Kida, Y. Ikebe, Y. Takahashi, J. P. He, Y. Kaneko, Y. Yamasaki, R. Shimano, T. Arima, N. Nagaosa, and Y. Tokura, *Phys. Rev. B*, **78**, 104414 (2008).
- [79] R. Feyerherm, E. Dudzik, A. U. B. Wolter, S. Valencia, O. Prokhnenko, A. Maljuk, S. Landsgesell, N. Aliouane, L. Bouchenoire, S. Brown, and D. N. Argyriou, *Phys. Rev. B*, **79**, 134426 (2009).
- [80] F. Kagawa, M. Mochizuki, Y. Onose, H. Murakawa, Y. Kaneko, N. Furukawa, and Y. Tokura, *Phys. Rev. Lett.*, **102**, 057604 (2009).
- [81] S. Quezel, F. Tcheou, J. Rossat-Mignod, G. Quezel, and E. Roudaut, *Physica B+C*, **86-88**, 916 (1977).
- [82] R. Kajimoto, H. Yoshizawa, H. Shintani, T. Kimura, and Y. Tokura, *Phys. Rev. B*, **70**, 012401 (2004).
- [83] M. Mostovoy, *Phys. Rev. Lett.*, **96**, 067601 (2006).
- [84] S. Foner, in *Magnetism*, edited by G. T. Rado and H. Suhl (Acad. Press, New York, 1963) p. 383.
- [85] A. Pimenov, A. Shuvaev, A. Loidl, F. Schrettle, A. A. Mukhin, V. D. Travkin, V. Y. Ivanov, and A. M. Balbashov, *Phys. Rev. Lett.*, **102**, 107203 (2009).
- [86] D. N. Argyriou, N. Aliouane, J. Stremper, I. Zegkinoglou, B. Bohnenbuck, K. Habicht, and M. v. Zimmermann, *Phys. Rev. B*, **75**, 020101 (2007).
- [87] D. Senff, P. Link, N. Aliouane, D. N. Argyriou, and M. Braden, *Phys. Rev. B*, **77**, 174419 (2008).
- [88] N. Aliouane, D. N. Argyriou, J. Stremper, I. Zegkinoglou, S. Landsgesell, and M. v. Zimmermann, *Phys. Rev. B*, **73**, 020102 (2006).
- [89] A. M. Shuvaev, V. D. Travkin, V. Y. Ivanov, A. A. Mukhin, and A. Pimenov, *Phys. Rev. Lett.*, **104**, 097202 (2010).
- [90] J. S. Lee, N. Kida, Y. Yamasaki, R. Shimano, and Y. Tokura, *Phys. Rev. B*, **80**, 134409 (2009).

Acknowledgments

Finally, I wish to thank the following people:

- Prof. Dr. Andrei Pimenov for the support, guidance and the indefinite patience throughout my dissertation writing
- Prof. Dr. Jean Geurts and Dr. Sven Issing for performing complementary far infrared and Raman measurements and especially Prof. Dr. Jean Geurts for the extensive proofreading of the manuscript
- Prof. Dr. Ralph Claessen for the fruitful discussions on the advanced physical topics
- Prof. Dr. Alois Loidl and the whole Chair of Experimental Physics 5 from Augsburg for kindly providing experimental support on the early stages of the project
- Prof. Dr. Markus Braden and Dr. Klaudia Hradil for the explanations of the critical neutron scattering data
- Prof. Dr. Anatoly Balbashov for providing large high quality single crystals
- Dr. Alexander Mukhin for introducing me into the field of magnetism and further theoretical discussions
- Anna Pimenov for the help with the x-ray and crystal structure data
- Monika Seifer for the great amount of assistance, which was especially invaluable during early accommodation in Germany
- Dr. Markus Paul for the critical competent proofreading of the manuscript and for the warm friendship and the introduction into the Swabian culture
- Dr. Benjamin Schmid for the great friendly support in Würzburg and for keeping up the conversations on military topics
- Sebastian Engelbrecht and Markus Schiebl for proofreading, the fruitful debates about dark corners of thermodynamics and for the friendly support in Würzburg and Wien
- Wlad Dziom for the critical proofreading of the manuscript, translation of the original work by P. Curie and for the introduction into tank battle tactics.

- Prof. Dr. Maxim Mostovoy and Dr. Sergey Artyukhin for the helpful explanations of the advanced theoretical topics and for ensuring me that Chapter 2 is not completely wrong
- all members of the Chair of Experimental Physics 4 for the kind assistance and the favourable working atmosphere
- Alexander and Natalie Proskurin, Anastasia Sanygina, Evgenia Kuzin and Natalia Pashina for the warm russian reception in Würzburg and for the priceless favour in one situation
- my family for their constant love, support and their understanding of my decision to do my PhD thesis abroad
- my marvelous girlfriend Stephanie Wogowitsch for her great backing, care and tremendous resignation during all days and nights I have spent in the laboratory